

Design and Fabrication of Porous Graphene Materials for
Advanced Supercapacitors

Shao Qingguo

Doctoral Program in Materials Science and Engineering

Submitted to the Graduate School of

Pure and Applied Sciences

in Partial Fulfillment of the Requirements

for the Degree of Doctor of Philosophy in Engineering

at the

University of Tsukuba

Abstract

Graphene, a one-atom-thick two-dimensional carbon material, due to its exceptional physical, chemical, and mechanical properties, has been a promising candidate for a broad range of applications. Graphene offers large specific surface area, high conductivity, excellent mechanical flexibility and outstanding chemical stability. These characteristics make graphene an attractive electrode material for supercapacitors. However, the graphene sheets tend to restack due to the strong π - π interactions and van der Waals forces between them, which cause significant decrease in the electrochemically active surface area and the inter-graphene channels accessible to electrolyte, leading to lower specific capacitance. To address this problem, one effective strategy is to synthesis of graphene electrode materials with a desired morphology/structure for easing the restacking. Here, in this thesis, we have developed a series of graphene electrodes with different micro-structures and architectures. These rational designed graphene structures show many advantages, i.e., large specific surface area, favorable pore structure, or high conductivity, when they are used for supercapacitor applications.

We first successfully assembled graphene nanosheets into hollow spherical shells and tested them as electrode material for supercapacitors. Compared with planar stacked graphene sheets, the hollow spherical graphene shells can provide more free space between the spheres and therefore reduce effectively restacking of graphene sheets. More accessible surface area will also be produced for ion adsorption. Electrochemical characterization shows that the graphene hollow spheres exhibit impressive specific capacitance of 273 F g^{-1} at a low current density of 0.5 A g^{-1} and 197 F g^{-1} at a high current density of 10 A g^{-1} , respectively. Moreover, when it was charged and discharged repeatedly at a high current density of 10 A g^{-1} , 95% of its initial capacitance was retained even after 5000 cycles. These findings indicate that the graphene hollow spheres are promising as electrode material for supercapacitors.

The as prepared graphene hollow spheres were further investigated as the conductive matrixes to load SnO_2 nanoparticles, where the SnO_2 nanoparticles are confined between the multi-layered sheets of graphene hollow spheres. The obtained composite was used as anode for Li-ion battery. With this design, firstly, the volume changes of SnO_2 nanoparticles during the charging and discharging process can be restricted by the multi-layered graphene. Secondly, the graphene spheres can also serve as a non-stacked high conductive substrate to facilitate Li^+ and electron transport. Thirdly, the interconnected nature of graphene hollow spheres makes the electrode can be self-assembled together eliminating the need of any binders which could lower the conductivity and increase weight of the whole electrode. Electrochemical tests show that the as designed unique graphene/ SnO_2 composite exhibit a large reversible capacity of 1001 mAh/g and excellent long cycling life with 85% retention

even after 100 cycles, indicating its great potential as high performance anode materials for lithium-ions battery.

Then we prepared a single-walled carbon nanotube spaced graphene aerogel (SSGA), in which the SWCNTs are sandwiched between graphene sheets to realize a high specific capacitance together with a high rate capability. The aerogel provides a macro-porous structure and the numerous large pores make the electrode be wetted quickly by the electrolyte to ensure high rate performance; The SWCNTs are placed between the graphene layers to prevent the restacking of graphene sheets and more accessible surface area is made available for ion adsorption; The introduction of highly conductive SWCNTs can also reduce the resistance of the SSGA electrode to further increase the rate capability and promote stable cycling performance. Electrochemical characterization showed that the composites exhibited a high specific capacitance of 245.5 F g^{-1} at a current density of 2.5 A g^{-1} and a high specific capacitance of 197.0 F g^{-1} at a high current density of 80 A g^{-1} in aqueous electrolyte. After 2000 times of repeated charge and discharge cycles at a high current density of 10 A g^{-1} , 97% of its initial capacitance was retained. A high capacitance of 183.3 F g^{-1} at 0.5 A g^{-1} and a high energy density of 80 Wh kg^{-1} were achieved using an ionic liquid (EMIMBF₄) as the electrolyte.

We also prepared curved graphene sheets by ionic liquid mediate chemical reduction of graphene oxide in aqueous electrolyte. Electrochemical test results show that the relaxation time and charge transfer resistance at electrode-electrolyte interface for curved graphene electrode is one third and one fourth of that for common graphene electrode, respectively, indicating the improved compatibility between the electrode and the electrolyte. Benefited from that, the capacitance retention of curved graphene electrode from current density of 0.5 A g^{-1} to 20 A g^{-1} is 84.4 %, which is extremely higher than that of common graphene electrode (52.9 %), highlighting its enhanced rate capability in ionic liquid electrolyte.

In addition, we also fabricated some other novel nanostructured electrode materials beyond graphene. Firstly, a highly porous carbon nanofiber paper was constructed by heat treatment of fullerene nanofiber paper. The obtained carbon nanofiber paper exhibits ultra-high external surface area, and it could be directly used as electrode for supercapacitors. A high energy density of 106 kWh kg^{-1} was achieved using ionic liquid as electrolytes. Secondly, we also fabricated a hierarchical NiCo₂O₄ nanocube assembled with porous nanosheets for pseudo-capacitors. It could exhibit a high specific capacitance of 930 F g^{-1} , and excellent cycling stability with 88 % retention after 2000 cycles.

Content

Abstract	I
Chapter 1	
Introduction	1
1.1 Historical overview	1
1.2 Fundamentals of supercapacitors.....	2
1.2.1 Electrical double-layer capacitor	3
1.2.2 Pseudo-capacitor.....	4
1.2.3 Electrolytes	5
1.3 Advantages and disadvantages of supercapacitors	6
1.3.1 Advantages of supercapacitors	6
1.3.2 Disadvantages for supercapacitors	7
1.4 Graphene based supercapacitors.....	8
1.4.1 Introduction of graphene	8
1.4.2 Graphene electrodes prepared by chemical reduction method.	9
1.4.3 Graphene electrodes prepared by physical method.	10
1.4.4 Graphene-metal oxide composite electrodes	11
1.4.5 Graphene-conducting polymer composite electrodes.....	12
1.4.6 Other kinds of graphene based electrodes	13
1.5 Current research and motivation.....	15
1.5.1 Current research results of graphene based electrodes	15
1.5.2 Originality of this work	16
References	18
Chapter 2	
Experimental Technique	21
2.1 Electrochemical testing methods.....	21

2.1.1 Cyclic voltammetry	21
2.1.2 Galvanostatic charge and discharge	22
2.1.3 Electrochemical impedance spectroscopy	23
2.2 Electrochemical testing configuration	24
2.2.1 Two-electrode test configuration	24
2.2.2 Three-electrode test configuration	25
2.3 Summary of the testing technique	25
References	25

Chapter 3

Synthesis and Characterization of Graphene Hollow Spheres for Application in Supercapacitors	26
3.1 Introduction	26
3.2 Experimental section	27
3.2.1 Synthesis of positively charged PS sphere	27
3.2.2 Synthesis of PS@graphene core-shell spheres	27
3.2.3 Synthesis of graphene hollow spheres	27
3.2.4 Structural characterization	28
3.2.5 Electrochemical characterization	28
3.3 Results and discussion	28
3.4 Conclusions	33
References	34

Chapter 4

Confining SnO₂ nanoparticles between multi-layered and interconnected graphene shells as binder-free anodes for high-capacity lithium-ion batteries	35
4.1 Introduction	35
4.2 Experimental section	36
4.2.1 Synthesis of graphene oxide (GO)	37

4.2.2 Synthesis of polystyrene (PS) spheres	37
4.2.3 Synthesis of PS@SnO ₂ /graphene oxide multi-layered spheres	37
4.2.4 Synthesis of SnO ₂ /graphene shells	37
4.2.5 Structural characterization	37
4.2.6 Electrochemical characterization	38
4.3 Results and discussion	38
4.4 Conclusions	46
References	46

Chapter 5

Carbon nanotube Spaced Graphene Aerogels with Enhanced Capacitances in Aqueous and Ionic liquid Electrolytes	48
5.1 Introduction	48
5.2 Experimental	50
5.2.1 Sample preparation	50
5.2.2 Structural characterization	51
5.2.3 Electrochemical characterization	51
5.3 Results and discussion	51
5.3.1 Preparation and morphology	51
5.3.2 Structural study	53
5.3.3 Capacitance behaviors in aqueous electrolyte	55
5.3.4 Capacitance behaviors in ionic liquid electrolyte	58
5.3.5 EIS analysis	59
5.3.6 Ragone plot and cycle stability	61
5.4 Conclusions	62
References	62

Chapter 6

Curved graphene from Ionic liquid mediated reduction of graphene oxide for supercapacitor with improved rate capability in ionic liquid electrolyte	64
6.1 Introduction	64
6.2 Experimental section	66
6.2.1 Preparation of Graphene oxide (GO).....	66
6.2.2 Preparation of Reduce Graphene oxide (RGO).	66
6.2.3 Preparation of Ionic liquid modified reduced graphene oxide (RGO-IL).	66
6.2.4 Characterization.....	66
6.2.5 Electrochemical measurements.	67
6.3 Results and discussion.....	67
6.4 Conclusions	72
References	73

Chapter 7

Fabrication of a Highly Porous Carbon Nanofiber Paper with Large External Surface Area and Its Application for High Energy Density Supercapacitors	74
7.1 Introduction	74
7.2 Experimental section	75
7.2.1 Fabrication of Highly Porous Carbon Nanofiber Paper (HPNFP).	75
7.2.2 Characterizations.	75
7.2.3 Fabrication of a high energy density coin cell supercapacitor.....	76
7.2.4 Fabrication of a flexible All-Solid-State supercapacitor.	76
7.2.5 Electrochemical measurements.	76
7.3 Results and discussion.....	76
7.4 Conclusions	82
References	82

Chapter 8

Hierarchical NiCo₂O₄ Nanocubes Constructed by Nanosheets with Excellent Pseudo-capative Properties	84
8.1 Introduction	84
8.2 Experimental section	85
8.2.1 Synthesis of Cu ₂ O nanocubes	85
8.2.2 Synthesis of hierarchical NiCo ₂ O ₄ nanocubes	85
8.2.3 Structural characterization	85
8.2.4 Electrochemical characterization	85
8.3 Results and discussion	86
8.4 Conclusions	92
References	92
Chapter 9	
Conclusions and Perspective	94
9.1 Conclusions	94
9.2 Future Prospects	98
Chapter 10	
Achievements	100
10.1 List of Publications	100
10.2 Oral Presentations	101
10.3 Patent	101
Acknowledgements	102

Chapter 1

Introduction

1.1 Historical overview

With the rapid growth of the economic expansion, the energy consumption, and the environmental pollution, there has been an urgent need for cheap, clean, and renewable energy sources. Among of various energy conversion and storage devices, supercapacitors also known as electrical capacitors, which display intermediate power and energy between dielectric capacitors and batteries, have attracted particular research attention in recent years due to their high power density and long cycle lifetime [1–5].

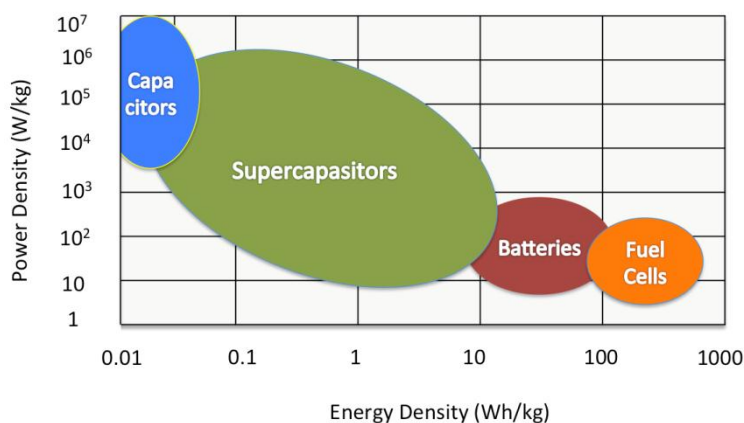


Figure 1-1 A Ragone plot of power density versus energy density for various electrochemical energy storage devices. [3]

There are several parameters to evaluate the performances of the energy storage systems. These parameters include energy density (Wh/kg) power density (W/kg), specific capacitance (F/g), specific capacity (mA h g⁻¹), cycle life, and the safety. In order to compare these energy storage systems,

Figure 1-1 shows the Ragone plot of power density versus energy density for the most common energy storage systems. High-energy storage systems contain batteries and fuel cells. And, supercapacitors and conventional capacitors are high-power storage systems.

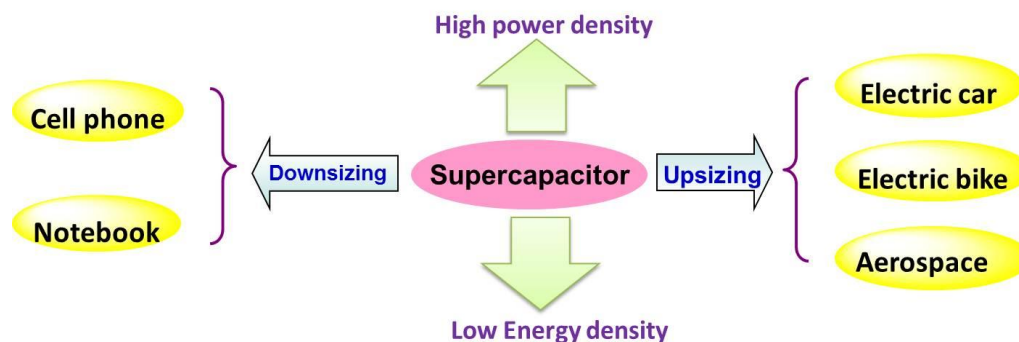


Figure 1-2 Schematic illustration the broad application of supercapacitors.

Because of the high power capability, long cycle life and reliability, supercapacitors have been used in a variety of applications (as shown in Figure 1-2) ranging from cell phones, notebooks, to electric cars and electric bikes, and to even to aerospace. The fast charge/discharge rates and long cycle life lead supercapacitors suitable for recycling energy from automotive braking, or elevator operation which will improve the energy efficiency.

Based on the energy storage mechanisms, supercapacitors can be divided into two categories: electric double layer capacitors (EDLCs) and pseudocapacitors. [3,4,6-9] Pseudocapacitors, which store charges from fast and reversible redox reactions at the surface of electroactive materials (MnO_2 , NiCO_2O_4 , conducting polymers), usually faces problems of either short cycling life or poor rate ability, let along their high cost. As for EDLCs, the capacitance comes from the reversible ion absorption at the electrode/electrolyte interface. Carbon based materials with high surface area, such as activated carbons (ACs) and mesoporous carbons (MCs), are ideal candidates for EDLCs. ACs are widely used for EDLCs electrode materials because of their extremely high specific surface area (up to $3000 \text{ m}^2 \text{ g}^{-1}$), abundant raw materials, and moderate cost. However, the specific capacitances of ACs are usually not so high as expected especially when increasing the charging-discharging rate, which are mainly caused by the large quantity of micropores in ACs that are inaccessible by the electrolyte. [10-15] For MCs, their relatively regular structure and suitable pore size bring about acceptable capacitances and considerable cycling life, nevertheless the fabrication of MCs usually involves complex or multi steps which are not suitable for mass production and the cost is also very high. [16-25]

1.2 Fundamentals of supercapacitors

As described in the Introduction, there are two types of supercapacitors. The first one is the electric double-layer capacitor, in which the energy is stored in the electrode materials by physical

absorption of the electrolyte ions at the electrode/electrolyte interface. In this case, no electrochemical redox reactions occur during the charging and discharging of the electric double layer capacitors. Carbon based materials, such as activated carbon, carbon nanotubes, and carbon fibers are widely used as electrodes for electric double-layer capacitors. The other kind is the pseudo-capacitor, in which the energy is stored by the surface electrochemical redox reactions. The typical electrodes contain transition metal oxides, conducting polymers, etc. [26–31]

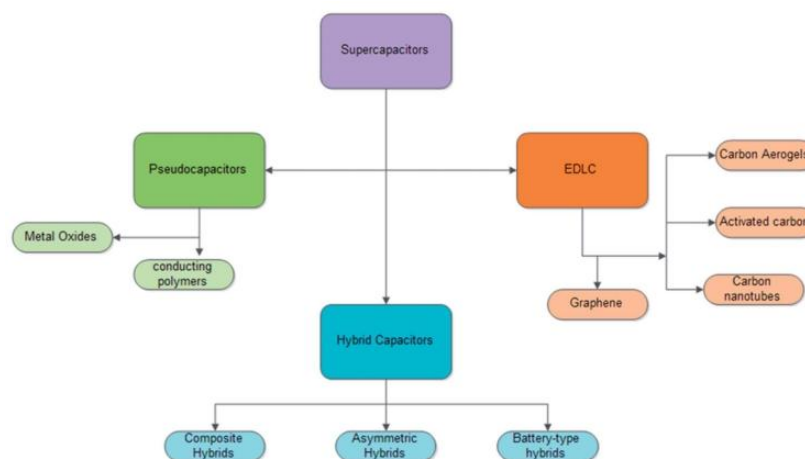


Figure 1-3 A chart showing types of supercapacitors. [6]

1.2.1 Electrical double-layer capacitor

Electrical double-layer capacitors store energy by physical absorption of the electrolyte ions at the electrode/electrolyte interface. As shown in Fig. 1, this electrical double-layer capacitance comes from electrode material particles, such as at the interface between the carbon particles and electrolyte, where an excess or a deficit of electric charges is accumulated on the electrode surfaces, and electrolyte ions with counterbalancing charge are built up on the electrolyte side in order to meet electro-neutrality. During the process of charging, the electrons travel from the negative electrode to the positive electrode through an external load. Within the electrolyte, cations move towards the negative electrode while anions move towards the positive electrode. During discharge, the reverse processes take place. In this type of supercapacitors, no charge transfers across the electrode/electrolyte interface, and no net ion exchanges occur between the electrode and the electrolyte. This implies that the electrolyte concentration remains constant during the charging and discharging processes. In this way, energy is stored in the double-layer interface. [1,32-38]

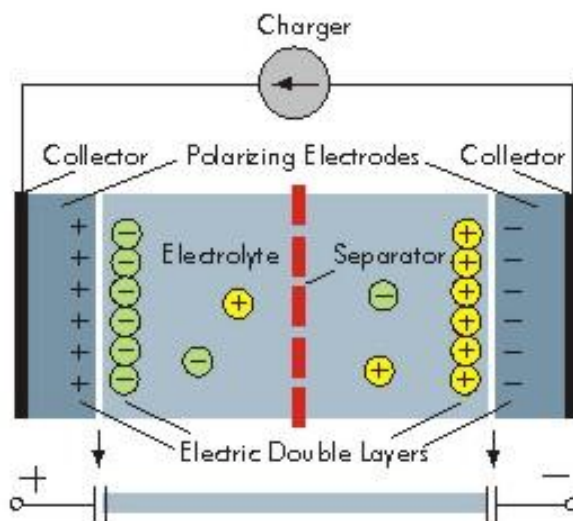
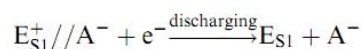
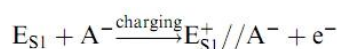


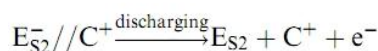
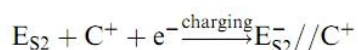
Figure 1-4 Schematic diagram of electrical double-layer capacitors. [6]

The charging and discharging of the electrical double-layer capacitors can be classified as follows. The E_{S1} and E_{S2} are the two electrodes surfaces, A^- and C^+ are anions and cations, respectively. The electrode/electrolyte interface is illuminated as //.

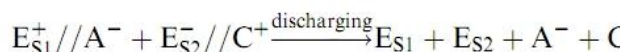
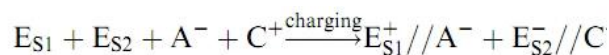
On the positive electrode:



On the negative electrode:



And the whole charge and discharge process can be expressed:



1.2.2 Pseudo-capacitor

Different from electrical double-layer capacitors, fast and reversible redox reactions occur on the electrode materials when a potential is applied to pseudo-capacitors. The charging and discharging process of pseudo-capacitors is similar with batteries, where Faraday reactions happen, resulting in

faradaic current passing through the supercapacitors. The different is that the redox reactions can only take place on the surface of the electrodes for pseudo-capacitors, which is different from batteries on the bulk materials. The materials for pseudo-capacitors contain several metal oxides, including RuO_2 , MnO_2 , and Co_3O_4 , and conducting polymers. There are mainly three kinds of faradaic processes taken place for the pseudo-capacitors electrodes: reversible adsorption (for example, adsorption of hydrogen on the surface of platinum or gold), redox reactions for transition metal oxides (e.g. Co_3O_4 , MnO_2), and reversible electrochemical doping–dedoping for conductive polymers. [32,33,39-49]

Generally, because of the faradaic reactions, the operating voltage can be extended a lot. Most importantly, the specific capacitance of the pseudo-capacitors is much larger than electrical double-layer capacitors. Conway et al, have demonstrated that the capacitance of a pseudo-capacitors can be 10–100 times larger than that of electrical double-layer capacitors. [3] In this case, the energy density of the pseudo-capacitors is also larger than electrical double-layer capacitors. However, the power densities of pseudo-capacitors are usually lower than that of electrical double-layer capacitors because faradaic processes are normally slower than physical adsorption. Besides, because there are faradaic reactions at the electrode, pseudo-capacitors usually suffer a low cycling stability.

1.2.3 Electrolytes

As shown in Fig. 1-3, the electrolyte is also one of the most important parts for supercapacitors. There are a few requirements for the electrolytes used in supercapacitors such as high electrochemical stability, high ionic concentration, low ionic radius, low viscosity, low toxicity, wide voltage window, and low cost.

There are mainly three types of electrolytes for supercapacitors: (1) aqueous electrolyte, (2) organic electrolyte, and (3) ionic liquids (ILs). [1]The comparison of the three electrolytes is shown in Table.1-1.

Table.1-1 The advantages and disadvantages of aqueous electrolytes, organic electrolytes, and ionic liquids electrolytes.

Items Electrolytes	Advantages	Disadvantages
Aqueous electrolyte (H_2SO_4 , KOH , Na_2SO_4)	Higher ionic concentration Lower resistance Smaller ionic radius Stable in air	Low voltage window(<1.2V)
Organic electrolyte (TEA-BF_4 , LiPF_6)	Wider voltage window Low cost Environment friendly	Need to be processed in glove box Low conductivity

Ionic liquids electrolyte (EMI-BF ₄ ,EMI-TFSI)	High voltage window(up to 6V) Good conductivity Wide temperature range No toxicity	High cost high viscosity
---	---	-----------------------------

1.3 Advantages and disadvantages of supercapacitors

Supercapacitor, as a kind of energy storage device, provides high power density and moderate energy density. Table 1-2 list some of the important properties of supercapacitors. The detailed advantages and disadvantages of supercapacitors are discussed below. [50-53]

Table 1-2. Some properties of supercapacitors

Items	Performance
Power density	100-10000 W/kg
Energy density	10-100 Wh/kg
Coulombic efficiency	>90%
Cycling life	>10 0000
Shelf life	>10 years
Operating voltage	0.5-3.5V
Operating temperature	-30-80 °C
Self-discharge rate	20-50% per day
Toxicity	No
Safety	High
Cost	Low
Industrial standard	Limited

1.3.1 Advantages of supercapacitors

1.3.1.1 High power density

Supercapacitor stores energy from the chemical absorption of the electrolyte ions or the redox

reactions on the surface. So the charge-discharge time is much less than the bulk electrochemical redox reaction of batteries. Generally, it is only takes a few seconds to fully charge a supercapacitor.

1.3.1.2 Long life expectancy

When the charging or discharging a supercapacitor, no or negligibly small chemical charge transfer reactions and phase changes happened, so the supercapacitor have good cycling stability. Generally, a supercapacitors can be charged and discharged with little changes of capacitance for 1000–1 0 000 cycles.

1.3.1.3 Long shelf life

Long shelf life is also an advantage of supercapacitors. Researchers have found that a supercapacitor can still keep its capacitance for many years with only a little of the capacitance.

1.3.1.4 High efficiency

The energy stored in a supercapacitor is highly reversible. The energy loss during the charging and discharging is relatively small and can be ignored (i.e., heat management is easy). The coulombic efficiency for a supercapacitor is almost 100%.

1.3.1.5 Wide range of operating temperatures

Supercapacitors can still work even at extremely high and low temperatures. The typical working temperature for a supercapacitor is from -30 to 80 °C.

1.3.1.6 Environmental friendliness

There is no hazardous or toxic materials used in a supercapacitor, and the waste can be easily disposed.

1.3.1.7 Safety

In general, the safety of a supercapacitor is much better than fuel cells or batteries.

1.3.2 Disadvantages for supercapacitors

1.3.1.7 Low energy density

The energy density of a supercapacitor is usually ranging from 5 to 50 W h kg⁻¹, which is much less than batteries.

1.3.1.7 High cost

The cost of the raw materials for a supercapacitor is very high. The production of carbon based electrodes with high specific surface area usually involves complex steps, so this kind of electrode materials is rather expensive. Besides, the electrolyte and the separator also increase the cost.

1.3.1.7 High self-discharging rate

The self-discharging of a supercapacitor is serious. It is reported that 20–50% of the capacitance can be lost after one day.

1.3.1.7 Industrial standards for commercialization

Supercapacitors are now widely commercially available. However, there are limited general industrial standards such as device performance, thickness of the electrode, electrode configuration, and electrode porosity and so on.

1.4 Graphene based supercapacitors

1.4.1 Introduction of graphene

Graphene is a two dimensional single atom thick sp^2 bonded carbon material, and it is also considered as the “mother” building block for other kinds of carbon materials. As shown in Fig.1-5, graphene can be wrapped into zero dimensional buckyballs, or rolled into one dimensional carbon nanotubes, or stacked into three-dimensional graphite. In 2004, Andre Geim and Konstantin Novoselov developed a method to produce high quality single layer graphene in which they use an adhesive tape to peel graphite until the single layer carbon is found. Then, in 2010, they got the Nobel Prize in physics “for groundbreaking experiments regarding the two-dimensional material graphene.” After that, graphene had been a “research star” and the tremendous efforts have been devoted to this two-dimensional nano carbon material. [50,51,54]

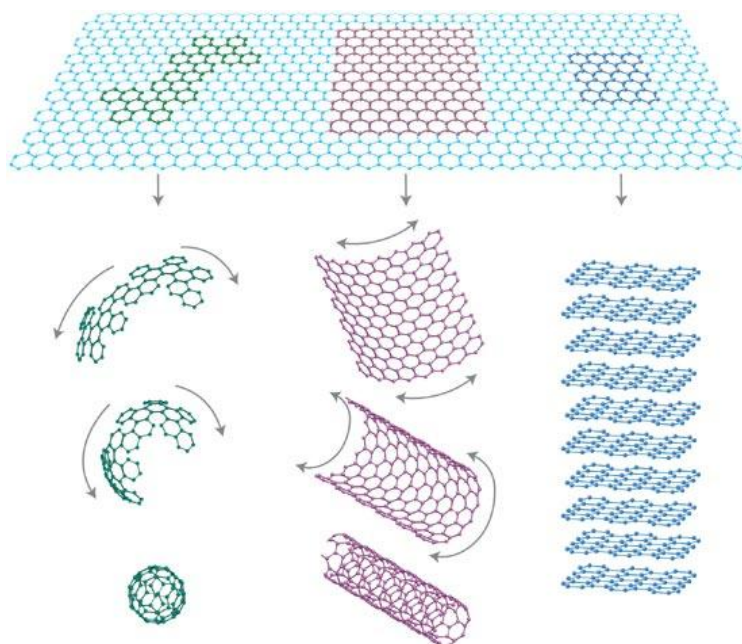


Figure 1-5 Schematic illustration of graphene is a 2D building material for carbon materials of all other dimensionalities. It can be wrapped up into 0D buckyballs, rolled into 1D nanotubes or stacked into 3D graphite. [53]

Graphene exhibits many remarkable chemical, physical, optical and mechanical properties. For example, graphene shows the fracture strength as high as 125 GPa and its thermal conductivity is nearly $5000 \text{ W m}^{-1} \text{ K}^{-1}$. Besides, graphene also exhibits high specific surface area (as high as $2630 \text{ m}^2 \text{ g}^{-1}$), high optical transmittance, and high chemical stability. Due to these attracted properties, graphene based materials have been widely exploited in many fields, including gas sensors, photo catalysis, oil absorption, and energy storage.

1.4.2 Graphene electrodes prepared by chemical reduction method.

Ruoff et al. have pioneered the use of chemically modified graphenes (CMGs) for supercapacitor application. The CMGs show a good electrical conductivity $2 \times 10^2 \text{ S m}^{-1}$, which eliminates the need for other conductive additives. More importantly, the CMG materials are assembled from one-atom thick carbon, and it shows a large specific surface area of $705 \text{ m}^2 \text{ g}^{-1}$. Different from activated carbons, each individual CMG sheet can change its position to accommodate the electrolyte ions. In this case, it is much easier for the electrolyte ions to fully access to the entire surface of the chemically modified graphene. Electrochemical tests show the CMGs can deliver high specific capacitances of 135 and 99 F g^{-1} in aqueous and organic electrolytes, respectively. Considering the further space for increasing the specific surface area and electric conductivity, the chemical reduced graphene hold great potential for high performance supercapacitors. [55]

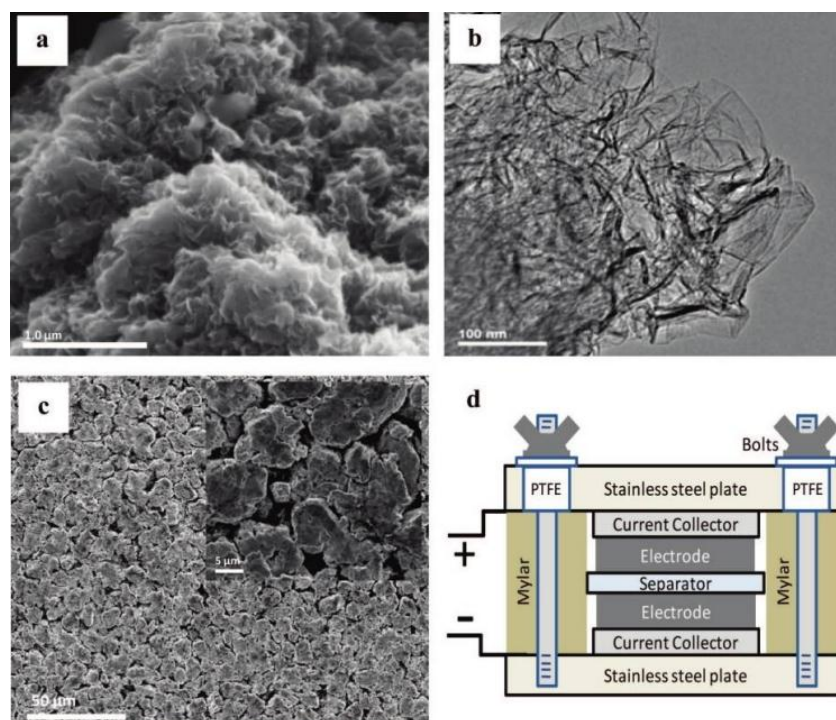


Figure 1-6 (a,c) SEM images, (b) TEM image of the surface of CMG particle electrode, and (d) schematic of the test configuration. [55]

It is found that chemical reduced graphene usually suffer from irreversible agglomerates. Chen et al. have developed a gas-solid reduction method to produce graphene materials. The as prepared graphene materials show much less agglomeration compared traditional reduction method. When they were used for supercapacitor application in aqueous electrolyte, the as prepared graphene show a large specific capacitance of 205 F/g and a high energy density of 28.5 W h/kg . Besides, the supercapacitor based on these graphene materials also demonstrates super cycling performance. 90% of the initial capacitance can be retained even after 1200 repeated charge-discharge cycles. [55]

Hydrazine hydrate is generally used as reduction agent for reducing graphene oxide. Ma et al. have exploited hydrobromic acid as a novel reduction agent for chemical production of graphene.

Compared with hydrazine hydrate, hydrobromic acid is a much weaker reductant. So, there still exists a few amount of oxygen containing groups in the reduced graphene. Surprisingly, the capacitance of the reduced graphene could exhibit an extremely large capacitance of 384 F/g at a current density of 0.2 A/g in 1 M H₂SO₄ aqueous electrolyte. The reasons for the enhanced capacitance lie in the fact that the oxygen functional groups on the graphene surface could increase the wettability of the electrode and also bring about pseudo-capacitance.

1.4.3 Graphene electrodes prepared by physical method.

Chen et al. have exploited a low temperature thermal method for producing graphene. The supercapacitor based on these graphene materials could exhibit a specific capacitance of 220 F/g in aqueous electrolyte and a specific capacitance of 120 F/g in organic electrolyte. The advantage of this method is that it could be easily scaled up and the cost is relatively low. [56]

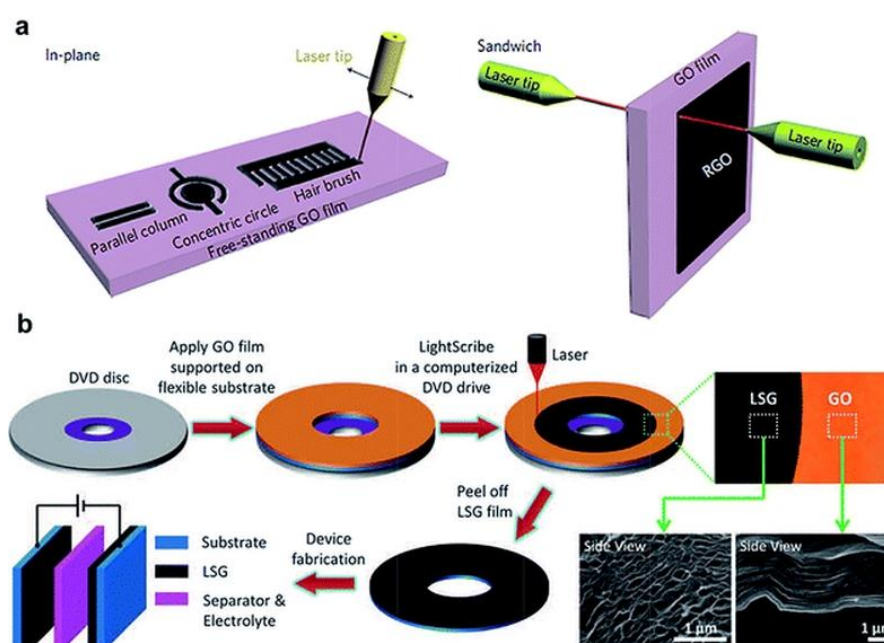


Figure 1-7 (a) A Sandwiched rGO-GO-rGO micro-supercapacitor by laser patterning, (b) A supercapacitor based on laser scribed graphene. [56,57]

Recently, laser reduction of graphene oxide has got a lot of attention. Ajayan et al. have used a laser writing method to directly reduce graphene oxide to graphene. In this work, the reduced graphene show a ultra-porous structure, which is because of the burning of oxygen groups and water on the graphene oxide surface in the laser reduction process. The supercapacitor based on this laser reduced graphene materials shows a large area capacitance of 0.4 mF/cm². However, the cycling performance is not very good. It shows a 35% drop after 10000 cycles. [57]

Kaner et al. have used a lightscribe DVD drive to reduce graphene oxide film to graphene. The laser-scribed graphene film shows an open network, which could largely reduce the agglomeration of graphene sheets. Besides, it also shows high conductivity and large specific surface area. An ultra-thin supercapacitor was assembled based on this laser-scribed graphene film and it demonstrates

desirable cycling properties where 96% of the capacitance can be preserved after 10000 cycles. [2]

1.4.4 Graphene-metal oxide composite electrodes

Graphene materials hold great potential for electric double-layer capacitor. Apart from that, graphene has also been used for loading metal oxides to form graphene/metal oxide composite electrodes. The composite electrode could adopt the electric double-layer capacitance together with high value of pseudocapacitance from the loaded metal oxide. By carefully tailoring the nanostructure of the composite, it will show synergistic effect for boosting the capacitance, improving the stability, and increasing the rate capability.

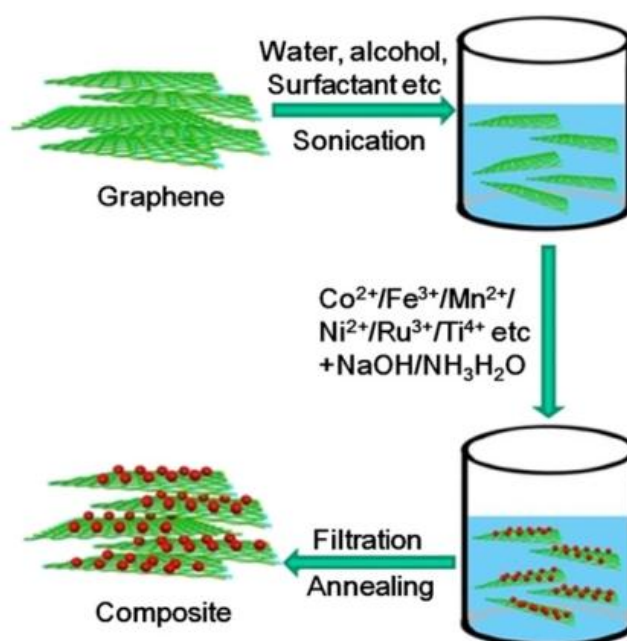


Figure 1-8 A general approach for preparing graphene-metal oxide composite electrodes. [59]

RuO_2 is considered as a promising material for pseudocapacitor due to its large capacitance. However, RuO_2 electrode prepared from thermal method or hydrothermal method usually suffers from a low capacitance owing to its low conductivity and low specific surface area. [58] Cheng and his co-workers used graphene as a conductive matrix to synthesis hydrous ruthenium oxide-graphene composite electrode by a sol-gel method in a low temperature condition. The RuO_2 nanoparticles were found randomly loaded on the surface of graphene sheets. The RuO_2 nanoparticles could serve as spacers to obstruct the restacking of graphene sheets. The specific surface area of the composite is $281 \text{ m}^2/\text{g}$, which is much larger than that of pure graphene sheets ($108 \text{ m}^2/\text{g}$) and pure RuO_2 powders ($3.0 \text{ m}^2/\text{g}$). On the other hand, the conductivity of the composite was largely increased due to the high conductive graphene. [59]

The as prepared composite was tested for supercapacitor application. It showed a high capacitance of 570 F/g , and this value is larger than the sum of the individual capacitance of the two components, indicating the synergistic effect between the RuO_2 nanoparticles and graphene sheets. More importantly, the composite can keep 98% of its initial capacitance after 1000 cycles at the

current density of 1 A/g.

1.4.5 Graphene-conducting polymer composite electrodes

Conducting polymers, such as polyaniline (PANI), polypyrrole (PPY), polythiophene (PTH), have been extensively studied for pseudocapacitors due to their high capacitance, low cost, and ease of preparation. However, the relatively low cycling life really limits their practical application. One effective strategy is to hybrid them with some high stable carbon materials, such as activated carbon, carbon nanotube, and graphene. Hao and his co-workers has synthesized a PANI/graphene composite using a in situ polymerization method. The obtained composite shows a large specific capacitance of 531 F/g, which is much larger than that of pure PANI sample, indicating the positive synergistic effect between the PANI and graphene. [60]

In another work, Wei and his co-workers have developed a convenient approach to synthesize PANI nanowire vertically grown on the surface of graphene. When it was tested for supercapacitor application, not only the cycling performance was largely improved, but also the specific capacitance was also increased. At a constant charge-discharge current density of 0.2 A/g, the composite could deliver a high capacitance of 555 F/g. Besides, the supercapacitor based on this composite could still maintain a capacitance of 227 F/g after 2000 cycles even under a high current density of 2 A/g. The author ascribes the enhanced electrochemical performance to the synergistic effect of the two components. Graphene sheets restrict the decomposition of PANI during the redox process and PANI contributes to the large capacitance. [61]

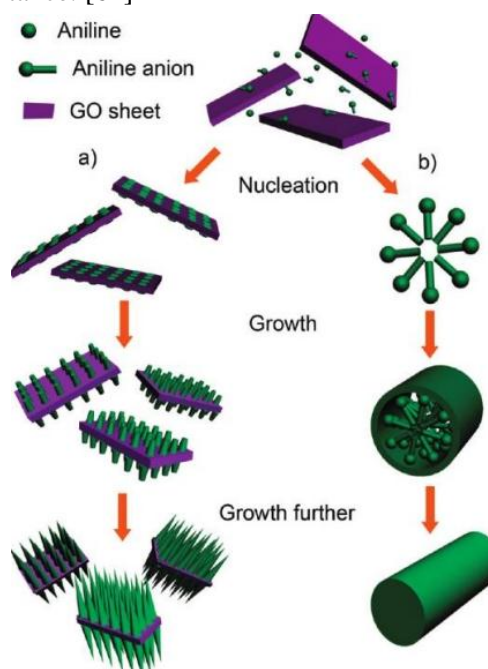


Figure 1-9 Schematic illustration of the fabrication mechanism of PANI nanowire coated graphene composite. [61]

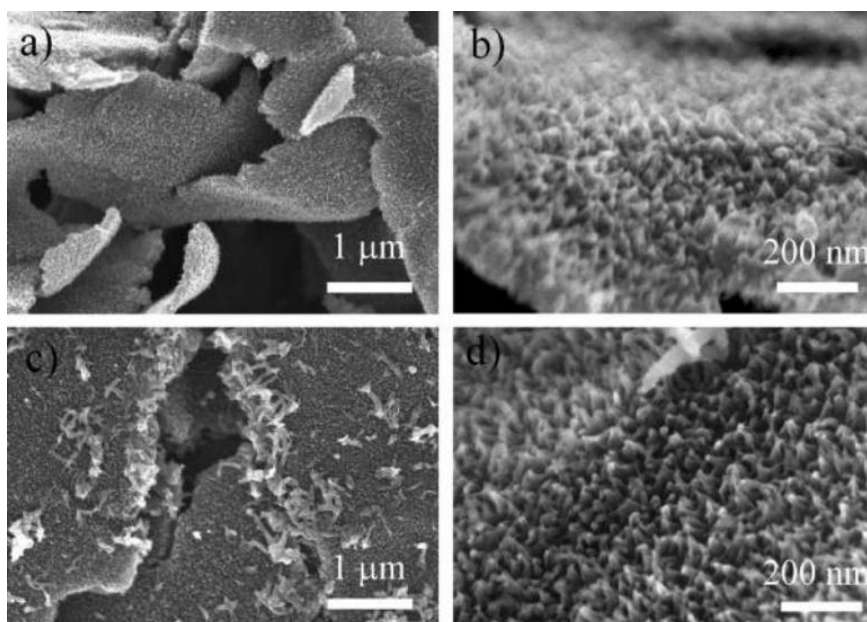


Figure 1-10 SEM images of PANI nanowire coated graphene composite. [61]

Apart from the chemical solution method, graphene/polyaniline composite paper was also prepared by in-situ anodic electropolymerization of aniline on graphene paper. When it was used for supercapacitor application, an reasonable electrochemical capacitance as high as 233 F g^{-1} was obtained.

1.4.6 Other kinds of graphene based electrodes

The stacked geometry of graphene as electrode usually leads to a low specific capacitance. The reasons can be classified as shown in Fig 1-11a. The graphene sheets are parallel to the current collector, which makes the inner layer of graphene sheets inaccessible to the electrolyte ions. Based on this issue, Ajyan and his co-workers have reported an “in plane” fabrication method for solid state supercapacitors. The novel concept is shown in Fig 1-9b. With this design, all the graphene layers could be easily interaction with the electrolyte ions, which result to the full utilization of the specific surface of graphene sheets. [62]

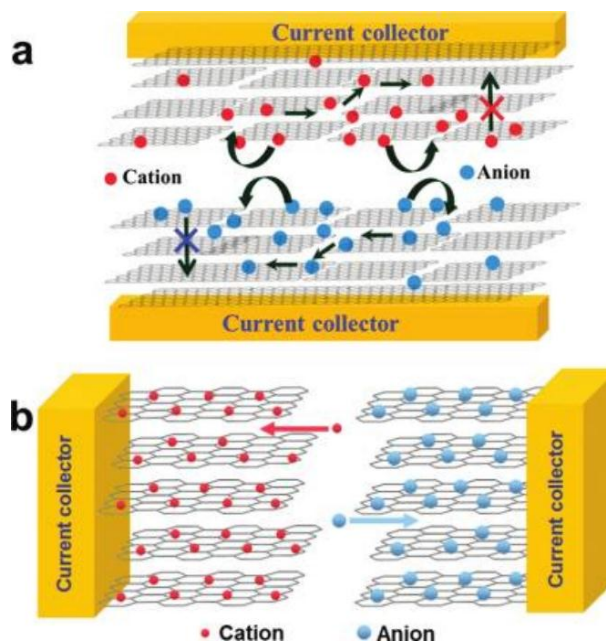


Figure 1-11 schematic comparison of the supercapacitors fabricated based on (a) stacked graphene and (b) in-plane graphene. [62]

Electrochemical tests show that the area normalized capacitance of this unique designed supercapacitor is 394 uF/cm^2 , which is much larger than the traditional graphene film (80 uF/cm^2). Besides, from the practical point, this geometry concept hold potential to be extended to other kind of graphene based functional devices. [62]

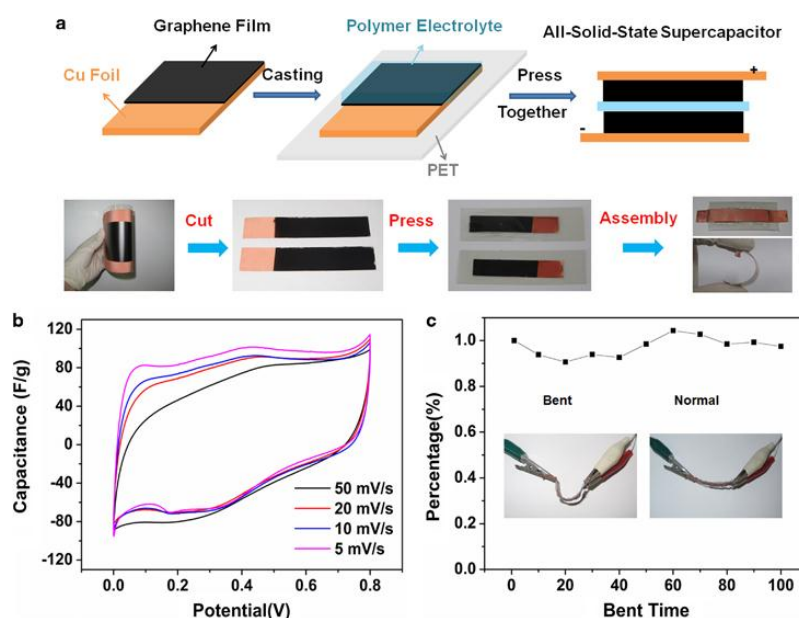


Figure 1-12 (a) Schematic illustration of preparation process of flexible all-solid state supercapacitor using photo reduced graphene film. (b) CV curves at different scanning rates of the supercapacitor. (c) Cycling performance of the supercapacitor under bending test. [63]

Li and his co-workers have developed a new solution-processable method to prepare thin graphene films. Graphene oxide sheets were directly cast onto Cu foil, and they were converted to

high conductive graphene sheets by a convenient illumination treatment. This method is a green, time-saving method. Most importantly, it can be easily scaled up. This photo-reduced graphene film was assembled to a solid state supercapacitor and the device show good flexibility and robust stability. Electrochemical tests reveal that it could deliver a high capacitance of 275 F/g at a scan rate of 10 mV/s. In addition, after 100 bending cycles, only 2% of the capacitance was lost, indicating its superior stability. [63]

1.5 Current research and motivation

1.5.1 Current research results of graphene based electrodes

The current research of graphene based electrodes can be classified into two categories, i.e., bare graphene based electrodes and graphene based composite electrodes. For the bare graphene electrode, the mostly used preparation methods involve chemical reduction method, hydrothermal method, thermal reduction method, and chemical vapor deposition (CVD) method. As for the graphene composite electrodes, conducting polymer including polyaniline, polypyrrole, polythiophene, and transition metal oxide including MnO_2 , RuO_2 , Co_3O_4 are widely exploited composition with graphene to increase the specific capacitance. Conducting polymers can be deposited on graphene surface by in situ polymerization method or electrodeposition method. Metal oxides can be coated on graphene sheets by hydrothermal method or chemical coprecipitation method. The obtained electrochemical performances of these graphene based electrode are summarized in Table 1-3.

Table. 1-3 Summary of the current research results of graphene based supercapacitors.

Category	Electrodes	Preparation method	Electrolyte	Capacitance (F/g)	Capacitance retention
Bare graphene materials	Chemical reduced Graphene	Hydrazine reduction	2 M H_2SO_4	194	90% (1000 cycles)
	Highly corrugated graphene	Thermal reduction	6 M KOH	349	108% (5000 cycles)
	3D pillar graphene	CVD grown	HNO_3 -IPA	330	-
	N-doped graphene	Hydrothermal method	5 M KOH	190	95% (4000 cycles)
Graphene-conducting polymer composite	Graphene oxide-polyaniline	In situ polymerization	1 M H_2SO_4	525	91% (200 cycles)
	Graphene-polyaniline	In situ polymerization	0.5 M H_2SO_4	500	119% (680 cycles)

	Graphene-polypyrrole	Ultrasonication	0.5 M H ₂ SO ₄	400	88% (200 cycles)
	Graphene-polyurethane	Simple bonding	1 M H ₂ SO ₄	218	95% (2000 cycles)
	Graphene-polyphenylenediamine	Chemical oxidation polymerization	1 M H ₂ SO ₄	525	72% (1000 cycles)
Graphene-metal oxide composite	Graphene-MnO ₂	Mild hydrothermal	1 M Na ₂ SO ₄	263	99% (500 cycles)
	Graphene-Mn ₃ O ₄	Hydrothermal	1 M Na ₂ SO ₄	121	100% (10000 cycles)
	Graphene-Co ₃ O ₄	2-step surfactant	6 M KOH	160	63% (1000 cycles)
	GO/Co ₃ O ₄ /MnO ₂	Electrochemical deposition	1 M KOH	117	-
	Graphene-NiO film	Chemical bath deposition	1 M KOH	400	63% (1000 cycles)
	Graphene-RuO ₂	Hydrothermal	1 M H ₂ SO ₄	155	-

1.5.2 Originality of this work

Graphene-based materials, due to their unique two dimensional structure and outstanding intrinsic physical properties, such as extraordinarily high electrical conductivity and large surface area, have been intensively studied as electrode materials for supercapacitor applications. However, graphene sheets tend to restack due to the strong π - π interactions and van der Waals forces between them, which make it difficult for ions to gain access to the inner layer graphene to form electric double layer, thus leading to a real value far below its intrinsic 550 F g⁻¹ calculated from graphene.

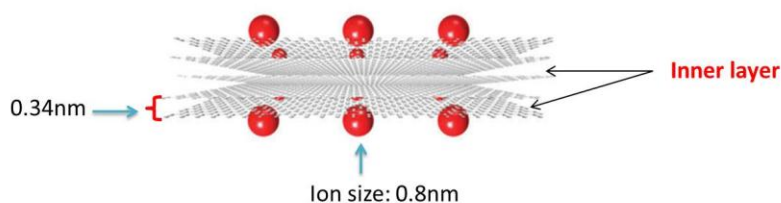


Figure 1-13 Schematic illustration of the restacking problem of graphene for absorbing electrolyte ions.

To address the serious restacking problem of graphene, we have proposed two main strategies. One is fabrication of novel self-separated graphene structures, another one is fabrication of separated graphene sheets.

- Fabrication of self-separated graphene structures to get maximum monolayer graphene. (i.e., graphene spheres)

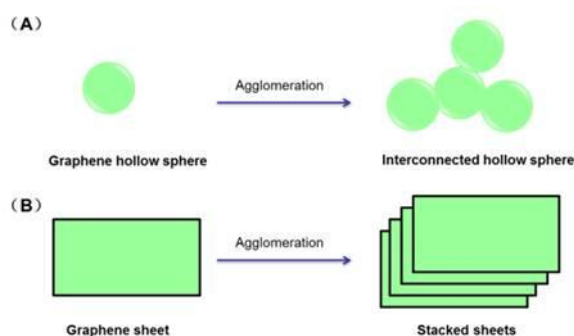


Figure 1-14 Schematic illustration of the non-stacked graphene spheres when they were scaled up.

The first strategy is fabrication of non-stacked graphene structures. In the present study, we have assembled successfully graphene nanosheets into hollow spherical shells and tested them as electrode material for supercapacitors. Compared with other reported planar graphene sheets, as shown in figure 1-14, the graphene hollow spheres are advantageous due to their unique features in structure: (1) the spherical graphene can significantly reduce large stacks of graphene sheets and offers more accessible surface area available for ions adsorption; (2) there are more free space between graphene spheres, which can make the graphene shells fully wetted by electrolyte; (3) the graphene spheres are interconnected, which would enhance electric conduction.

- Fabrication of separated graphene sheets with larger interlayer spacing for sufficient accessibility of electrolyte ions. (i.e., graphene sheets were separated by carbon nanotubes)

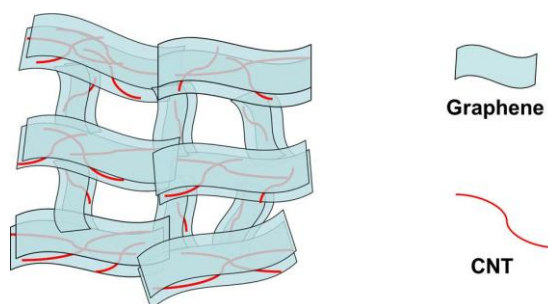


Figure 1-15 Schematic illustration of carbon nanotube spaced graphene aerogels with combined macro and micro 3D structure.

The second strategy is fabrication of separated graphene sheets with larger interlayer spacing for sufficient accessibility of electrolyte ions. Here, for the first time, we realize a graphene structure with both macro and micro 3D structures. We use carbon nanotube as a spacer to prevent the restacking in graphene aerogels, which would result in a macro-porous aerogel structure with separated graphene walls, and thus provide both macropores and mesopores created by the carbon nanotube spacers. The combined effect of the macro-porous structure and the SWCNTs spacer in this

composite aerogel are : (i) The 3D macro-porous structure provides numerous large pores to make the electrode be wetted quickly by the electrolyte to ensure high rate performance; (ii) The SWCNTs are placed between the graphene layers to prevent the restacking of graphene sheets and more accessible surface area is made available for ion adsorption; (iii) The introduction of highly conductive SWCNTs can also reduce the resistance of the SSGA electrode to further increase the rate capability and promote stable cycling performance

References

1. P. Simon and Y. Gogotsi, *Nature materials*, 2008, **7**, 845-854.
2. M. F. El-Kady, V. Strong, S. Dubin and R. B. Kaner, *Science*, 2012, **335**, 1326-1330.
3. B.E. Conway, *Electrochemical Supercapacitors: Scientific Fundamentals and Technological Applications*, Kluwer Academic/Plenum, New York, 1999.
4. M. Inagaki, H. Konno and O. Tanaike, *Journal of Power Sources*, 2010, **195**, 7880-7903.
5. G. A. Snook, P. Kao and A. S. Best, *Journal of Power Sources*, 2011, **196**, 1-12.
6. Y. B. Tan and J.-M. Lee, *Journal of Materials Chemistry A*, 2013, **1**, 14814.
7. X.-L. Wu and A.-W. Xu, *Journal of Materials Chemistry A*, 2014, **2**, 4852.
8. L. Borchardt, M. Oschatz and S. Kaskel, *Materials Horizons*, 2014, **1**, 157.
9. Z.-S. Wu, G. Zhou, L.-C. Yin, W. Ren, F. Li and H.-M. Cheng, *Nano Energy*, 2012, **1**, 107-131.
10. G. Wang, H. Wang, X. Lu, Y. Ling, M. Yu, T. Zhai, Y. Tong and Y. Li, *Advanced materials*, 2014, **26**, 2676-2682, 2615.
11. X. Tao, J. Du, Y. Li, Y. Yang, Z. Fan, Y. Gan, H. Huang, W. Zhang, L. Dong and X. Li, *Advanced Energy Materials*, 2011, **1**, 534-539.
12. Q. Zhang, J. Rong, D. Ma and B. Wei, *Energy & Environmental Science*, 2011, **4**, 2152.
13. G. Milczarek, A. Ciszewski and I. Stepniak, *Journal of Power Sources*, 2011, **196**, 7882-7885.
14. C.-L. Liu, W. Dong, G. Cao, J. Song, L. Liu and Y. Yang, *Journal of The Electrochemical Society*, 2008, **155**, F1.
15. Y. Wei, H. Liu, Y. Jin, K. Cai, H. Li, Y. Liu, Z. Kang and Q. Zhang, *New Journal of Chemistry*, 2013, **37**, 886.
16. W. Li, F. Zhang, Y. Dou, Z. Wu, H. Liu, X. Qian, D. Gu, Y. Xia, B. Tu and D. Zhao, *Advanced Energy Materials*, 2011, **1**, 382-386.
17. Y. G. Wang, H. Q. Li and Y. Y. Xia, *Advanced materials*, 2006, **18**, 2619-2623.
18. C.-W. Huang, C.-H. Hsu, P.-L. Kuo, C.-T. Hsieh and H. Teng, *Carbon*, 2011, **49**, 895-903.
19. H. Jiang, L. Yang, C. Li, C. Yan, P. S. Lee and J. Ma, *Energy & Environmental Science*, 2011, **4**, 1813.
20. Z. Lei, N. Christov and X. S. Zhao, *Energy & Environmental Science*, 2011, **4**, 1866.

21. D. Feng, Y. Lv, Z. Wu, Y. Dou, L. Han, Z. Sun, Y. Xia, G. Zheng and D. Zhao, *Journal of the American Chemical Society*, 2011, **133**, 15148-15156.
22. M. Li, J. Ding and J. Xue, *Journal of Materials Chemistry A*, 2013, **1**, 7469.
23. J. Zhou, J. He, C. Zhang, T. Wang, D. Sun, Z. Di and D. Wang, *Materials Characterization*, 2010, **61**, 31-38.
24. K. Wilgosz, X. Chen, K. Kierzek, J. Machnikowski, R. J. Kalenczuk and E. Mijowska, *Nanoscale research letters*, 2012, **7**, 269.
25. S. Murali, D. R. Dreyer, P. Valle-Vigon, M. D. Stoller, Y. Zhu, C. Morales, A. B. Fuertes, C. W. Bielawski and R. S. Ruoff, *Physical chemistry chemical physics : PCCP*, 2011, **13**, 2652-2655.
26. L. Dai, D. W. Chang, J. B. Baek and W. Lu, *Small*, 2012, **8**, 1130-1166.
27. Y. Huang, J. Liang and Y. Chen, *Small*, 2012, **8**, 1805-1834.
28. J. W. Liu, S. Y. Zhang, H. Qi, W. C. Wen and S. H. Yu, *Small*, 2012, **8**, 2412-2420.
29. L. Liu, Z. Niu, L. Zhang and X. Chen, *Small*, 2014, **10**, 2200-2214.
30. B. Luo, S. Liu and L. Zhi, *Small*, 2012, **8**, 630-646.
31. K. Wang, H. Wu, Y. Meng and Z. Wei, *Small*, 2014, **10**, 14-31.
32. J. Zhang, F. Zhao, Z. Zhang, N. Chen and L. Qu, *Nanoscale*, 2013, **5**, 3112-3126.
33. X. Zhao, B. M. Sanchez, P. J. Dobson and P. S. Grant, *Nanoscale*, 2011, **3**, 839-855.
34. C. Zhu and S. Dong, *Nanoscale*, 2013, **5**, 1753-1767.
35. E. Frackowiak, *Physical chemistry chemical physics : PCCP*, 2007, **9**, 1774-1785.
36. J. Hou, Y. Shao, M. W. Ellis, R. B. Moore and B. Yi, *Physical chemistry chemical physics : PCCP*, 2011, **13**, 15384-15402.
37. V. Singh, D. Joung, L. Zhai, S. Das, S. I. Khondaker and S. Seal, *Progress in Materials Science*, 2011, **56**, 1178-1271.
38. T. Kuilla, S. Bhadra, D. Yao, N. H. Kim, S. Bose and J. H. Lee, *Progress in Polymer Science*, 2010, **35**, 1350-1375.
39. N. Li, M. Cao and C. Hu, *Nanoscale*, 2012, **4**, 6205-6218.
40. N. Mathews, B. Varghese, C. Sun, V. Thavasi, B. P. Andreasson, C. H. Sow, S. Ramakrishna and S. G. Mhaisalkar, *Nanoscale*, 2010, **2**, 1984-1998.
41. T. K. Nielsen, F. Besenbacher and T. R. Jensen, *Nanoscale*, 2011, **3**, 2086-2098.
42. W. I. Park, C. H. Lee, J. M. Lee, N. J. Kim and G. C. Yi, *Nanoscale*, 2011, **3**, 3522-3533.
43. W. Scharl, *Nanoscale*, 2010, **2**, 829-843.
44. Q. Tang, Z. Zhou and Z. Chen, *Nanoscale*, 2013, **5**, 4541-4583.
45. H. B. Wu, J. S. Chen, H. H. Hng and X. W. Lou, *Nanoscale*, 2012, **4**, 2526-2542.
46. Y. Xia, Z. Yang and R. Mokaya, *Nanoscale*, 2010, **2**, 639-659.
47. J. Xiao and S. Yang, *Nanoscale*, 2012, **4**, 54-65.
48. S. S. Yu and W. T. Zheng, *Nanoscale*, 2010, **2**, 1069-1082.
49. C. Z. Yuan, B. Gao, L. F. Shen, S. D. Yang, L. Hao, X. J. Lu, F. Zhang, L. J. Zhang and X. G. Zhang, *Nanoscale*, 2011, **3**, 529-545.

50. S. Guo and S. Dong, *Chemical Society reviews*, 2011, **40**, 2644-2672.
51. X. Huang, X. Qi, F. Boey and H. Zhang, *Chemical Society reviews*, 2012, **41**, 666-686.
52. G. Wang, L. Zhang and J. Zhang, *Chemical Society reviews*, 2012, **41**, 797-828.
53. L. L. Zhang and X. S. Zhao, *Journal of Materials Chemistry*, 2010, **20**, 5983-5992.
54. S. Pei and H.-M. Cheng, *Carbon*, 2012, **50**, 3210-3228.
55. M. D. Stoller, S. Park, Y. Zhu, J. An and R. S. Ruoff, *Nano letters*, 2008, **8**, 3498-3502.
56. R. S. Ruoff.
57. W. Gao, N. Singh, L. Song, Z. Liu, A. L. Reddy, L. Ci, R. Vajtai, Q. Zhang, B. Wei and P. M. Ajayan, *Nature nanotechnology*, 2011, **6**, 496-500.
58. P. Chen, H. Chen, J. Qiu and C. Zhou, *Nano Research*, 2010, **3**, 594-603.
59. Z.-S. Wu, D.-W. Wang, W. Ren, J. Zhao, G. Zhou, F. Li and H.-M. Cheng, *Advanced Functional Materials*, 2010, **20**, 3595-3602.
60. H. Wang, Q. Hao, X. Yang, L. Lu and X. Wang, *Electrochemistry Communications*, 2009, **11**, 1158-1161.
61. J. Xu, K. WANG, S. Zu, B. Han and Z. wei, *ACS nano*, 2010, **4**, 5019-5026.
62. J. J. Yoo, K. Balakrishnan, J. Huang, V. Meunier, B. G. Sumpter, A. Srivastava, M. Conway, A. L. Reddy, J. Yu, R. Vajtai and P. M. Ajayan, *Nano letters*, 2011, **11**, 1423-1427.
63. Y. Shao, H. Wang, Q. Zhang and Y. Li, *NPG Asia Materials*, 2014, **6**, e119.

Chapter 2

Experimental Technique

2.1 Electrochemical testing methods

2.1.1 Cyclic voltammetry

Cyclic voltammetry is a widely used technique by electrochemists because of its versatility. At the laboratory or materials scale it is an accurate technique that enables:

- Qualitative and pseudo-quantitative studies
- Kinetic analysis by scanning a huge range of scan rates
- Voltage window determination

The principle of this technique is to apply a linear voltage ramp to an electrode (or a device) between two voltage limits and to measure the resulting current. For a capacitor, with capacitance C , discharge Q , voltage V and current I , we can simply measure the capacitance:

$$CV = Q = \int I dt$$

Thus, for an ideal capacitor, with constant capacitance for a given constant sweep rate, we expect the current to be measured constant. Figure 2-1 shows typical CV response. An ideal capacitor will have a box-like curve, immediately responding to a change in the voltage ramp, and maintaining a constant current. A material undergoing corrosion, will exhibit Faradiac peaks at potentials corresponding to the corrosion potentials.

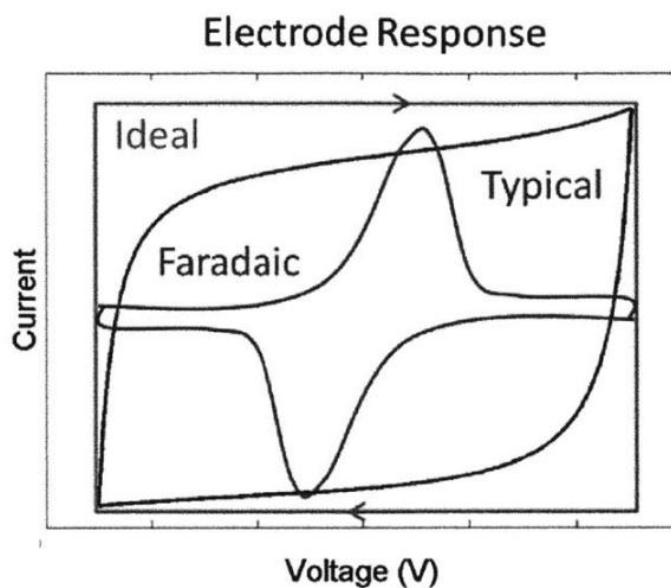


Figure 2-1 Typical cyclic voltammetry curves of electrical double-layer capacitor and pseudo-capacitor. [1]

Cyclic voltammetry is also useful to evaluate the cyclability of a supercapacitor (or an electrode), and the variation in capacitance on cycling would give a good idea of how things will go. But, usually, galvanostatic cycling is better when performing such experiments.

2.1.2 Galvanostatic charge and discharge

This technique is very different from cyclic voltammetry because the current is controlled and the voltage is measured. [2] This is certainly the most widely used technique in the supercapacitor field because it can be extended from a laboratory scale to an industrial one. This method is also called chronopotentiometry and gives access to different parameters such as:

- Capacitance
- Resistance
- Cyclability

The voltage variation is described by the following equation:

$$V(t) = Ri + \frac{t}{C}i \text{ (V)}$$

The voltage variation of a supercapacitor is represented in Figure 2.2:

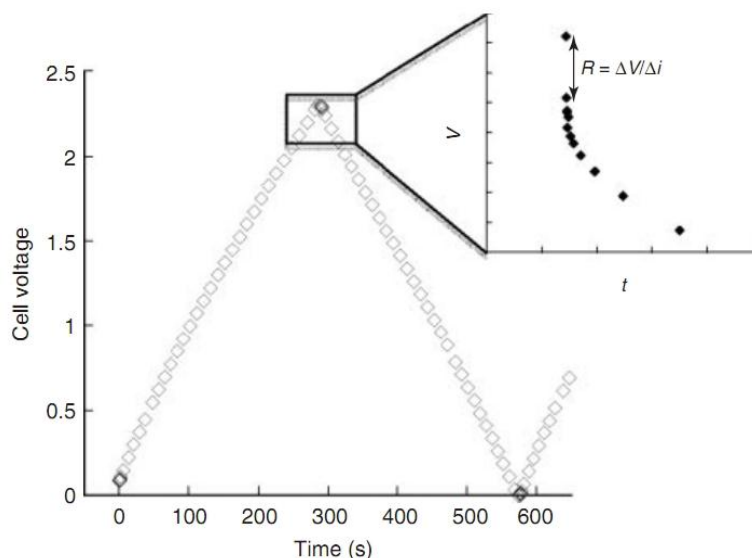


Figure 2-2 Typical charge-discharge curve of a supercapacitor. [1]

As can be seen from Eq. (2.3), the capacitance of a supercapacitor can be calculated from the slope of the curve; for a pseudocapacitor, when the V-t curve profile is not as linear as it should be, the capacitance can be calculated by integrating the current over the discharge time or charge time:

$$C = \frac{I\Delta t}{\Delta V}$$

Where I is the set current, Δt is the discharge time (or charge time), and ΔV is the voltage window.

The series resistance is deduced from the voltage drop (V_{drop}) occurring over the current inversion (Δi); it is illustrated in the inset of Figure 2.2:

$$R = \frac{V_{\text{drop}}}{\Delta I}$$

When the current is inversed or interrupted, the voltage drop is directly linked to the resistance of the cell. By repeating both capacitance and resistance measurements over cycling, it is then also possible to watch the cyclability of supercapacitors (electrical double-layer capacitors and pseudocapacitors).

2.1.3 Electrochemical impedance spectroscopy

Electrochemical impedance spectroscopy (EIS) allows covering a large timescale (from microseconds to hours), meaning that electrochemical processes are parted depending on their own time constant. In addition, such measurements are made under steady-state conditions that allow acquisition times high enough to get accurate measurements. In contrast to the previous techniques, small excitation signals are employed, permitting linearization of current-voltage characteristics. Actually, this means that this technique can be carried out by controlling either the current or the voltage, thus measuring either the voltage or the current. Here, the voltage control technique is focused on, but the same remarks or conclusions could be driven by controlling the current.

The use of complex-plane plot, or Nyquist plot, to represent the impedance behavior as a function of frequency has often been used to evaluate the frequency response of supercapacitors. In

the complex-plane, the imaginary component, Z_2 , is usually used to represent the capacitive parameter and the Z_1 (the real component) represents the ohmic parameter. The two components are all studied under a certain frequency range. These kinds of plots usually consist of one or more semicircles in the complex plane, sometimes with the center of a semicircle depressed below the Z_1 axis. The theoretical Nyquist plot of a supercapacitor consists of three regions which are dependent on the frequencies. At very high frequency, the supercapacitor behaves like a pure resistor. At low frequency, the imaginary part sharply increases and a vertical line is observed, indicating a pure capacitive behavior. In the middle frequency domain, the influence of the electrode porosity can be observed. When the frequency decreases, starting from the very high frequency, the signal penetrates deeper and deeper inside the porous structure of the electrode, then more and more electrode surface is available for the ion adsorption. This middle frequency range is related to the electrolyte penetration inside the porous structure of the high porosity electrodes and this region is usually called Warburg curve.

2.2 Electrochemical testing configuration

2.2.1 Two-electrode test configuration

A typical two-electrode test configuration is comprised of two electrodes that are isolated from electrical contact by a porous separator. Electrodes often contain conductive, low surface area additives such as carbon black to improve electrical conductivity. Current collectors of metal foil or carbon filled polymers are used to conduct electrical current from each electrode. The separator and the electrodes are impregnated with an electrolyte, which allows ionic current to flow between the electrodes while preventing electronic current from discharging the cell. A packaged supercapacitor module, depending upon the desired size and voltage, is constructed of multiple repeating unit cells. Two-electrode test configuration are either available commercially or can be easily fabricated from two stainless steel plates. [3]

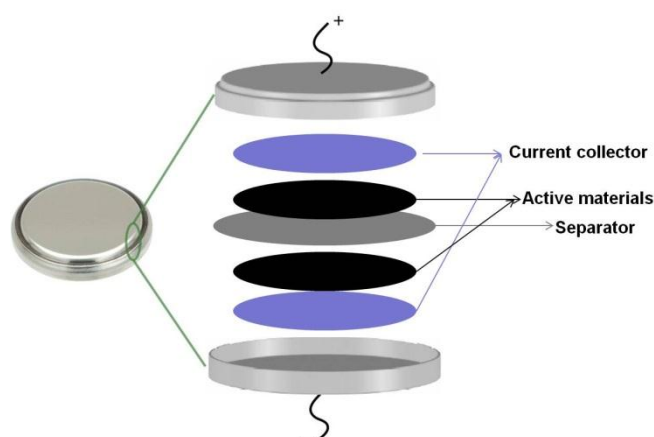


Fig.2-3 Illustration of the two-electrode test configuration

2.2.2 Three-electrode test configuration

Three-electrode test configuration is commonly used in electrochemical research and consist of a working electrode (WE), a reference electrode (RE), and a counter electrode (CE). In this setup, the current flows between the CE and the WE. The potential difference is controlled between the WE and the CE and measured between the RE (kept at close proximity of the WE) and Sense. By controlling the polarization of the CE, the potential difference between RE and WE is controlled all the time. The potential between RE and WE is usually not measured. This is the voltage applied by the control amplifier and it is limited by the compliance voltage of the instrument. It is adjusted so that the potential difference between the WE and the RE will be equal to the potential difference specified by the user. This configuration allows the potential across the electrochemical interface at the WE to be controlled with respect to the RE. [3]

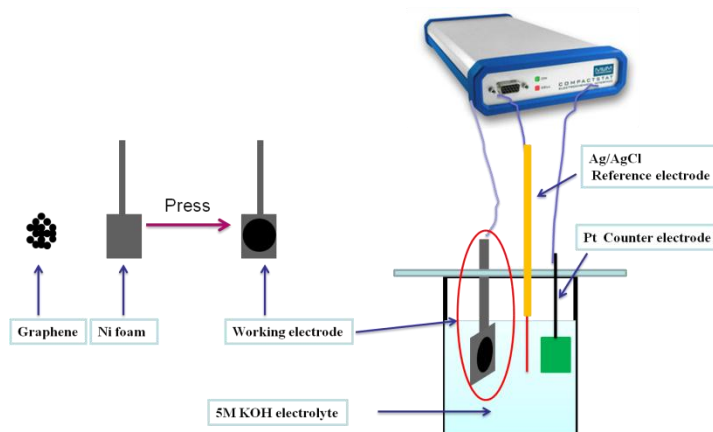


Fig.2-4 Illustration of the three-electrode test configuration

2.3 Summary of the testing technique

A three-electrode test system is very useful for determining the electrochemical properties of a single electrode. A two-electrode test system is the best construction which can mimics the real packaged supercapacitor that can be characterize the energy density, power density and cycling property of a practical supercapacitor. For good signal to noise and to noise and to minimize measurement errors, the test cell should have a capacity larger than 0.25 F.

References

1. B.E. Conway, *Electrochemical Supercapacitors: Scientific Fundamentals and Technological Applications*, Kluwer Academic/Plenum, New York, 1999
2. M. D. Stoller, S. Park, Y. Zhu, J. An and R. S. Ruoff, *Nano letters*, 2008, **8**, 3498-3502.
3. M. D. Stoller and R. S. Ruoff, *Energy & Environmental Science*, 2010, **3**, 1294.

Chapter 3

Synthesis and Characterization of Graphene Hollow Spheres for Application in Supercapacitors

3.1 Introduction

Due to its exceptional physical, chemical, and mechanical properties, graphene, a one-atom-thick two-dimensional carbon material, has been a promising candidate for a broad range of applications. Graphene offers large specific surface area, high conductivity, excellent mechanical flexibility and outstanding chemical stability. These characteristics make graphene an attractive electrode material for supercapacitors[1-5]. Stoller et al. reported first that chemically modified graphene can deliver a specific capacitance of 135 F/g and 99 F/g in aqueous and organic electrolytes, respectively[6]. However, the graphene sheets tend to restack due to the strong π - π interactions and van der Waals forces between them, which cause significant decrease in the electrochemically active surface area and the inter-graphene channels accessible to electrolyte, leading to lower specific capacitance[7]. Therefore, a key issue in graphene supercapacitors is to reduce the agglomeration of graphene sheets during its processing in assembling them into macroscopic structures for device applications. Up to now, there have emerged several strategies to prevent the restacking of graphene sheets, among which the idea of adding a spacer between graphene sheets seems to be most effective and promising. For example, Cheng et al. has explored using single-walled carbon nanotubes as spacer to reduce agglomeration of graphene sheets and found that the electrochemical properties of the composite graphene electrodes were indeed much improved [8].

As we all know, the properties of functional materials are greatly depended on its structures especially when the materials are in the nanoscale. In the recent years, a large number of materials can be controlled synthesized with a sphere-like morphology, such as carbon, polymer, ceramics, oxides, alloys, metals, and these sphere-structured materials show enhanced a broad range of applications, including energy storage, sensor, catalysis, environment, biology and so on. At the same time, graphene nanosheets have been assembled into various tailored macroscopic graphene structures, such as porous films, flowers, networks, and hydrogels, to improve their electrochemical

performances [9-12]. However, graphene hollow spheres have not been investigated till now. There are some expected features about graphene spheres, for example, graphene spheres should have lower stacking, and it should also possess porous macrostructure, favorable pore distribution and ultra-light density. These features would benefit a lot when they were used for supercapacitor application.

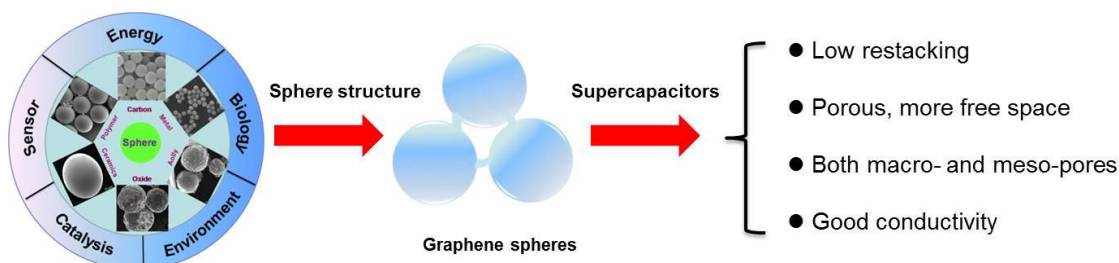


Fig. 3-1 Illustration of the proposed graphene spheres and their features.

In the present study, we have assembled successfully graphene nanosheets into hollow spherical shells and tested them as electrode material for supercapacitors. Compared with planar stacked graphene sheets, the hollow spherical graphene shells can provide more free space between the spheres and therefore reduce effectively restacking of graphene sheets. More accessible surface area will also be produced for ion adsorption. Electrochemical characterization shows that the graphene hollow spheres exhibit impressive specific capacitance of 273 F g^{-1} at a low current density of 0.5 A g^{-1} and 197 F g^{-1} at a high current density of 10 A g^{-1} , respectively. Moreover, when it was charged and discharged repeatedly at a high current density of 10 A g^{-1} , 95% of its initial capacitance was retained even after 5000 cycles. These findings indicate that the graphene hollow spheres are promising as electrode material for supercapacitors.

3.2 Experimental section

3.2.1 Synthesis of positively charged PS sphere

The positively charged polystyrene (PS) spheres were prepared by a dispersive polymerization approach[13]. In this work, 20 mL of styrene monomers and 0.5 g of PVP were added to 100 mL of deionized water in a 250 mL flask in water bath. After stirring at 400 rpm for 30 min, 0.2 g of AIBA dissolved in 20 mL of deionized water was added. The mixture was deoxygenated by bubbling nitrogen gas for 30 min, and then it was kept at $70 \text{ }^\circ\text{C}$ for 24 hours before cooling to room temperature. After the reaction completed, products were centrifuged with methanol and deionized water and dried in an oven over night.

3.2.2 Synthesis of PS@graphene core-shell spheres

Graphene oxide was synthesized from natural graphite flakes by a modified Hummers method[14]. Specifically, 30 mg of graphene oxide powders and 70 mg of PS spheres were dissolved

in 50 mL deionized water separately aided by sonication. The two solutions were then mixed together and sonicated for another hour. The mixture was heated to 100 °C and 0.5 mL of hydrazine hydrate was added in. The reaction was kept going at 98 °C for 6 more hours. The product was harvested by centrifugation and washed with deionized water before drying in an oven over night.

3.2.3 Synthesis of graphene hollow spheres

The above prepared PS@graphene core-shell spheres were placed at the center of a tube furnace and were heated to 420 °C with a heating rate of 5 °C per minute and maintained at this temperature in air for 2 hours.

3.2.4 Structural characterization

The material morphology and structure were examined with field-emission scanning electron microscope (FE-SEM, JSM-6500, JEOL, Japan) and transmission electron microscope (TEM, JEM-2100, JEOL, Japan). Powder X-ray diffraction (XRD) patterns were recorded with Rigaku RINT 2500. Raman spectra were obtained with RAMAN-11 (Nanophoton) with a 532 nm laser source. Thermogravimetric analyses (TG) were performed on SDTA851e Analyzer at a heating rate of 10 °C/min in air. The specific surface area and pore size distribution were measured with AUTOSORB of Quantachrome Instruments.

3.2.5 Electrochemical characterization

The electrochemical properties of graphene hollow spheres were investigated using a three-electrode test system[15]. The working electrode was fabricated by mixing the prepared powders with 10 wt% polytetrafluorene-ethylene (PTFE) binder. The mixture was pressed onto nickel foam to make electrodes. A platinum foil and a saturated Ag/AgCl electrode were used as the counter and the reference electrode, respectively. A 5 M KOH solution was used as the electrolyte. Cyclic voltammetry, galvanostatic charge-discharge, and electrochemical impedance spectroscopy were performed on an EC-lab electrochemical workstation. Specific capacitance ($F\ g^{-1}$) of the electrode was obtained from the discharge process according to the following equation

$$C_g = \frac{I \times \Delta t}{m \times \Delta V}$$

where I is the loaded current (A), Δt is the discharge time (s), ΔV is the potential drop during discharge, and m is the mass of active material in a single electrode (g).

3.3 Results and discussion

Figure 3-2 illustrates the preparation of the spherical graphene shells. The synthesis consists of two steps: (i) formation of PS@graphene core-shell spheres and (ii) removal of PS template spheres. Positively charged PS spheres were first prepared by a solution polymerization method using AIBA as initiator. Then they were mixed with negatively charged graphene oxide nanosheets. Due to the electrostatic attraction the graphene oxide nanosheets would wrap around the PS spheres. After being

reduced by hydrazine, the PS@graphene core-shell structure was produced. At last, the PS template spheres were removed by heat treatment and graphene hollow spheres were obtained.

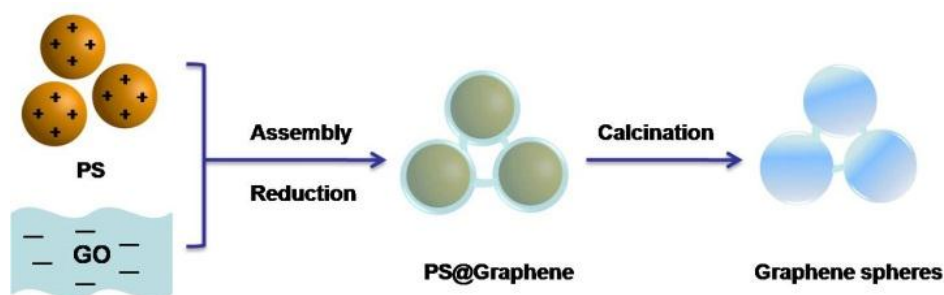


Fig. 3-2 Illustration of preparation process of graphene hollow spheres.

Figure 3-3 shows SEM images of the as-prepared (A) PS spheres, (B) PS@graphene core-shell spheres, and (C) graphene hollow spheres. As can be observed in Fig. 3-3(A), the PS spheres are not only mono-dispersed with an average diameter of ~ 290 nm but also have smooth surfaces. Fig. 3-3(B) is a typical SEM image of the PS@graphene core-shell spheres. It can be clearly seen that the graphene nanosheets are uniformly coated on the surface of PS spheres, leading to a core-shell structure. In addition, it should be pointed out that the electrostatic attraction between the GO sheets and the PS spheres plays a key role in the formation of the core-shell structure. Fig. 3-3(C) shows the final graphene hollow spheres, after removing the PS template, and the spherical geometry was retained. The SEM image also indicates that the graphene layers were very thin.

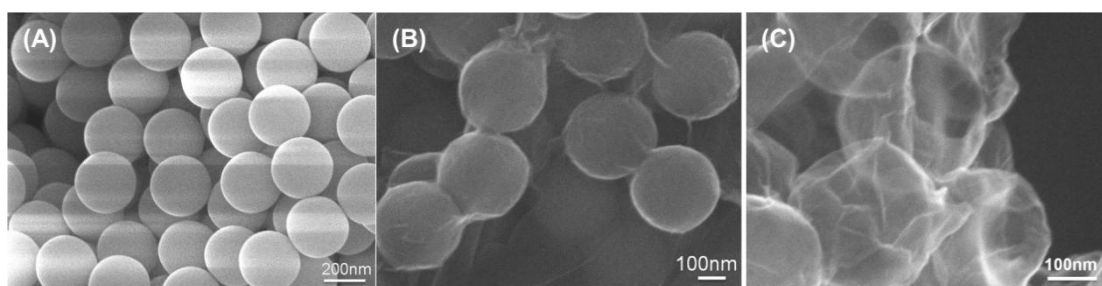


Fig. 3-3 SEM images of as prepared structures: (A) PS spheres, (B) PS@Graphene core-shell spheres, and (C) graphene spherical shells after removing the PS sphere in the core.

The morphology and structure of the PS@graphene core-shell spheres and the graphene hollow spheres were also characterized with TEM. Fig. 3-4(A) and (B) display representative TEM images of PS@graphene core-shell spheres. In Fig. 3-4(A) we can find that the neighboring spheres are linked together by a thin sheet, which provides direct visual evidence for the presence of graphene nanosheets. Besides, the rough surface of one core-shell sphere shown in Fig. 3-4(B) confirms the graphene coating. Fig. 3-4(C) shows a TEM image at low magnification of the spherical graphene.

Nearly all the graphene spheres show a hollow structure. The enlarged TEM image (Fig. 3-4(D)) reveals that the diameter of the hollow spheres is about 300 nm and the shell thickness is about 8 nm.

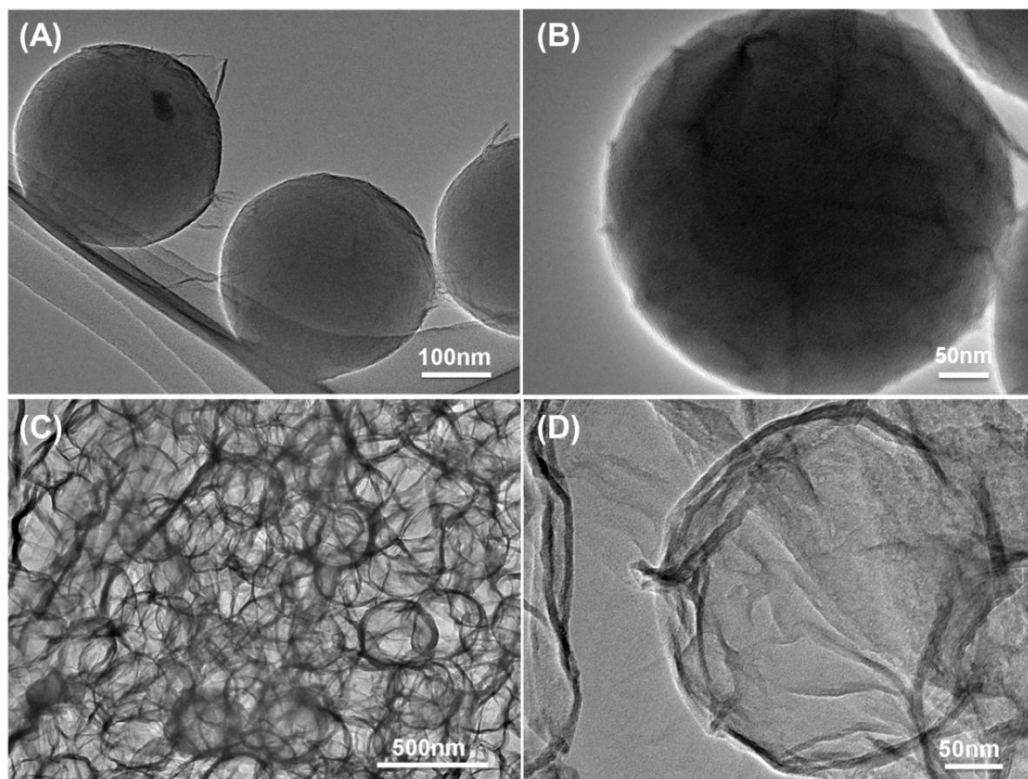


Fig. 3-4 TEM images of (A-B) PS@graphene core-shell spheres and (C-D) graphene hollow spheres.

Figure 3-5 shows the XRD patterns of graphite (green), graphite oxide (blue), and graphene spheres (red). For the pristine graphite the Bragg peak at $2\theta = 26.2^\circ$ is due to the (002) reflection with an interlayer spacing of 0.34 nm[16]. However, for graphite oxide this peak disappeared and a broader reflection peak appeared at $2\theta = 10.0^\circ$, corresponding to an interlayer spacing of 0.89 nm, which is attributed to the intercalation of certain oxygen functional groups. After having been reduced by hydrazine, the XRD pattern of graphene spheres shows a typical broad peak at $2\theta = 24.1^\circ$, corresponding to an interlayer spacing of 0.36 nm, which is a little larger than that of graphite. These results indicate that the graphene spheres were highly reduced, resulting a new structure which is significantly different from the pristine graphite and graphite oxide.

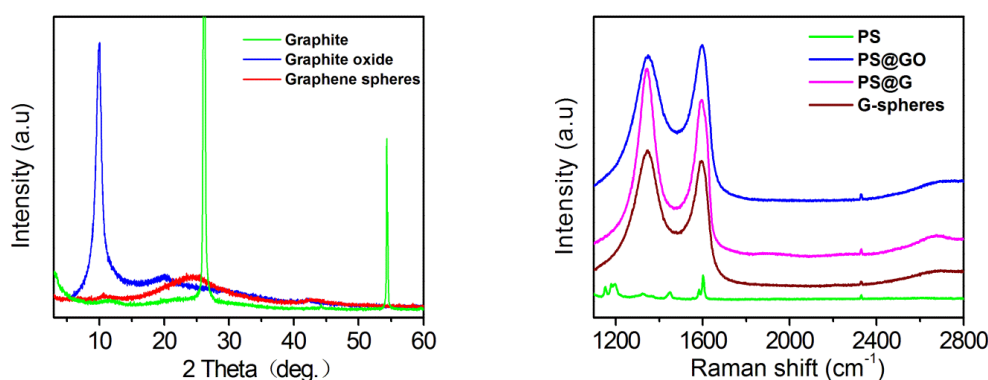


Fig. 3-6 (A) XRD patterns of graphite, graphite oxide, and graphene spheres; (B) FT-Raman spectrum of PS, PS@GO, PS@G, and graphene spheres.

The structural evolution of PS, PS@GO, PS@graphene, and graphene hollow spheres was also characterized by Raman spectroscopy as shown in Fig. 3-6. The Raman spectrum of PS spheres shows three weak characteristic peaks at 1180, 1450, and 1610 cm^{-1} , and these weak signals were attenuated or absorbed when the PS spheres were wrapped by graphene oxide or graphene. As for the Raman spectrum of PS@GO, PS@graphene and graphene hollow spheres, the two intense features are the D band at 1340 cm^{-1} and the G band at 1590 cm^{-1} .

The D band is associated with disorder arising from structural defects, while the G band corresponds to the first-order scattering of the stretching vibrational mode E_{2g} observed due to the sp^2 bonded carbon domains[17]. Generally, the intensity ratio of D band to G band (I_D/I_G) indicates the degree of disorder. Compared with the spectrum of PS@GO, as shown in Fig. 3-5, I_D/I_G increased in the spectrum of PS@graphene. This occurs because of the increased number of structural defects after reduction. The ratio of I_D/I_G decreased a little from PS@graphene to graphene hollow spheres, which is attributed to the improved crystallinity of graphene by heat treatment.

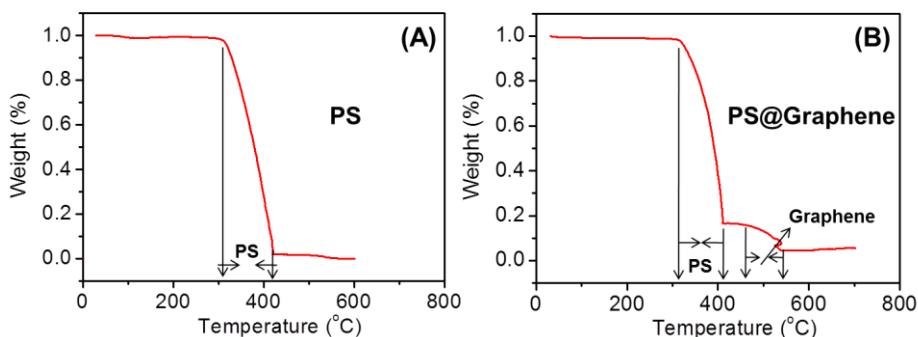


Fig. 3-7 TG curves of (A) PS spheres and (B) PS@graphene core-shell spheres. Gravimetric loss of graphene starts at 450 $^{\circ}\text{C}$.

Figure 3-7 shows the TG curves of PS spheres and PS@Graphene core-shell spheres. As shown

in Fig. 3-7(A), the PS spheres begin to decompose at 300 °C and were burned completely by 410 °C. However, as expected, the PS@graphene core-shell spheres showed a two-step process in weight loss (Fig. 3-7(B)), corresponding to the decomposition of PS cores starting at 300 °C and graphene shells starting at 450 °C, respectively. The graphene shells begin to decompose at about 450 °C. Therefore, in the case of our heat treatment at temperature of 420 °C, the PS spheres were removed while the graphene shells were retained.

The BET surface area of graphene hollow spheres was obtained from the nitrogen adsorption-desorption isotherms shown in Fig. 3-8. The isotherms (Fig.3-8(A)) exhibited a mixed type-II and V curve, indicating the presence of microporosity, mesoporosity, and macroporosity. A specific surface area of about 440 m² g⁻¹ for the as-prepared graphene hollow spheres was obtained by the BET measurement. The corresponding pore size distribution (Fig. 3-8(B)) exhibited an average pore diameter of 3.2 nm calculated by the DFT model.

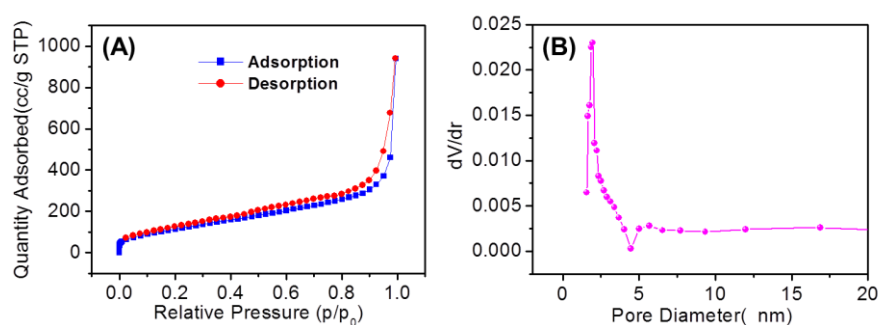


Fig. 3-8 Nitrogen sorption isotherms of (A) graphene hollow spheres and (B) the corresponding pore size distribution curve. Average diameter of pores is 3.2 nm.

The obtained graphene hollow spheres were also investigated as electrode material for supercapacitors. The electrochemical properties were tested using cyclic voltammetry (CV) and galvanostatic charge/discharge measurements within the potential window of -1 to -0.2 V in 5 M KOH aqueous solution. Fig. 3-9(A) shows the CV curves of graphene hollow spheres at scan rates of 10-50 mV/s. The curves are approximately rectangular in shape, indicating an excellent capacitive behaviour. Accordingly, the galvanostatic charge-discharge curves at various current densities in Fig. 3-9(B) are symmetric triangles without obvious potential drop (IR drop), confirming the characteristic electric double-layer capacitance. The calculated specific capacitance under different current densities is displayed in Fig. 3-9(C). Specific capacitance of 273, 244, 224, and 208 F g⁻¹ were obtained for the graphene hollow spheres at current densities of 0.5, 1.0, 2.0, and 5.0 A g⁻¹, respectively. Even charged and discharged at high current densities of 10 and 20 A g⁻¹, the graphene hollow spheres retained high specific capacitance of 197 and 183 F g⁻¹, respectively, highlighting excellent rate capability. In order to investigate the durability of the graphene hollow spheres, a repetitive charge-discharge cycling test was carried out at a high current density of 10 A g⁻¹ over 5000 cycles. As shown in Fig. 3-9(D), the graphene hollow spheres retained 95% of its initial capacitance even after 5000 cycles. This rate capability is much improved than many of previously

reported supercapacitor electrodes including nitrogen-modified graphene, CNT/graphene, MnO_2 /graphene, and Mn_3O_4 /graphene composite electrodes[18-21].

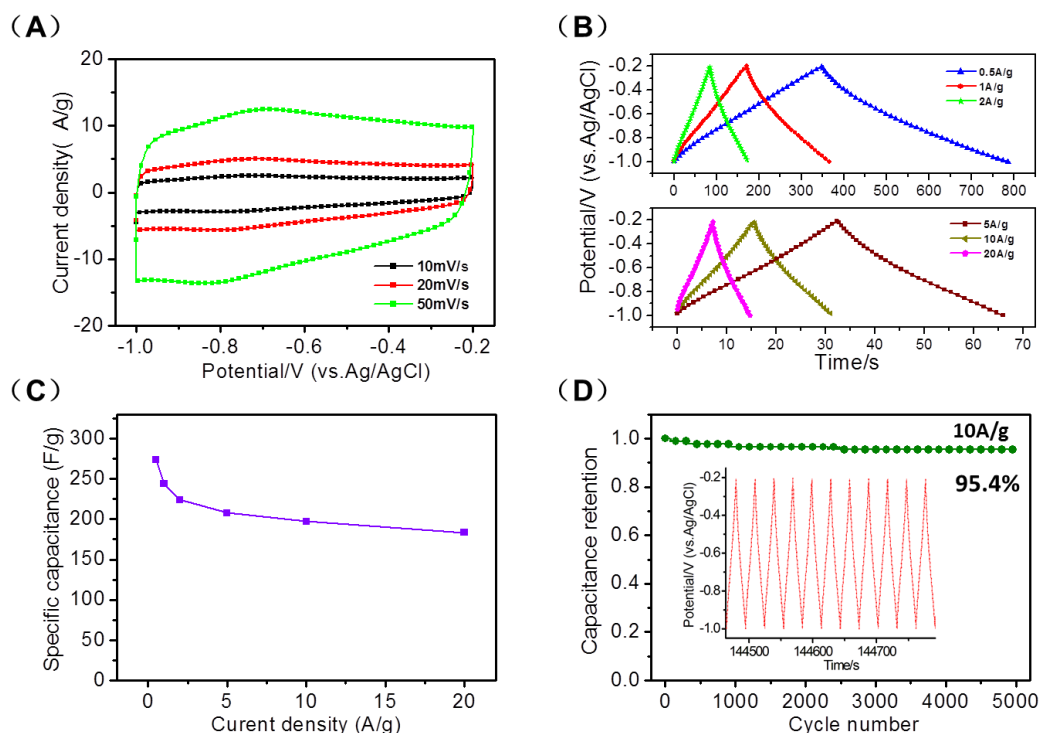


Fig. 3-9 Electrochemical characterization of as-prepared graphene hollow spheres. (A) Cyclic voltammograms at various scan rates, (B) Galvanostatic charge-discharge curves, (C) Corresponding specific capacitance at various current densities, and (D) Capacitance retention at a high current density of 10 A g^{-1} . (Inset is a portion of the charge-discharge curve after 40 hours.)

We attribute the outstanding capacitive behaviour of graphene hollow spheres to their unique spherical structure. Compared with planar graphene sheets, the graphene hollow spheres are advantageous due to their unique features in structure: (1) the spherical graphene can significantly reduce large stacks of graphene sheets and offers more accessible surface area available for ions adsorption; (2) there are more free space between graphene spheres, which can make the graphene shells fully wetted by electrolyte; and (3) the graphene spheres are interconnected, which would enhance electric conduction.

We also suggest that the graphene spheres reported in this work would find potential applications in other fields such as lithium ion batteries, electrochemical sensors, and oil absorption.

3.4 Conclusions

We have successfully fabricated spherical graphene shells using polystyrene spheres as templates. The as-prepared graphene hollow spheres were studied as electrode material for supercapacitors. Compared with stacked planar graphene, the graphene hollow spheres offer more free space between spheres, leading to larger accessible surface area for ion adsorption.

Electrochemical tests show that the graphene hollow spheres showed high specific capacitance of 273 F g⁻¹ at a current density of 0.5 A g⁻¹ and 197 F g⁻¹ at a higher current density of 10 A g⁻¹. After charge-discharge of 5000 cycles at a high current density of 10 A g⁻¹, the graphene hollow spheres retained 95% of its initial capacitance. These results demonstrate the graphene hollow spheres are a promising structure for supercapacitor applications.

References

1. Y.W. Zhu, S. Murali, W.W. Cai, X. Li, J. Suk, J. R. Potts and R. S. Ruoff, *Adv. Mater.*, 2010, **22**, 3906–3924.
2. K.S. Novoselov, A.K. Geim, S.V. Morozov, D. Jiang, Y. Zhang, S.V. Dubonos, I.V. Grigorieva and A.A. Firsov, *Science*, 2004, **306**, 666–669.
3. J.J. Wang, M.Y. Zhu, R.A. Outlaw, X.Zhao, D.M. Manos and B.C. Holloway, *Carbon*, 2004, **42**, 2867-2872.
4. S. William, J. Hummers and E. Richard, *J. Am. Chem. Soc.*, 1958, **80**, 1339–1339.
5. C. Daniela, Marcano, D.V. Kosynkin, J.M. Berlin, A. Sinitskii, Z. Sun, A. Slesarev, L.B. Alemany, W. Lu and M. James, *ACS Nano*, 2010, **4**, 4806–4814.
- 6 M.D. Stoller, S.J. Park, Y.W. Zhu, J.H. An and R.S. Ruoff, *Nano Lett.*, 2008, **8**, 3498-3502.
7. J. Yan, T. Wei, B. Shao, F.Q. Ma, Z.J. Fan, M.L. Zhang, C. Zheng, Y.C. Shang, W.Z. Qian and F. Wei, *Carbon*, 2010, **48**,1731–1737.
- 8 Q. Cheng, J. Tang, J. Ma, H. Zhang, N. Shinya and L.-C. Qin, *Phys. Chem. Chem. Phys.*, 2011, **13**, 17615-17624.
- 9 Z. Niu, J. Chen, H. H. Hang, J. Ma and X. Chen, *Adv. Mater.*, 2102, **24**, 4144–4150.
- 10 Y. Zhang, L.Y. Zhang, P. Kim, M.Ge, Z. Li and C.W. Zhou, *Nano Lett.*, 2012, **12**, 2810–2816
- 11 Z.P. Chen,W.C. Ren, L.B. Gao, B.L. Liu, S.F. Pei and H.M. Cheng, *Nature Mater.*, 2011, **10**, 424-428
- 12 Y.X. Xu, K.X. Sheng, C. Li and G.Q. Shi, *ACS Nano*, 2010, **4**, 4324–4330.
- 13 W.G Leng, M. Chen , S.X. Zhou and L. Wu , *Langmuir*, 2010, **26** ,14271–14275.
- 14 J.P. Zhao, S. F. Pei, W.C. Ren, L.B. Gao and H.M. Cheng, *ACS Nano*, 2010, **4**, 5245–5252.
- 15 Z. Lei, N. Christova and X.S. Zhao, *Energy Environ. Sci*, 2011, **4**, 1866-1873.
- 16 W.F. Chen and L.F. Yan, *Nanoscale*, 2011,**3**, 3132-3137
17. J. Zhang, Y. Yu, L.Liu and Y. Wu, *Nanoscale*, 2013, **5**, 3052-3057
18. Y. Qiu, X.g Zhang and S. Yang, *Phys. Chem. Chem. Phys.*, 2011, **13**, 12554-12558.
- 19 D. Zhang, T. Yan, L. Shi, Z. Peng, X. Wen and J. Zhang, *J. Mater. Chem.*, 2012, **22**, 14696-14704.
- 20 M. Lee, C. Fan, Y. Wang, H. Li, J. Chang and C. Tsengd, *J. Mater. Chem. A*, 2013, **1**, 3395.
- 21 J. Qu, F. Gao,Q. Zhou, and Z.Wang, *Nanoscale*, 2013, **5**, 2999-3005.

Chapter 4

Confining SnO₂ nanoparticles between multi-layered and interconnected graphene shells as binder-free anodes for high-capacity lithium-ion batteries

4.1 Introduction

Lithium-ion batteries (LIBs), as the power sources of portable electronic devices and upcoming electric vehicles, have received great attention in the recent years.[1-3] The current commercial graphite anode, due to its low theoretical capacity of 372 mAh g⁻¹, cannot meet the demands of future energy storage systems which require both high energy density and power density. Therefore, it has been an urgent issue to exploit new high capacity electrode materials to substitute the graphite anode. Transition metal oxides, such as TiO₂, Fe₂O₃, SnO₂, Co₃O₄, MoO₃, NiO have been studied as the anode materials for LIBs. [4-7] Among them, SnO₂ attracts particular interest because of its large theoretical capacity (782 mAh g⁻¹) and natural abundance. [8-10] However, SnO₂ anode suffers severe volume expansion (over 200%) during the Li⁺ insertion and extraction, which cause the pulverization of the electrodes and loss of interparticle contact, thus leading to a low specific capacity and poor cycling stability. [11-15]

Several approaches have been proposed to deal with the problem of the volume changes and improve the cycling stability of SnO₂ based anodes. One strategy is to decrease the particle size into the nanoscale, which could minimize the strain during the volume expansion. [16] Another strategy involves the fabrication of SnO₂ anode with desired hollow structures, including nanotubes, hollow spheres, and hollow boxes. The void space in these hollow structures can accommodate the volume changes and result in enhanced cycling performance. Beside these strategies, making a nanocomposite with a conductive matrix is also useful for buffering the volume expansion as well as improving the electrical conductivity. Among various conductive matrixes, graphene has attracted considerable attention due to its unique properties such as high electrical conductivity, large specific surface area, and broad electrochemical window. Many kinds of SnO₂/graphene composites, e.g.,

graphene mixed SnO₂ composites, graphene loaded SnO₂ composites, graphene wrapped SnO₂ composites, or graphene encapsulated SnO₂ composites, have been fabricated and show enhanced lithium storage properties. [17-23] However, graphene sheets in those composites are easily to form irreversible agglomerates and even restack to graphite due to the strong π - π interactions and van der Waals forces, which would make graphene lose its merits of large surface area and high electrical conductivity and consequently result in rapid capacity fading. So, it is still a challenge to uniformly load SnO₂ nanoparticles and carefully tailor graphene structures for better electrochemical performances.

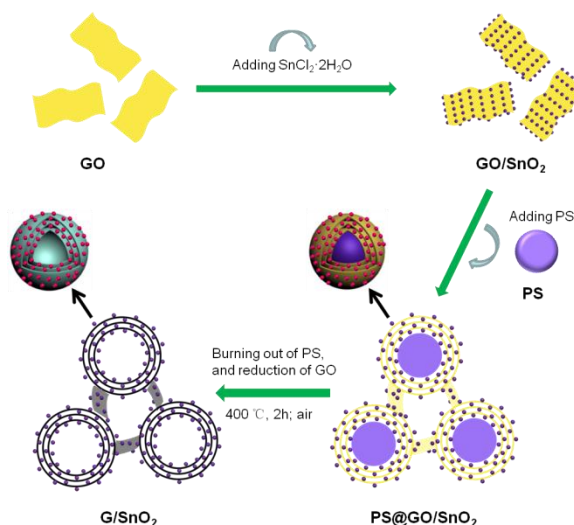


Fig. 4-1 Illustration of preparation process of graphene hollow spheres confined SnO₂ nanoparticles.

Recently, we have successfully assembled graphene nanosheets into interconnected graphene hollow spheres by a template method. The as prepared hollow spherical graphene materials provide more free space between each spheres and therefore reduce effectively restacking of graphene sheets. [24] Besides, the graphene spheres also exhibit high conductivity due to their interconnected features. Inspired by this work, here, we use the interconnected multi-layered graphene hollow spheres as a robust and high conductivity matrix to load SnO₂ nanoparticles, where the SnO₂ nanoparticles are confined between the multi-layered sheets of graphene hollow spheres. With this design, firstly, the volume changes of SnO₂ nanoparticles during the charging and discharging process can be restricted by the multi-layered graphene. Secondly, the graphene spheres can also serve as a non-stacked high conductive substrate to facilitate Li⁺ and electron transport. Thirdly, the interconnected nature of graphene hollow spheres makes the electrode can be self-assembled together eliminating the need of any binders which could lower the conductivity and increase weight of the whole electrode. Electrochemical tests show that the as designed unique graphene/SnO₂ composite exhibit a large reversible capacity of 1001 mAh/g and excellent long cycling life with 85% retention even after 100 cycles, indicating its great potential as high performance anode materials for lithium-ions batteries.

4.2 Experimental section

4.2.1 Synthesis of graphene oxide (GO)

Graphene oxide was synthesized from natural graphite flakes by a modified Hummers method. Briefly, 3.0 g of graphite powder and 1.5 g sodium nitrate were mixed with 70 mL 98 wt % sulfuric acid in an ice-bath. After stirring 5 min, 9.0 g potassium permanganate was added gradually, and the temperature was kept below 20 °C. The reaction system was transferred to a 35 °C water bath for 1 h, forming a thick paste. Successively, 140 mL of deionized water slowly added into the pasty mixture. The mixture was stirred for another 1 h. After dilution with 500 mL water, 20 mL of 30% H₂O₂ was slowly added and the color changed from dark brown to yellow. The suspension was centrifuged and washed with 10 % HCl solution and deionized water several times to remove the metal ions and acid. The obtained products were dried under vacuum to get GO powders.

4.2.2 Synthesis of polystyrene (PS) spheres

The PS spheres were synthesized according to the literature using styrene as monomer, AIBA as initiator. In a typical process, 0.5 g of PVP and 20 mL of styrene were first added to a 250 mL flask containing 100 mL of deionized water. Then, the reaction flask was heated to 70 °C. After stirring for 30 min, 0.2 g of AIBA dissolved in 20 mL of deionized water was added. After the reaction of 24 h, the product was centrifuged with deionized water for several time and dried in an oven overnight.

4.2.3 Synthesis of PS@SnO₂/graphene oxide multi-layered spheres

The synthesis was conducted as follows: 20 mg of PS was dispersed in 50 mL of deionized water to form solution A. 20 mg of GO, 40 mg of SnCl₂•2H₂O, and 1 mL of HCl (37% wt%) were dispersed in 50 mL of deionized water to form solution B. Subsequently, the solution B was added into the solution A under vigorous stirring. Then the mixed solution was kept at 40 °C under stirring for 4 h. Finally, the product was collected by centrifuge and washed with deionized water several times and dried in a vacuum environment.

4.2.4 Synthesis of SnO₂/graphene shells

The above prepared PS@SnO₂/graphene oxide multi-layered spheres were calcinated at 400 °C in air for 2 h to obtain SnO₂/graphene shells.

4.2.5 Structural characterization

The morphology and structure of samples were investigated by field emission scanning electron microscopy (FESEM) (JEOL, JSM-7001F), transmission electron microscopy (TEM) (JEOL, JEM-2100). X-ray diffraction (XRD) pattern was collected on a Rigaku RINT 2500. Raman spectra was recorded with a RAMAN-11 (Nanophoton) with 532 nm laser source. Thermogravimetric analysis (TGA) was tested on an SDTA851e Analyzer at a heating rate of 10 °C min⁻¹ in air. X-ray photoelectron spectroscopy (XPS) data were obtained by an PHI Quantera SXM (Ultravac-PHI). The

BET surface area was probed by using an AUTOSORB iQ-MP instrument.

4.2.6 Electrochemical characterization

CR2032 coin-type cells were used to test the electrochemical performance of the samples. SnO₂/graphene composite were filtered on a PTFE membrane and cut into circular disks with diameter of 15 mm. After drying in a vacuum oven at 80°C for 12 h, the small disks were directly used as the working electrodes. A piece of Cu foil current collector was placed on the sample side of the disks. In a glove box, the test cells were assembled with Li foil as counter electrode, PP membrane (Celgard 2400) as the separator, and 1 M LiPF₆ in a mixture of ethylene (EC), diethyl carbonate (DEC) (1:1, v/v) as the electrolyte. Cyclic voltammograms and galvanostatic charge-discharge were performed on a VMP3 electrochemical station (Biologic) between 0.005 V to 2.5 V.

4.3 Result and Discussion

Fig 4-1 shows the designed route for preparing the composite of interconnected graphene hollow spheres confined SnO₂ nanoparticles. Aqueous solution of SnCl₂•2H₂O was firstly mixed with graphene oxide (GO) suspension, and SnCl₂•2H₂O would be hydrolyzed to SnO₂ nanoparticles on both side of the graphene oxide nanosheets. After adding of polystyrene (PS) sphere template, the composite sheets would wrap around the PS spheres. The final composite of interconnected graphene hollow spheres confined SnO₂ nanoparticles was obtained after burning out of the PS spheres and reduction of GO by a calcination process in air atmosphere.

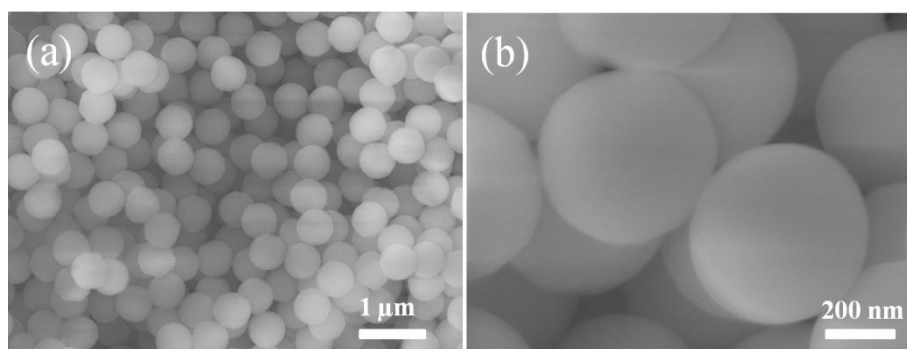


Fig. 4-2 SEM images of PS spheres.

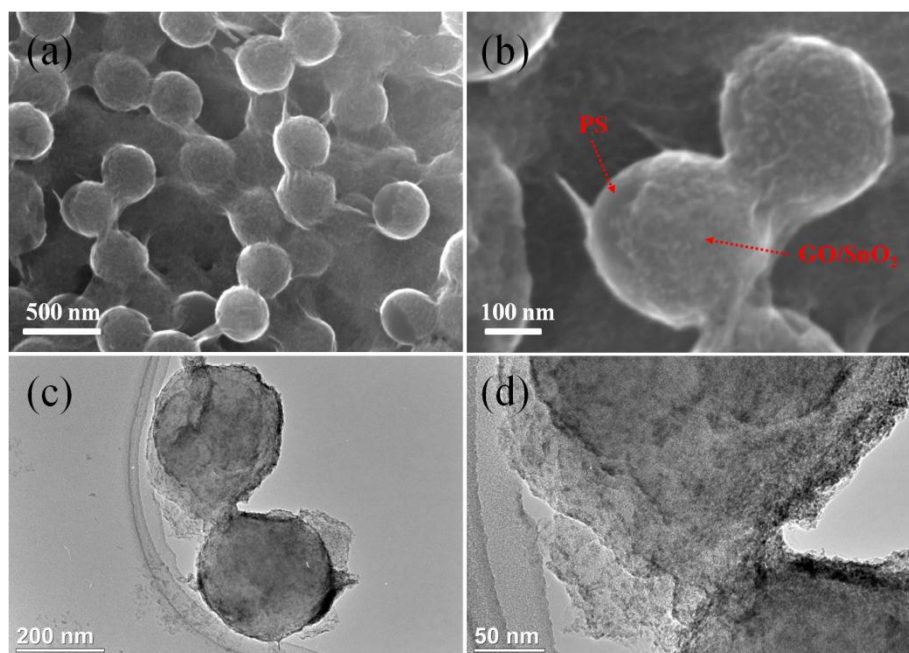


Fig. 4-3 SEM and TEM images of PS@GO/SnO₂ composite.

Fig 4-2 shows the SEM images of as prepared PS templates. The PS templates show a typical sphere structure with rather smooth surface and a diameter of 300 nm. Besides, the spheres are monodispersed, which is crucial for the uniform coating of GO/SnO₂ composite sheets in the following step. Fig 6-3a and b display the SEM images of the PS@GO/SnO₂ composite. As can be observed, the surface of the PS spheres is no longer smooth but coated with a composite sheet. In addition, the monodispersed PS spheres are linked together by the composite sheet. TEM images also confirm this core-shell structure. The ultra-fine SnO₂ nanoparticles are uniformly anchored on the graphene oxide sheets and the composite sheets wrap around on the PS spheres.

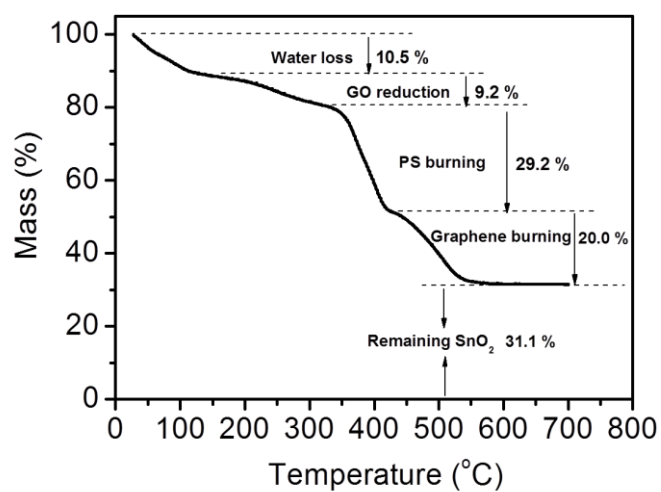


Fig. 4-4 TGA curve of PS@SnO₂/graphene composite.

In order to find the suitable heating temperature, TGA was performed with the PS@SnO₂@graphene composite and its weight loss curve was shown in Fig 4-4. As can be seen, the TGA curve shows a multi-step weight loss process. From the beginning to 100 °C is the weight loss of absorbed water. The weight loss From 200 to 300°C should be ascribed to the reduction of GO. From 300 to 380 °C is the burning of PS. From 420 to 550°C is the burning of graphene. So, in order to get the graphene/SnO₂ composite, the heating temperature was determined at 400°C, where PS can be burned out and graphene and SnO₂ was retained. Besides, the weight ratio of graphene and SnO₂ (2:3) in the final composite can also be identified from the TGA curve.

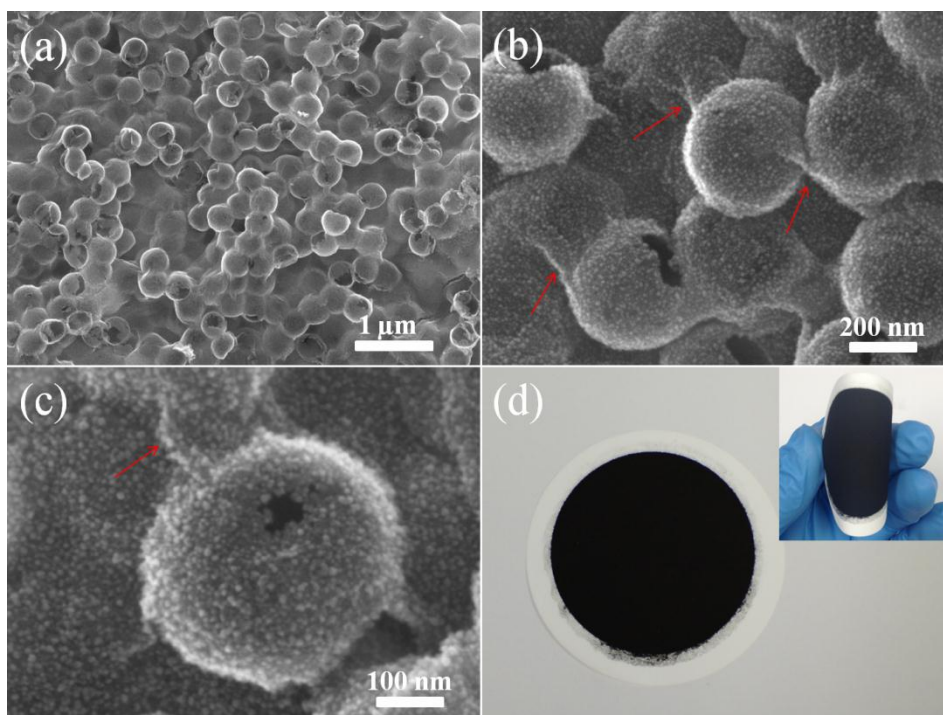


Fig. 4-5 (a-c) FESEM images of SnO₂/graphene composite at different magnifications ; (d) A photograph of the paper of SnO₂/graphene composite filtered on a PTFE membrane showing it can be self-assembled without any binder. The inset showing its mechanical flexibility.

The morphology of as prepared graphene/SnO₂ composite was firstly examined by SEM and the representative SEM images in different magnification are shown in Fig 4-5a-c. From the SEM images, we can see the typical sphere like morphology of the composite can be retained after burning out of PS spheres, indicating its good mechanical property. Also, the self-interconnected feature of the composite spheres is clearly revealed in the Fig 4-5b and c. Due to this self-interconnected feature, the composite spheres can be self-assembled without any binder by vacuum filtration on a PTFE paper, as shown in Fig 4-5d. The filtered composite paper can be directly used as anode for lithium-ion battery eliminating the need of any binders that could lower the conductivity and increase weight of the whole electrode, thus resulting in better lithium storage property.

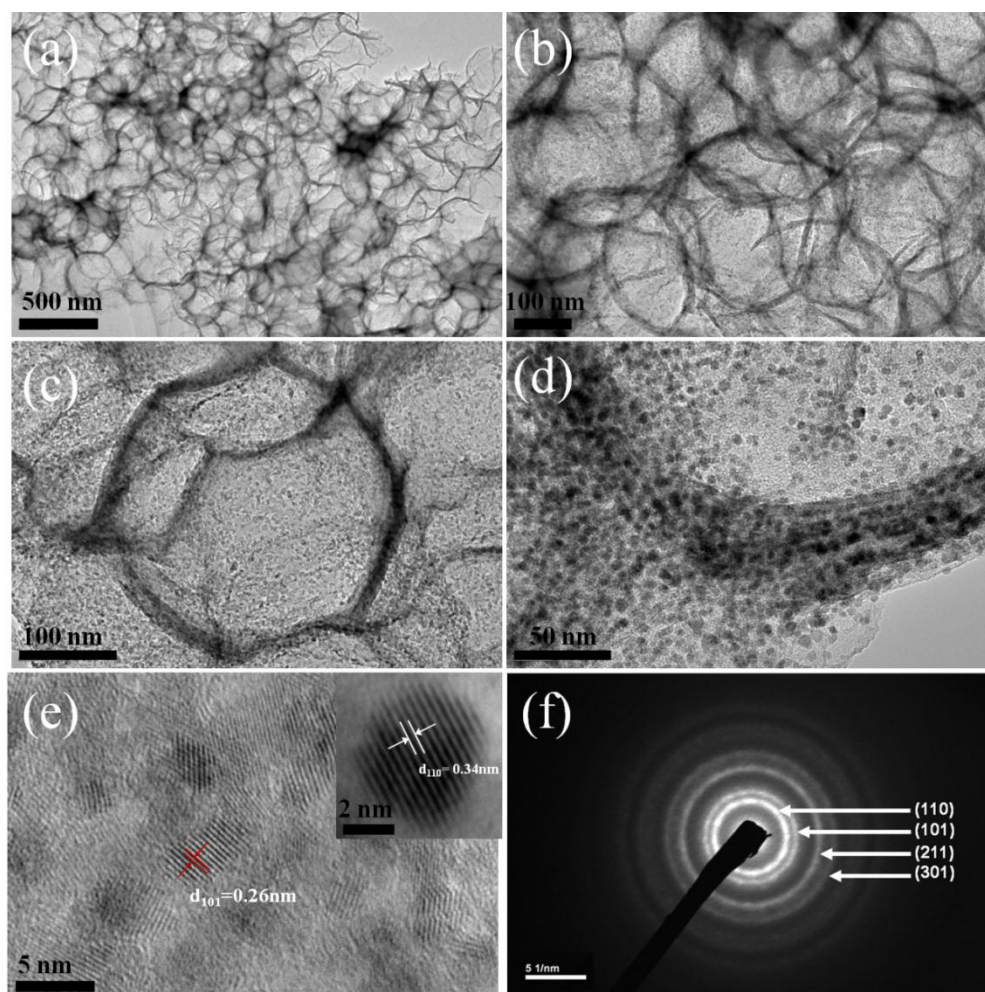


Fig. 4-6 (a-d) TEM images of SnO₂/graphene composite at different magnifications; (e) HRTEM images; (f) the selected area electron diffraction (SEAD) pattern of SnO₂/graphene composite.

The morphology and structure of the graphene/SnO₂ composite spheres were further characterized using TEM. Fig 4-6a-d shows the typical TEM images of the graphene/SnO₂ composite spheres. The SnO₂ nanoparticles are uniformly composited with the graphene sheets. The spheres are interconnected with a diameter about 300 nm, which is agreed with the SEM results. From the larger TEM image in Fig 4-6d, we can clearly see that SnO₂ nanoparticles are confined between the multi-layered graphene sheets and the size of the SnO₂ nanoparticles is about 5 nm. The HR-TEM images in Fig 4-6e and the SEAD pattern Fig 6-6f confirm the nanoparticles are SnO₂. [11-13,15]

XRD, Raman and TGA techniques were further employed to characterize the chemical structure of the graphene/SnO₂ composite spheres. Fig 4-7a shows the XRD pattern of as prepared composite spheres. It can be well indexed to the tetragonal phase of SnO₂ (JCPDS:41-1445), which confirms again the existence of SnO₂ in the composite. [16,25-27] It should be noted that the main peak of graphene (002) is overlapped with the (110) peak of SnO₂, so it is difficult to distinguish the independent diffraction peak of graphene in the XRD pattern. The Raman spectrum shown in Fig 4-7b displays the characteristic D band and G band, confirming the formation of graphene during the heating process. Fig 4-7c shows the TGA curve of as prepared composite spheres which was

performed under air atmosphere. The decomposition temperature range from 400 to 550 °C, corresponding to the burning out of graphene in air. The remained 61.8% weight should only come from SnO₂, and this ratio is consistent with the former TGA results of PS@SnO₂/graphene composite shown in Fig 4-4.

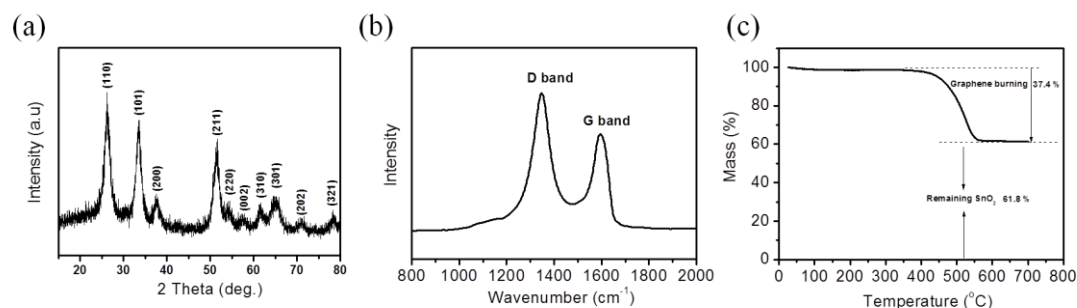


Fig. 4-7 (a) XRD pattern; (b) Raman spectra ; (c) TGA curve of SnO₂/graphene composite.

XPS was also performed to further characterize the composite spheres. Figure 4-8a shows the XPS survey spectra of the composite spheres. There are only Sn, O, C elements in the composite, no other element was detected. The Sn 3d regions with two peaks centered at 495.5 and 487.1 eV can be observed in Fig 4-8b, and they are attributed to Sn 3d 3/2 and Sn 3d 5/2, suggesting the (IV) state of tin in the form of SnO₂. [16,17] Figure 4-8c and d show the high-resolution spectra of the C1s spectra of graphene/SnO₂ composite and GO, respectively. In the C1s spectra of graphene/SnO₂ composite and GO, four peaks located at 284.6, 286.7, 287.8, and 289.1 eV can be seen, which are assigned to C–C (sp²), C–O, C=O and O–C=O groups, respectively. As can be observed, the intensity of oxygenated functionalities in the graphene/SnO₂ composite are much weaker than that of GO, indicating the graphene oxide in the composite had been reduced to graphene. [16,17]

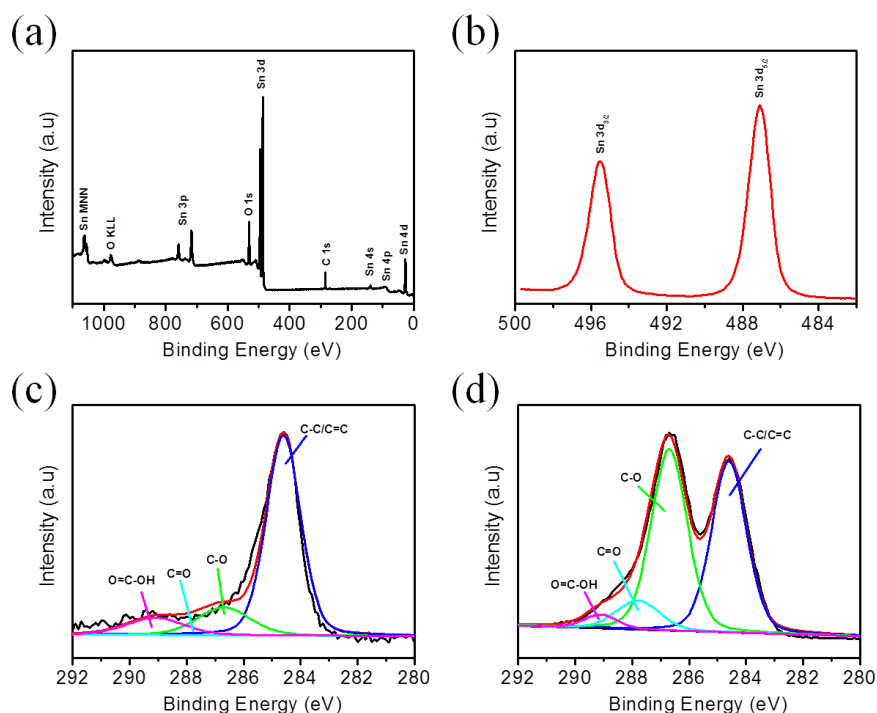


Fig. 4-8 (a) XPS survey and (b) Sn 3d XPS spectra of SnO₂/graphene composite, (c) C 1s XPS spectra of SnO₂/graphene composite, (d) C 1s XPS spectra of GO.

As we all know, the specific surface area and the pore size distribution of the electrode materials play a key role in the final electrochemical performances. The porosity of the as prepared graphene/SnO₂ composite spheres was investigated using Brunauer-Emmett-Teller (BET) nitrogen adsorption method performed at 77K and the BET isotherm is shown in Figure 6-9. As can be seen in Figure 4-9, the curve is the typical type IV isotherm, indicating a large number of mesopores in the composite. According to the adsorption isotherm, the specific surface area of the composite spheres is 315 m²/g, which is larger than previously reported bare SnO₂ and some other kinds of graphene/SnO₂ composites. The pore size distribution curve (shown in the inset) derived from the adsorption isotherm also confirm its large mesopores proportion. As can be observed, the pores are mainly centered in the range of 3-5 nm, which is favorable for the diffusion of the Li ions and the electron transfer within the electrode.

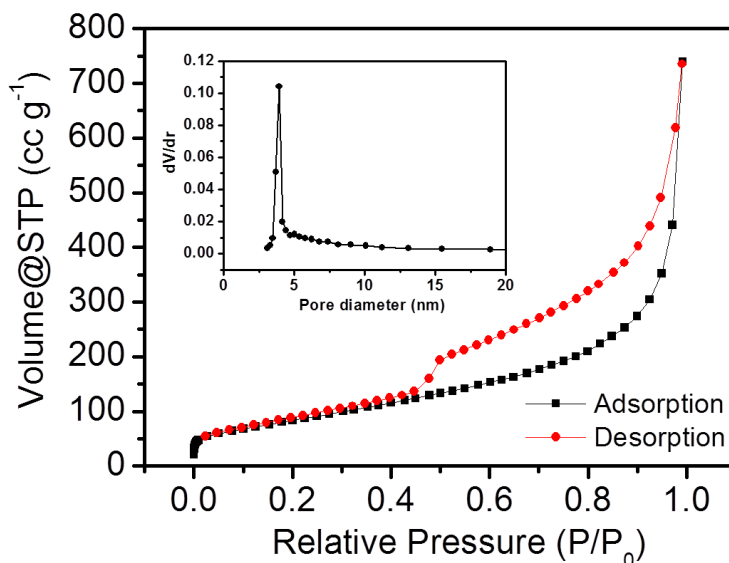
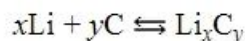
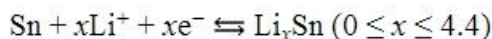
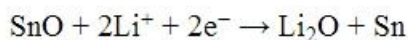
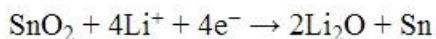


Fig. 4-9 Nitrogen adsorption-desorption isotherms obtained at 77 K. The inset is the corresponding pore size distribution.

The composite spheres are used as anode materials for lithium ion batteries and the obtained electrochemical performances are shown in Figure 4-10. Figure 6-10a shows the first three CV curves at the scan rate of 0.1mV/s in the potential range of 0.005 to 2.5V. In the first cycle, the reduction peak at 0.7V corresponds to the formation of a solid electrolyte interface (SEI) layer and the reduction SnO₂ to Sn as shown in eqn (2). [12-14] This peak disappears after the first cycle, indicating the SEI layer is stable. There is a sharp reduction peak at 0.1 V, which can be assigned to the formation of Li-Sn alloys and the reaction between lithium and graphene sheets, as described in eqn (3) and (4). In the anodic curve, two main peak located at 0.51 and 1.25V are attributed to the de-alloying of Li-Sn alloy and the partially reversible reaction of Sn to SnO₂. [12-14]The reversibility of this peak suggest the advantages of this unique structured graphene/SnO₂ composite, such as high electric conductivity, good contact between SnO₂ and graphene sheets.



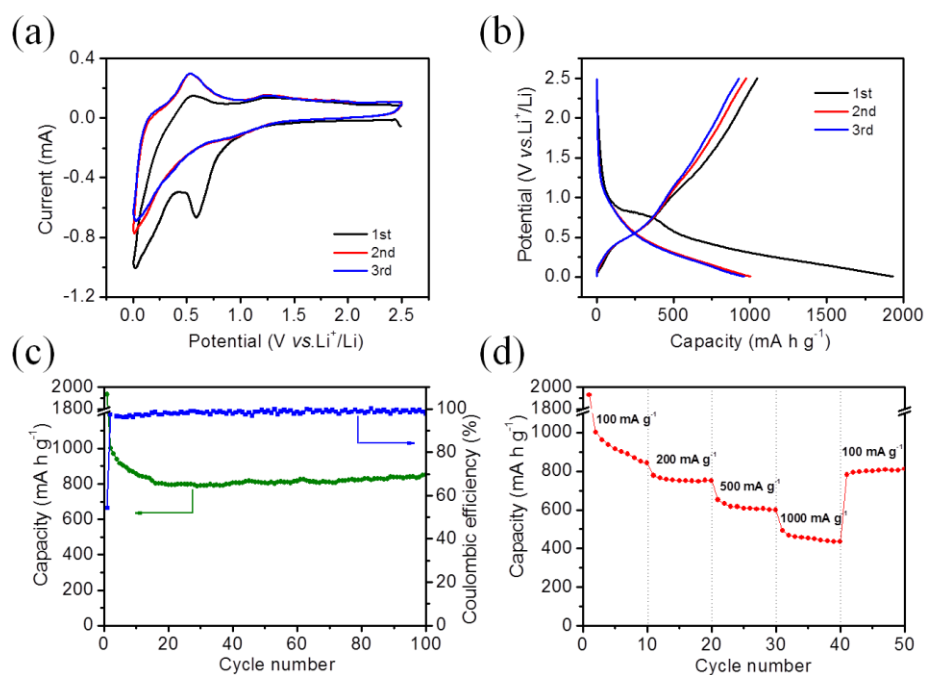


Fig. 4-10 Electrochemical performance of the SnO₂/graphene composite. (a) CV curves of the first three cycles at a scan rate of 0.1 mV s⁻¹, (b) charge/discharge curves, (c) rate capability; (d) cycling stability and coulombic efficiency at 100 mA g⁻¹.

Figure 4-10b shows the initial three charge-discharge curves of the composite spheres at a current density of 100 mA/g. In the first discharge curve, the potential plateau at about 0.78 V is associated to the reduction of SnO₂ to Sn. The long flat curve from 0.5 to 0.005 V is the reaction of Sn with Li. The first discharge capacity is 1980 mAh/g, which is much larger than the first charge capacity of 1032 mAh/g due to the irreversible formation of Li₂O, which is in good agreement with the former CV measurement. The reversible capacity in the second discharge process is 1003 mAh/g, which is among the highest values for SnO₂ based anodes. Figure 6-10c displays the cycling performance of the composite spheres. After 100 repeated charge and discharge cycles at a current density of 100 mA/g, 88% of the initial capacity can be retained and the coulombic efficiency remain nearly 100%, indicating the high cycling stability of the graphene/SnO₂ composite spheres. A multiple-step galvanostatic strategy was adopted to test the rate performance of the composite spheres. As shown in Figure 10d, the reversible discharge capacity is 1003, 778, and 652 mAh/g at current densities of 100, 200, 500 mA/g, respectively. Even at the high current density of 1000 mA/g, the composite spheres can still exhibit a high specific capacity of 492 mAh/g, which is much larger than the theoretical capacity of graphite (372 mAh/g). Besides, when the current density goes back to 100 mA/g, a high specific capacity of 781 mAh/g can be recovered.

4.4 Conclusion

In summary, we have reported a unique graphene/SnO₂ composite, where the SnO₂

nanoparticles are confined between the multi-layered sheets of interconnected graphene hollow spheres. The as prepared interconnected composite spheres can self-assemble together to form a free standing paper without of any binder, and it can be directly used as anode for Li-ion battery. Electrochemical measurements demonstrate that the composite spheres exhibit high specific capacity, good rate capability and excellent long cycling performance, indicating its great potential for high performance Li-ion batteries.

References

1. A. L. Mohana Reddy, S. R. Gowda, M. M. Shaijumon and P. M. Ajayan, *Advanced materials*, 2012, **24**, 5045-5064.
2. Z.-S. Wu, G. Zhou, L.-C. Yin, W. Ren, F. Li and H.-M. Cheng, *Nano Energy*, 2012, **1**, 107-131.
3. B. Luo, S. Liu and L. Zhi, *Small*, 2012, **8**, 630-646.
4. X. Yu, S. Liu and J. Yu, *Applied Catalysis B: Environmental*, 2011, **104**, 12-20.
5. L.-Y. Hao, C.-L. Zhu, W.-Q. Jiang, C.-N. Chen, Y. Hu and Z.-Y. Chen, *Journal of Materials Chemistry*, 2004, **14**, 2929.
6. H. Wang, Y. Liang, M. Gong, Y. Li, W. Chang, T. Mefford, J. Zhou, J. Wang, T. Regier, F. Wei and H. Dai, *Nature communications*, 2012, **3**, 917.
7. H. Zhang, X. Yu and P. V. Braun, *Nature nanotechnology*, 2011, **6**, 277-281.
8. S. Yang, W. Yue, J. Zhu, Y. Ren and X. Yang, *Advanced Functional Materials*, 2013, **23**, 3570-3576.
9. X. Wang, X. Zhou, K. Yao, J. Zhang and Z. Liu, *Carbon*, 2011, **49**, 133-139.
10. J. S. Chen and X. W. Lou, *Small*, 2013, **9**, 1877-1893.
11. B. Zhang, Q. B. Zheng, Z. D. Huang, S. W. Oh and J. K. Kim, *Carbon*, 2011, **49**, 4524-4534.
12. S. Ding, D. Luan, F. Y. Boey, J. S. Chen and X. W. Lou, *Chemical communications*, 2011, **47**, 7155-7157.
13. X. Huang, X. Zhou, L. Zhou, K. Qian, Y. Wang, Z. Liu and C. Yu, *Chemphyschem : a European journal of chemical physics and physical chemistry*, 2011, **12**, 278-281.
14. J. Yao, X. Shen, B. Wang, H. Liu and G. Wang, *Electrochemistry Communications*, 2009, **11**, 1849-1852.
15. P. Lian, X. Zhu, S. Liang, Z. Li, W. Yang and H. Wang, *Electrochimica Acta*, 2011, **56**, 4532-4539.
16. Y. Chen, B. Song, R. M. Chen, L. Lu and J. Xue, *Journal of Materials Chemistry A*, 2014, **2**, 5688.
17. B. P. Vinayan and S. Ramaprabhu, *Journal of Materials Chemistry A*, 2013, **1**, 3865.
18. Y. Zou, X. Zhou, J. Xie, Q. Liao, B. Huang and J. Yang, *Journal of Materials Chemistry A*, 2014, **2**, 4524.
19. H. Zhang, P. Xu, Y. Ni, H. Geng, G. Zheng, B. Dong and Z. Jiao, *Journal of Materials Research*, 2014, **29**, 617-624.
20. Z. Du, X. Yin, M. Zhang, Q. Hao, Y. Wang and T. Wang, *Materials Letters*, 2010, **64**, 2076-2079.
21. H. Kim, S.-W. Kim, Y.-U. Park, H. Gwon, D.-H. Seo, Y. Kim and K. Kang, *Nano Research*, 2010, **3**, 813-821.
22. Z. Wang, H. Zhang, N. Li, Z. Shi, Z. Gu and G. Cao, *Nano Research*, 2010, **3**, 748-756.
23. G. Zhou, D. W. Wang, L. Li, N. Li, F. Li and H. M. Cheng, *Nanoscale*, 2013, **5**, 1576-1582.

24. Q. Shao, J. Tang, Y. Lin, F. Zhang, J. Yuan, H. Zhang, N. Shinya and L.-C. Qin, *Journal of Materials Chemistry A*, 2013, **1**, 15423.
25. H. Song, L. Zhang, C. He, Y. Qu, Y. Tian and Y. Lv, *Journal of Materials Chemistry*, 2011, **21**, 5972.
26. G. Wang, B. Wang, X. Wang, J. Park, S. Dou, H. Ahn and K. Kim, *Journal of Materials Chemistry*, 2009, **19**, 8378.
27. M. Zhang, D. Lei, Z. Du, X. Yin, L. Chen, Q. Li, Y. Wang and T. Wang, *Journal of Materials Chemistry*, 2011, **21**, 1673.

Chapter 5

Carbon nanotube Spaced Graphene Aerogels with Enhanced Capacitances in Aqueous and Ionic liquid Electrolytes

5.1 Introduction

Electric double-layer capacitors (EDLC), also often known as supercapacitors, have attracted great attention in recent years due to their high power density and long cycle lifetime.[1-3] Among the various materials for supercapacitors, graphene has appeared to be a promising candidate because of its large specific surface area, high electrical conductivity, and outstanding mechanical properties.[4-6] However, the graphene sheets tend to restack due to the π - π interactions and the van der Waals forces between them, which make it often difficult for ions to gain access to the inner layers of stacked graphene to form electric double-layers with the electrolyte, thus usually leading to an actual specific capacitance far below its theoretical value of 550 F g^{-1} calculated for graphene.[7] To address this problem, many efforts have been devoted to synthesis of graphene materials with a desired structure to reduce the restacking of graphene, such as having curved graphene sheets, folded graphene paper, nano-porous graphene foam, vertically aligned graphene sheets, and our recently reported graphene hollow spheres.[8-12]

Recently, Graphene aerogel (GA), a three-dimensional (3D) macroscopic architecture of graphene, has been found to exhibit great potential in the fields of oil adsorption and catalysis. Based on their several features such as large specific surface area, high porosity, and high electrical conductivity, GAs have also been employed as electrode materials for supercapacitors. Lee et al. has reported a ball-shaped graphene aerogel using a chemical vapor deposition (CVD) method, which showed a specific capacitance of 206 F g^{-1} . [13] Despite of its high purity and superior electrical conductivity of CVD produced graphene aerogel, the low yield and required high temperature condition mainly obstruct its practical application. Xu et al. has developed a hydrothermal method, as shown in Fig.4-1A, to produce graphene hydrogels. The as prepared graphene hydrogels is electrical conductive, mechanical strong, and thermally stable and exhibits a specific capacitance of 160 F g^{-1} . [14] Then, by freeze drying the hydrothermal produced graphene based hydrogels, various

graphene aerogels including N-doped graphene aerogels, N and B co-doped graphene aerogels, graphene/porous carbon aerogels, and graphene/polypyrrole aerogels are prepared as electrode materials for supercapacitors. [14-16] There is a precious advantage for these graphene based aerogels for supercapacitors that these graphene based aerogels usually possess vast large pores (>100 nm), which would allow the outmost graphene sheets to be quickly wetted by the electrolytes, therefore, the assembled supercapacitors could be charged and discharged very quickly. However, there also exists a main drawback. Graphene sheets in these graphene based aerogels usually stacked in a thick slab between macropores, leaving behind the inner layers inaccessible to the electrolyte ions, which makes the current graphene aerogel based electrodes suffer from a low specific capacitance.

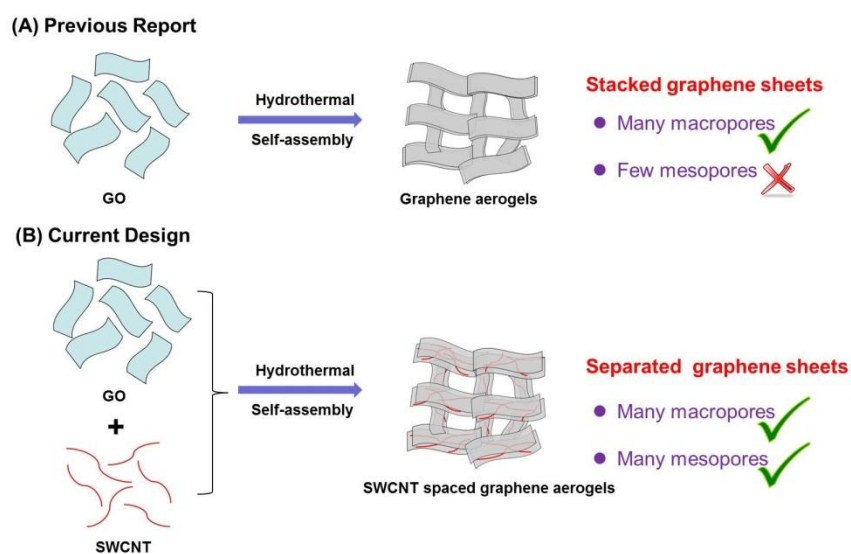


Figure 5-1. Schematic comparison of previously reported graphene aerogels and current designed SWCNT spaced graphene aerogels.

To prevent the restacking of graphene, our group has firstly reported that single-walled carbon nanotubes (SWCNTs) were an effective spacer to inhibit the restacking of chemical reduced graphene.[19,20] Then, carbon black, small graphite particles, and diethylene glycol have also been studied recently as spacers.[21-23] Zhu et al. has reported carbon nanotubes were also good spacers for CVD grown graphene and the supercapacitor show a high energy density of 60 Wh kg^{-1} in ionic liquid electrolyte.[24] More recently, we have reported a hydrothermal reduced graphene-carbon nanotube composite for selective detection of uric acid in which the carbon nanotubes play a key role in increasing more active sites for oxidation of uric acid.[25] These above reports enable us to use carbon nanotube spacer to prevent the restacking in graphene aerogels(as shown in Fig.5-1B), which would result in a macro-porous aerogel structure with separated graphene walls, and thus provide both macropores to ensure electrodes fast wetted by the electrolyte ions and additional mesopores created by the carbon nanotube spacers for more ions adsorption.

Herewith, we present a comprehensive study of the supercapacitor application of the single-walled carbon nanotube spaced graphene aerogel (SSGA) materials, and highlight the role of

the SWCNTs spacer in realizing a high specific capacitance together with a high rate capability by increasing the specific surface area, bringing about favorable pore size distribution, and resulting in faster ions transport. Compared with previously reported graphene aerogel electrodes for supercapacitor application, the combined effect of the macro-porous structure and the SWCNTs spacer in this composite aerogel are : (i) The 3D macro-porous structure provides numerous large pores to make the electrode be wetted quickly by the electrolyte to ensure high rate performance; (ii) The SWCNTs are placed between the graphene layers to prevent the restacking of graphene sheets and more accessible surface area is made available for ion adsorption; (iii) The introduction of highly conductive SWCNTs can also reduce the resistance of the SSGA electrode to further increase the rate capability and promote stable cycling performance.

Electrochemical tests showed that the SSGA-12 sample (weight ratio of graphene oxide to SWCNT is 12:1 in the initial composite) delivered a highest specific capacitance of 245.5 F g^{-1} at a current density of 2.5 A g^{-1} in aqueous electrolyte, which is 37% higher than that of pristine graphene aerogel (GA). Besides, this value is also much higher than that of previously reported 3D macroscopic graphene hydrogels (160 F g^{-1} , 166 F g^{-1} , 186 F g^{-1} , 190.1 F g^{-1}), [14,26-28] graphene aerogels (128 F g^{-1} , 239 F g^{-1}), [16,29] folded graphene paper (172 F g^{-1}), [8] or graphene foams (110 F g^{-1}). [9] Using this structure the rate capability has also been improved significantly. A high specific capacitance of 197.0 F g^{-1} is achieved even at a high current density of 80 A g^{-1} , corresponding to 80% of that at 2.5 A g^{-1} . After 2000 cycles of repeated charging and discharging at a current density of 10 A g^{-1} , 97% of its initial capacitance is retained, highlighting its excellent stability. When using the ionic liquid (EMIMBF₄) electrolyte, the SSGA-12 electrode exhibited a capacitance of 183.3 F g^{-1} at 0.5 A g^{-1} and a high energy density of 80 Wh kg^{-1} , which is about an order of magnitude larger than the previously reported 3D macroscopic graphene electrodes in aqueous electrolyte.

5.2 Experimental

5.2.1 Sample preparation

Graphene oxide (GO) was obtained first from natural graphite flakes by a modified Hummer's method. [30] The SWCNT/graphene composite aerogel was synthesized by hydrothermal reduction of a mixture of the graphite oxide and single-walled carbon nanotubes, followed by freeze drying. In our experiment the graphene oxide dispersion was mixed with carbon nanotubes with different weight ratios of GO to SWCNTs (16:1, 12:1 and 8:1). The mixture was then sonicated for 30 minutes before it was transferred to a Teflon lined autoclave and held in an oven at $180 \text{ }^\circ\text{C}$ for 12 hours. After being cooled to room temperature, the obtained composite hydrogel was freeze dried to obtain an aerogel. The products were denoted as SSGA-16, SSGA-12, SSGA-8 according to the weight ratio of GO to SWCNTs in the starting mixture. For comparison pristine graphene aerogel (GA) was also prepared through a similar procedure without adding carbon nanotubes.

5.2.2 Structural characterization

The morphology and microstructure of the as-prepared material was examined with both scanning electron microscopy (SEM, JEOL 6500F) and transmission electron microscopy (TEM, JEOL 2100). The nitrogen adsorption/desorption isotherms at 77 K were collected on an AUTOSORB iQ-MP instrument at 77 K. The specific surface area was determined according to the Brunauer-Emmett-Teller (BET) method in the relative pressure range of 0.05-0.3. The pore size distribution was analyzed using an NL-DFT method from the nitrogen adsorption data. X-ray diffraction (XRD) patterns were recorded with a Rigaku RINT 2500 diffractometer. Fourier transform infrared spectroscopy (FT-IR) data were acquired on a Nicolet 6700 spectrometer and Raman spectra were obtained using RAMAN-11 (Nanophoton) with a 532 nm laser.

5.2.3 Electrochemical characterization

The graphene aerogels were used as the active materials for the electrodes of symmetrical supercapacitors for electrochemical characterization. To assemble a test cell, the as-prepared aerogels were cut into small slices with a thickness of about 1 mm for electrode preparation of electrodes. For tests in aqueous electrolyte, 5 M KOH was used as the electrolyte, a piece of PTFE filter paper was used as the separator, and two Pt foils were used as the current collectors. For tests in ionic liquid electrolyte, 1-Ethyl-3-methylimidazolium tetrafluoroborate (EMIMBF₄) was used as the electrolyte, a piece of glass fiber was used as the separator, and conductive carbon coated aluminum foils (Exopack™ 0.5 mil 2-side coating) were used as the current collectors. The cells were assembled in an argon filled glove box.

Cyclic voltammetry (CV), galvanostatic charge-discharge (GC), and electrical impedance spectroscopy (EIS) measurements were performed using a VMP3 multi-potentiostat/galvanostat (Biologic) system. The specific capacitance C was calculated by $C = 2I\Delta t/(m\Delta V)$, where I is the discharge current, Δt is the discharge time, ΔV is the voltage change excluding the IR drop during the discharge process, and m is the mass of a single electrode. The specific energy density E and the specific power density P were calculated using $E = CV^2/8$ and $P = E/t$, respectively, where C is the specific capacitance, V is the voltage of the charged supercapacitor, and t is the discharge time.

5.3 Results and discussion

5.3.1 Preparation and morphology

Fig. 5-2 illustrates the synthesis of single-walled carbon nanotube spaced graphene aerogel (SSGA). As illustrated in Fig. 4-1(a), the SWCNTs were first dispersed in a solution of GO. Considering that the aqueous solution of GO was a good solvent for dispersing SWCNTs and the single layer nature of GO sheets,[31,32] the mixture of SWCNTs and single layers of GO is

homogeneous as seen in Fig. 5-2(a). During the process of hydrothermal reduction, due to the increasing hydrophobicity of the reduced GO caused by losing the oxygenous groups, the hydrothermally reduced GO sheets would self-assemble into a 3D macro-porous structure with carbon nanotubes between them, forming a SWCNT/graphene composite hydrogel. Finally, the composite hydrogel was freeze dried to obtain a composite aerogel. It was noticed that the composite aerogel is ultralight in weight. As shown in Fig. 5-2(d), a block of the composite aerogel could be balanced on a dandelion, indicating its ultralight weight due to its porous structure which will be discussed later.

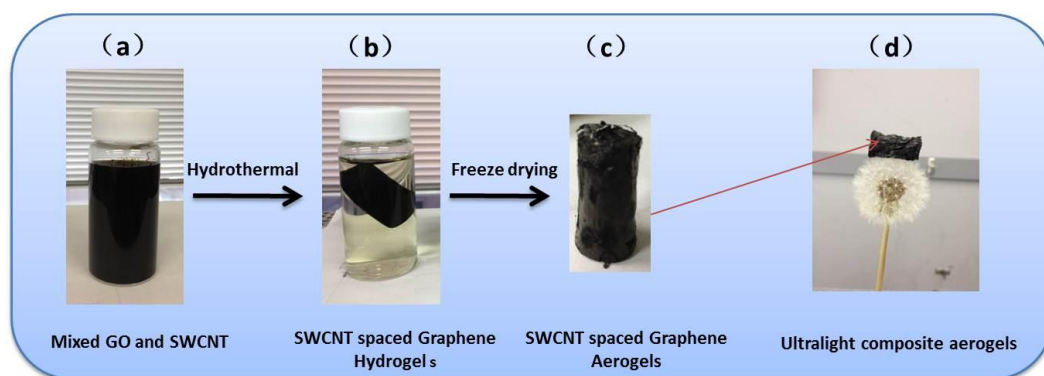


Figure 5-2 (a) Schematic photographs of the fabrication of homogeneous SSGAs with macro-pores and integrated 3D structure. The resulting SSGA is ultra-light in weight.

The unique structure of the SSGAs was characterized by SEM and TEM as shown in Fig. 5-3. As can be seen in the SEM images given in Fig. 5-3(a) and 5-3(b), the graphene aerogels have a 3D macro-porous structure with macropores (5-10 μm) and graphene walls. In addition, the TEM image shown in Fig. 5-3(c) reveals that the carbon nanotubes were randomly mixed with graphene sheets, indicating that the carbon nanotubes and graphene sheets are well mixed. Further evidence is shown in the high-resolution TEM image given in Fig. 5-3(d) which shows a single carbon nanotube sticking out of a graphene sheet, illustrating that the SWCNTs are in between the graphene layers, forming a sandwich structure. Combining the SEM and TEM images, we suggest that the SSGAs possess multi-level of pores and the graphene sheets within the structure are well spaced by carbon nanotubes. These features will not only guarantee that the SSGA electrode can be wetted quickly by the electrolyte but also release more accessible surface area for electrolyte ion adsorption in the supercapacitor device.

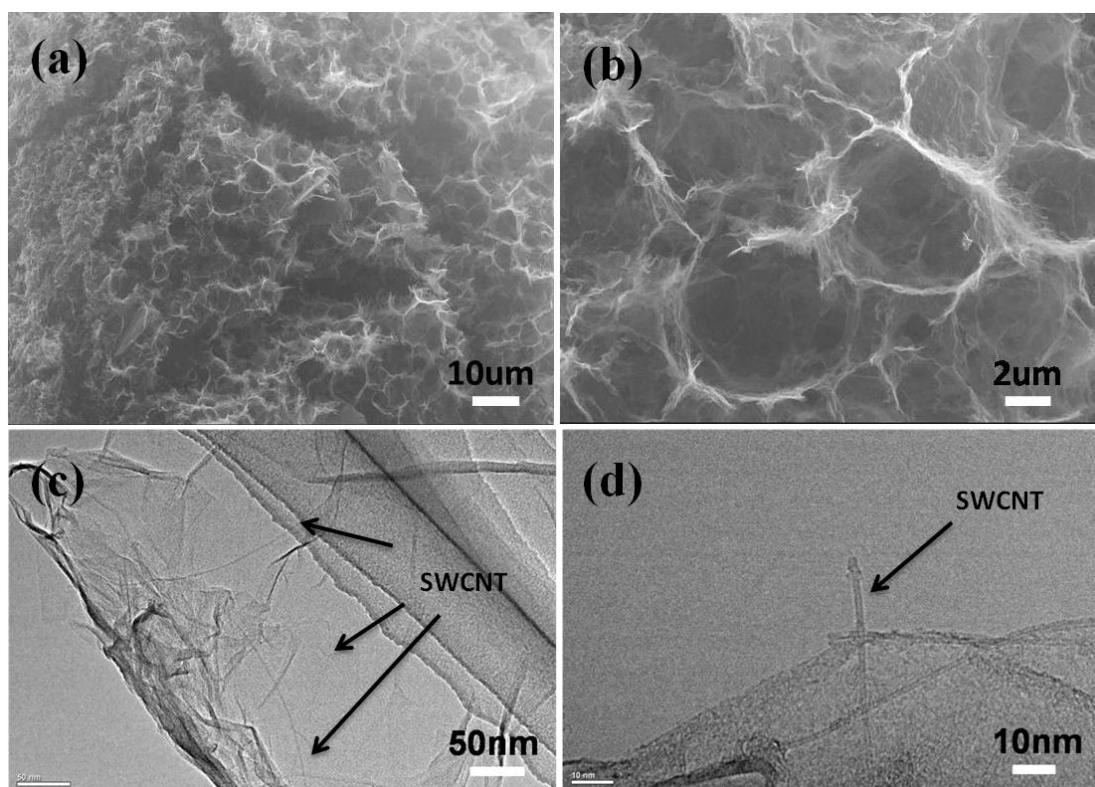


Figure 5-3 (a-b) SEM images; and (c-d) TEM images of as-prepared SSGAs. Carbon nanotubes are distributed in graphene structure homogenously.

5.3.2 Structural study

The structure of GA and SSGAs were further investigated by XRD, FT-IR spectroscopy, and Raman spectroscopy. Fig. 5-4(a) displays the XRD patterns of GO, GA, and SSGA. The characteristic inter-layer spacing of the GO layers as indicated by the sharp reflection peak at $2\theta = 11.4^\circ$ is $d = 0.776$ nm, which is much larger than that of graphite (~ 0.340 nm) due to the introduction of oxygenous functional groups. After the hydrothermal reduction this characteristic peak vanished and a new and broad peak centered at about $2\theta = 23.7^\circ$ (corresponding to $d = 0.375$ nm) was observed in both GA and SSGA, reflecting the deoxygenization and partial recovery of the graphitic structure. It should also be noted that the weaker and broader peak of SSGA (in comparison with that of GA) indicates that a lower degree of restacking of graphene in SSGA, which is attributed to the SWCNT spacers. In the FT-IR spectra (Fig. 5-4(b)) the C=O in GO at 1730 cm^{-1} disappeared in GA and SSGA, confirming the reduction of GO. Fig. 5-4(c) shows the Raman spectra of GA, SSGA, and SWCNTs. The intensity ratio of the D band at 1335 cm^{-1} to the G band at 1578 cm^{-1} of SSGAs decreased gradually from 1.00 to 0.72 with the increasing concentration of SWCNTs in the composite, indicating successive increment of perfect graphitic structures due to SWCNTs.

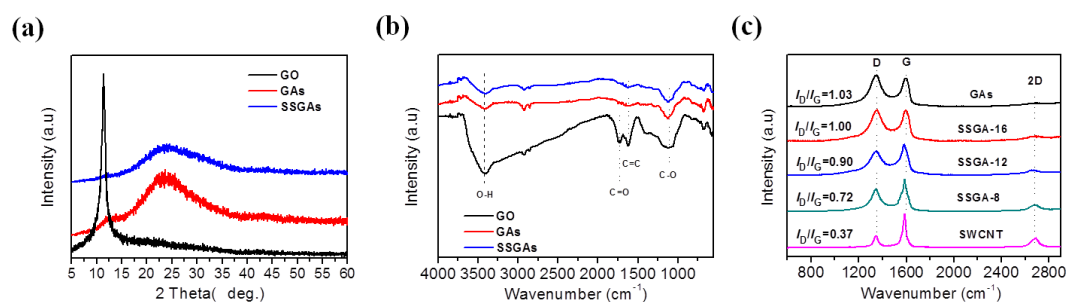


Figure 5-4 (a) XRD patterns of GO, GAs, and SSGAs; (b) FT-IR spectra of GO, GAs, and SSGAs; and (c) Raman spectra of SWCNT, GAs, and SSGAs with various concentration of SWCNTs.

It is well known that the supercapacitor performance is highly sensitive to the specific surface area (SSA) and the pore size distribution of the carbon electrode. Previous reports have shown that a large SSA together with a suitable pore size distribution containing a large proportion of accessible mesopores is ideal for electrolyte ion adsorption.[33] The porosity of the as-prepared GA and SSGA was studied by nitrogen adsorption/desorption isotherms. As shown in Fig. 5-5(a), the isotherm of GA displays a steep uptake at the relative pressure of 0.9-1.0, attributed to the large number of textural macropores. As for the SSGA, the curves are the type IV isotherms, indicating a large proportion of mesopores. The difference in the pore size distribution between GA and SSGA is further revealed in the plot of cumulative pore volume versus pore diameter shown in Fig. 5-5(b). Pores smaller than 8 nm accounted for only 59 % of the total volume in GA, while near 90% of the total pore volume is contributed by pores smaller than 8 nm in SSGA, indicating a large number of small mesopores have been created by the insertion of SWCNTs spacer. The calculated SSAs of the four samples are given in Table 4-1. All the three SSGA samples possess larger SSA than GA and the SSGA-12 sample showed a largest SSA of 807 m² g⁻¹, which is even comparable to activated graphene aerogel or holey graphene.[34,35] Therefore, the incorporation of SWCNTs has not only changed the pore size distribution but also increased the SSA, which is helpful for more ions adsorption. These changes in pore size and SSA can be understood in terms of the unique structure of the SSGA as revealed in Fig.5-3. The SWCNTs are sandwiched between the graphene layers to serve as spacers and, as a result, more graphene sheets are separated, which would in turn produce more mesopores and larger SSA. It should also be noted that excessive amount of carbon nanotubes in the composite would actually decrease the SSA (the SSA of SSGA-8 is lower than SSGA-12), which is ascribed to the lower SSA of SWCNTs than that of graphene.

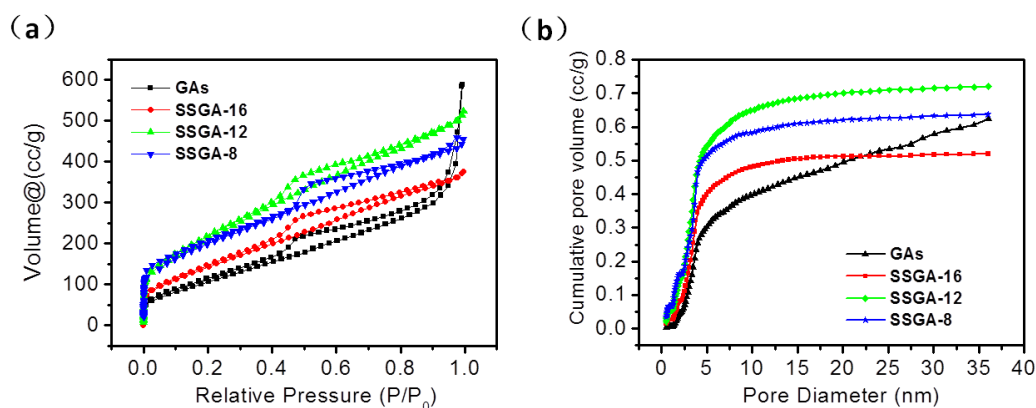


Figure 5-5. N₂ adsorption/desorption analysis of GA and SSGAs. (a) N₂ isotherm curves at 77.4 K. (b) Plots of cumulative pore volume versus pore diameter obtained from the adsorption isotherms.

Table 5-1. Specific surface area and pore volume of GAs and SSGAs.

Samples	Specific surface area (m ² g ⁻¹)	Pore volume of pores smaller than 8 nm (cc g ⁻¹)	Ratio of pore volume of pores smaller than 8nm
GAs	430	0.37	59.2 %
SSGA-16	551	0.46	88.1 %
SSGA-12	807	0.63	88.7 %
SSGA-8	712	0.57	89.0 %

5.3.3 Capacitance behaviors in aqueous electrolyte

The supercapacitor performance using the aerogel as the electrodes was first investigated in aqueous electrolyte (5 M KOH). The cyclic voltammograms (CVs) of GA, SSGA-16, SSGA-12, and SSGA-8 at different scan rates are shown in Fig. 5-6(a-d). It is observed that all CVs featured the rectangular shaped loops, indicating that the charges stored in the electrodes are dominated by the electric double-layer mechanism. Besides, all the CV loops retained the rectangular shape even at a high scan rate of 500 mV s⁻¹, suggesting their excellent rate capability, which is ascribed to the vast macropores in the aerogel that allow the electrode to be fast wetted by the electrolyte. To make a close comparison among the four electrodes, the CVs of different electrodes at 100 mV s⁻¹ are plotted in Fig. 5-6(e). The area within the CV loop is proportional to the charge storage capacity. As can be seen in the figure, all the three SSGA samples showed larger CV areas than the GA sample, indicating improved capacitance after incorporating the SWCNTs. The specific capacitance calculated on the scan rate is shown in Fig. 5-6(f). SSGA-12 exhibited the largest capacitance of 246.9 F g⁻¹ at 50 mV s⁻¹, which decreased to 206.9 F g⁻¹ (16% decrease) when the scan rate increased

to 500 mV s^{-1} . In contrast, GA showed a much lower capacitance of 179.3 F g^{-1} at 50 mV s^{-1} and a larger decrease of 24% to 135.9 F g^{-1} at 500 mV s^{-1} . The CV results indicate that both the specific capacitance and the rate capability are improved by introducing SWCNTs into the graphene aerogel.

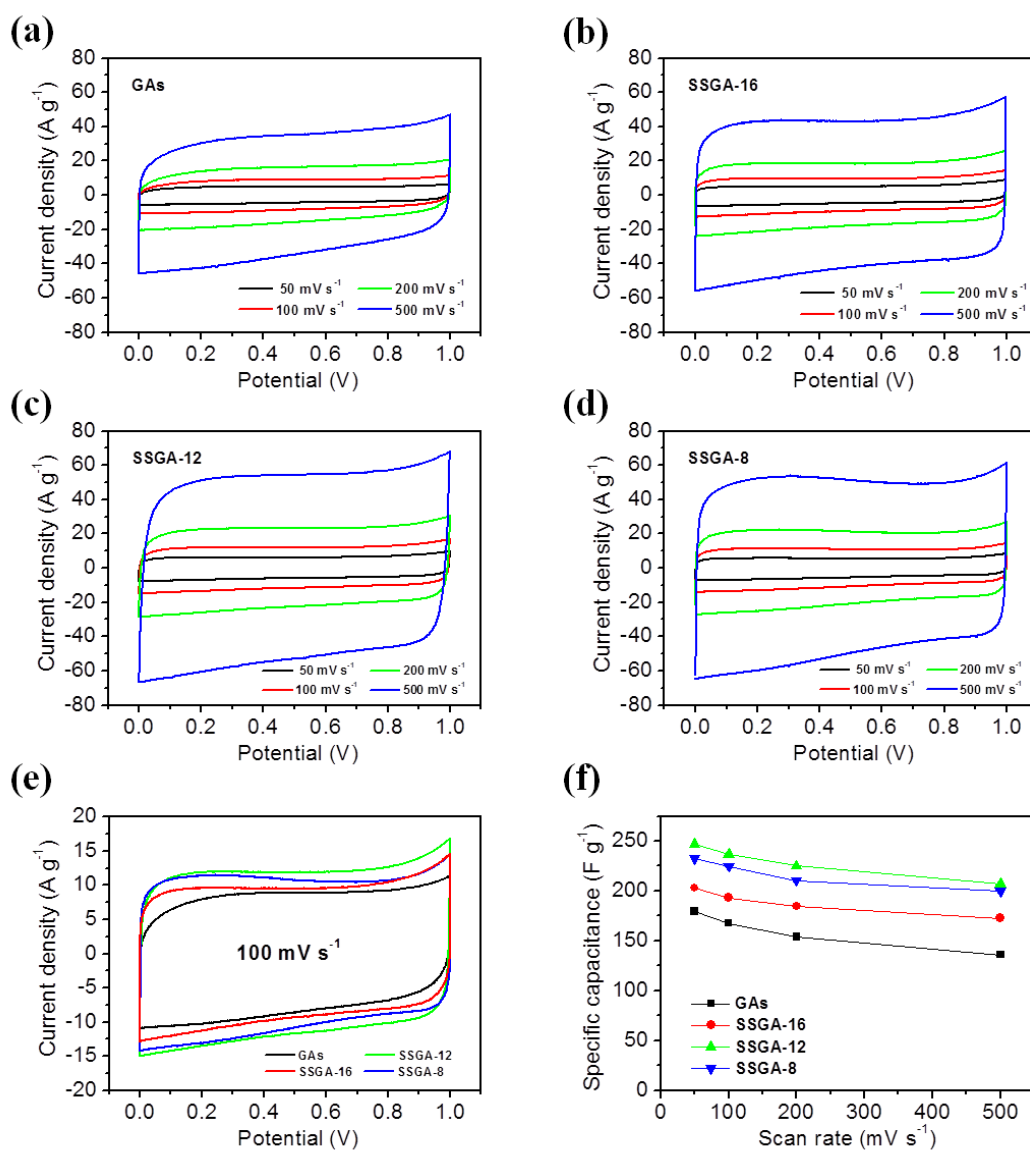


Figure 5-6 Electric double-layer capacitor performance in aqueous electrolyte. (a-d) CVs of the GA, SSGA-16, SSGA-12, and SSGA-8 at different scan rates from 50 to 500 mV s^{-1} . (e) CVs of different samples at a scan rate of 100 mV s^{-1} . (f) Dependence of specific capacitance on scan rate of the four graphene aerogel electrodes. SSGA-12 sample exhibited the best electrochemical performance.

Galvanostatic charge/discharge tests were performed to further investigate the supercapacitor properties of the aerogel electrodes in aqueous electrolyte. Fig. 5-7(a-d) are the charge/discharge profiles of GA, SSGA-16, SSGA-12, and SSGA-8 at different current densities from 5 to 80 A g^{-1} . As can be observed, all the curves are linear and symmetric and all have negligible IR drop, which further confirms the ideal electric double-layer capacitance. For comparison, the charge/discharge curves of different samples at a constant current density of 5 A g^{-1} are shown in Fig. 5-7(e). Evidently,

the charge and discharge time of all the three SSGA samples are longer than the GA sample at the same current density, indicating that the SSGA electrodes can store more energy than the GA electrode.

Table 5-2 Supercapacitor performance of the SSGA-12 sample in this study, compared with some graphene based aerogels, hydrogels, or other three dimensional structures for EDLCs application in previous literature.

Electrodes	Specific Capacitance	Rate capability
SSGA-12	245.5 F g⁻¹ at 2.5 A g⁻¹ 246.9 F g⁻¹ at 50 mV s⁻¹	80.2 % from 2.5 to 80 A g⁻¹ 83.8 % from 50 to 500 mV s⁻¹
Mechanically strong graphene aerogels (ref.1)	128.0 F g ⁻¹ at 0.05 A g ⁻¹	59.4 % from 0.05 to 20 A g ⁻¹
N,B co-doped graphene aerogels (ref.2)	239.0 F g ⁻¹ at 1 mV s ⁻¹	55.2 % from 1 to 100 mV s ⁻¹
3 D graphene aerogels (ref.3)	226.0 F g ⁻¹ at 1 mV s ⁻¹	36.7 % from 1 to 100 mV s ⁻¹
Graphene hydrogels (ref.4)	160±5 F g ⁻¹ at 1 A g ⁻¹	
Reduced graphene hydrogels (ref.5)	220.0 F g ⁻¹ at 1 A g ⁻¹	74.0 % from 1 to 100 A g ⁻¹
N doped graphene hydrogels (ref.6)	190.1 F g ⁻¹ at 10 A g ⁻¹	57.5 % from 10 to 185 A g ⁻¹
Graphene hydrogel films (ref.7)	186.0 F g ⁻¹ at 1 A g ⁻¹	70.0 % from 1 to 20 A g ⁻¹
Reduced graphene oxide foam (ref.8)	110.0 F g ⁻¹ at 0.5 A g ⁻¹	
Folded structured graphene paper (ref.9)	172.0 F g ⁻¹ at 1 A g ⁻¹	64.0 % from 1 to 100 A g ⁻¹

The calculated specific capacitance of the aerogels under different current densities is presented in Fig. 5-7(f). The specific capacitance at a loading current density of 2.5 A g⁻¹ for GA, SSGA-16, SSGA-12 and SSGA-8 are 179.0, 206.0, 245.5, and 230.5 F g⁻¹, respectively. The specific capacitance is very close to the value calculated from the CVs and also exhibited the same trend, indicating their high rate capability. Compared with GA, all the SSGA samples exhibited improved capacitance. In addition, it is interesting to note that the specific capacitance of the four samples are all in accordance with their BET SSA listed in Table 5-1, which further confirms the usefulness and functionalities of having SWCNT spacers to realize more accessible surface area and favorable pore structures. In particular the SSGA-12 sample shows the largest increment of 37% to reach 245.5 F g⁻¹, which is much higher than that of previously reported 3D macroscopic graphene based electrodes in aqueous electrolyte (as shown in Table 5-2), i.e., graphene hydrogels (160 F g⁻¹, 166 F g⁻¹, 186 F g⁻¹, 190.1 F g⁻¹), [14,26-28] graphene aerogels (128 F g⁻¹, 239 F g⁻¹), [16,29] folded graphene paper (172 F

g^{-1}),[8] or graphene foams (110 F g^{-1}).[9] Furthermore, when the current density is increased from 2.5 to 80 A g^{-1} , the specific capacitance of GA, SSGA-16, SSGA-12, and SSGA-8 becomes 121.0, 159.1, 197.0, and 192.3 F g^{-1} , corresponding to a retention of 68%, 77%, 80%, and 83%, respectively. It is clear that the rate capability is also improved after incorporating highly conductive SWCNTs to the graphene aerogel composite.

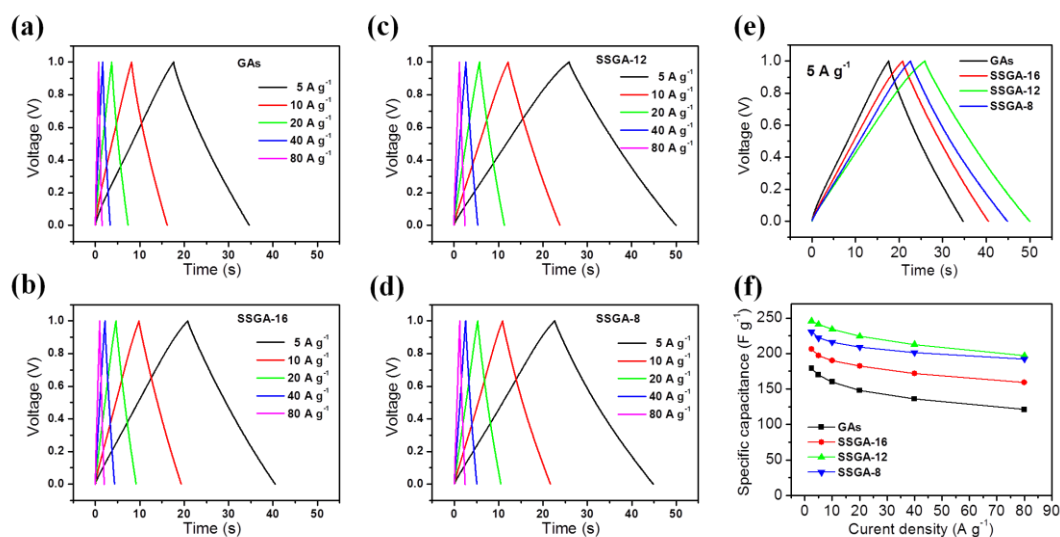


Figure 5-7 Electric double-layer capacitor performance of the graphene aerogel electrodes in aqueous electrolyte. (a-d) Galvanostatic charge/discharge curves of GA, SSGA-16, SSGA-12, and SSGA-8 at different current densities from 5 to 80 A g^{-1} . The current density was calculated based on the mass of a single electrode. (e) Charge/discharge curves of different samples at current densities of 5 A g^{-1} . (f) The dependences of specific capacitance on discharge current density of the four aerogel electrodes.

5.3.4 Capacitance behaviors in ionic liquid electrolyte

To explore further the electrochemical performance of the prepared graphene aerogels, EMIMBF₄, a room temperature ionic liquid with a wide potential window was employed as the electrolyte and the graphene aerogel electrodes were characterized in the voltage range of 0 to 3.5 V. Fig. 5-8(a) compares the CVs of GA and SSGAs at the scan rate of 50 mVs^{-1} . Just the same as in aqueous electrolyte, rectangular CVs were obtained, indicating the ideal electric double-layer capacitance in the ionic liquid electrolyte and SSGA-12 again showed the largest specific capacitance. Fig. 5-8(b) shows the CV of SSGA-12 at different scan rates from 20 to 100 mV s^{-1} and Fig. 5-8(e) shows the charge/discharge curves of SSGA-12 at different current densities from 1 to 10 A g^{-1} . As observed in the plots, the CVs retained the rectangular shape even at a high scan rate of 100 mV s^{-1} , and the charge/discharge curves followed the geometry of an isosceles triangle even at 10 A g^{-1} , indicating its excellent stability in the ionic liquid electrolyte. Fig. 5-8(f) displays the calculated specific capacitance of the aerogels under different current densities. At a low current density of 0.5

A g^{-1} , the specific capacitance of GA, SSGA-16, SSGA-12, and SSGA -8 are 137.4, 157.0, 183.3, and 167.9 F g^{-1} , respectively. All the capacitance values are understandably lower than that in the aqueous electrolyte due to the fact that the ionic liquid has larger molecular ions and larger viscosity. Compared with GA, all the SSGA samples also showed improved capacitance in the ionic liquid electrolyte, and SSGA-12 sample showed the largest increment of 33 % to a high capacitance of 183.3 F g^{-1} . Moreover, when the current density is increased by 20 times to 10 A g^{-1} , the remained capacitance for GA is only 97 F g^{-1} . However, thanks to the SWCNT spacers, a much higher capacitance, 154.3 F g^{-1} , which is 60% larger than that of GA, was retained for SSGA-12. Such an excellent rate performance demonstrates the rapid charge/discharge capability of the SSGA-12 electrode, which is particularly important and useful for supercapacitors requiring high energy densities.

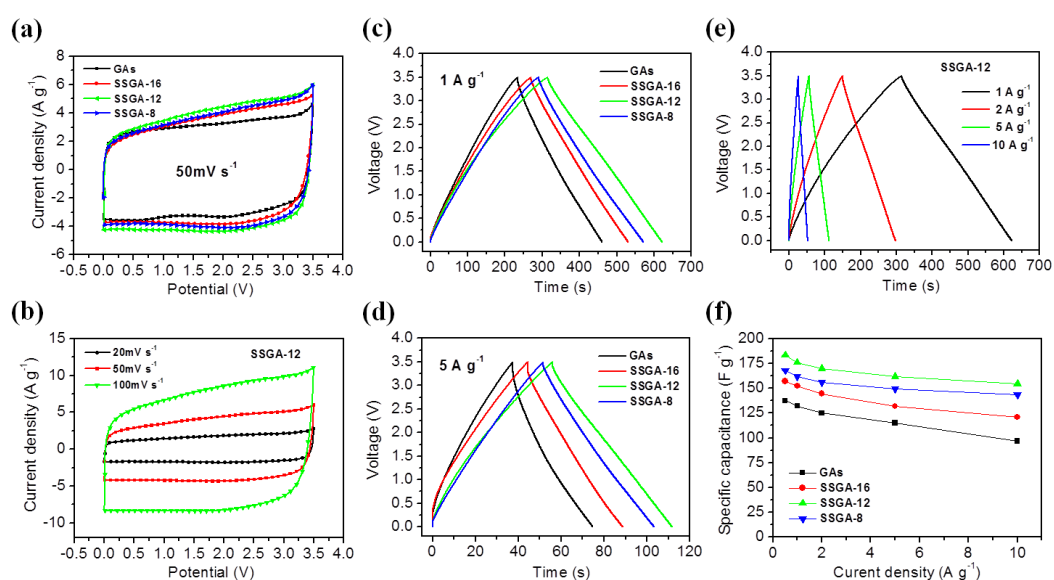


Figure 5-8 Electric double-layer capacitor performances in ionic liquid electrolyte. (a) CVs of GAs, SSGA-16, SSGA-12, and SSGA-8 at a scan rate of 50 mV s^{-1} . (b) CVs of SSGA-12 at different scan rates from 20 mV s^{-1} to 100 mV s^{-1} . (c, d) Galvanostatic charge/discharge curves of different samples at a current density of 1 and 5 A g^{-1} , respectively. (e) Charge/discharge curves of SSGA-12 at different current densities from 1 A g^{-1} to 10 A g^{-1} . (f) The dependences of specific capacitances on discharge current densities of the four aerogel electrodes.

5.3.5 EIS analysis

Electrochemical impedance spectroscopy (EIS) was also carried out to understand the reasons for the improved supercapacitor performance after having additive SWCNTs in the graphene aerogels. Fig. 5-9(a) and 5-9(b) show the Nyquist plots of the EIS data from GA and various SSGA electrodes in aqueous electrolyte and ionic liquid electrolyte, respectively. As can be observed, each plot consists of a semicircle at high frequencies and an almost vertical line at low frequencies, where the behaviors become mainly capacitive. The intercept on the horizontal axis gives the equivalent series

resistance (ESR). The ESR of the SSGA samples gradually decreased with increasing concentration of SWCNTs, attributed to the higher conductivity of SWCNTs. The semicircle in the Nyquist plot is closely related to the transport of electrolyte ions at the electrode/electrolyte interface and the radius of the semicircle is indicative of the charge transfer resistance (R_{ct}), which is associated with the porous structure of the electrode.[36] Generally, the smaller the radius of the semicircle, the higher the ion transport ability into the pores of the sample.[37-39]

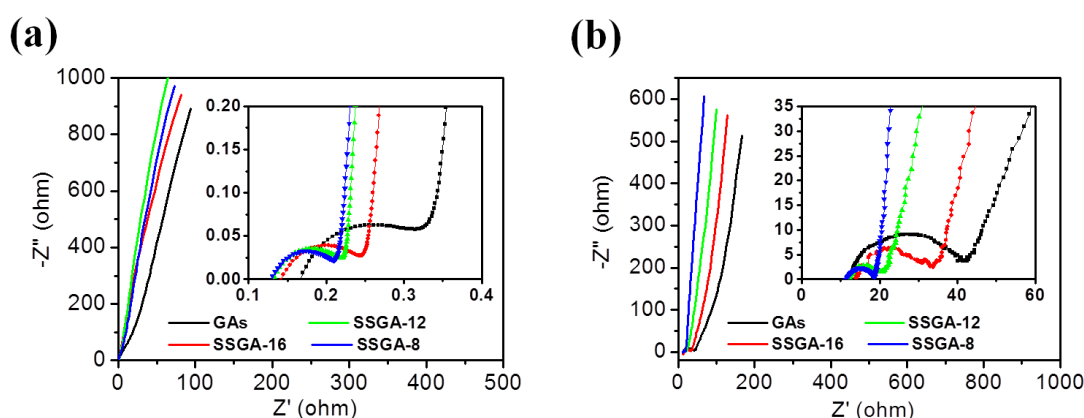


Figure 5-9. Nyquist plots of GAs, SSGA-16, SSGA-12, and SSGA-8 based cells in (a) aqueous electrolyte, and (b) ionic liquid electrolyte.

Table 5-3 lists the ESR and R_{ct} of the tested graphene aerogel samples. In aqueous electrolyte, the R_{ct} values of SSGAs are approximately only one half of GA and also decreased with increasing concentration of SWCNTs. This result means that the electrolyte ions could diffuse more easily in the SSGA samples, which is attributed to that the added SWCNTs served as spacers to increase the inter-layer spacing of graphene sheets and inhibit their restacking. The R_{ct} values obtained in the ionic liquid electrolyte also show the same trend. As can be observed, the values of ESR and R_{ct} of each sample are both larger than that in the aqueous electrolyte due to the lower conductivity and much higher viscosity of the ionic liquid. The R_{ct} of GA, SSGA-16, SSGA-12, and SSGA-8 are 18.5, 11.5, 5.0, and 4.3 Ω , respectively. The reduced R_{ct} after incorporating SWCNTs means that the diffusion of ions in the SSGA samples is much easier, which confirms again that the SWCNT spacers played an effective role in preventing the restacking of graphene sheets, leading to improved capacitance and rate capability. We also noted that the R_{ct} of SSGA-8 is almost the same as that of SSGA-12, indicating that further increases of SWCNTs in the composite electrode will not reduce it further. Instead, it will actually add more weight to the electrode and thus the optimal ratio of SWCNTs to GO is 1:12, which is in agreement with the electrochemical results.

Table 5-3. Comparison of ESR and R_{ct} of each electrode in aqueous and ionic liquid electrolyte obtained from the Nyquist plots of the EIS data.

Electrodes	Aqueous electrolyte		Ionic liquid electrolyte	
	ESR (m Ω)	R _{ct} (m Ω)	ESR (Ω)	R _{ct} (Ω)
GAs	166.6	121.4	12.0	18.5
SSGA-16	141.2	67.4	12.8	11.5
SSGA-12	132.2	56.5	11.7	5.0
SSGA-8	129.0	52.3	11.5	4.3

5.3.6 Ragone plot and cycle stability

The energy density of a supercapacitor is a vital indicator for its quality. The Ragone plot of SSGA-12 supercapacitor showing the relationship between the specific energy density (E) and the specific power density (P) is displayed in Fig. 5-10(a). In the aqueous electrolyte, SSGA-12 demonstrated a reasonable energy density of 8.5 Wh kg⁻¹ at a power density of 625 W kg⁻¹. As the energy density strongly depends on its operating voltage, the wide window of 0-3.5 V of the ionic liquid electrolyte made SSGA-12 electrode a much higher energy density: it exhibited a very high energy density of 80.0 Wh kg⁻¹ at a power density of 438 W kg⁻¹, which are about an order of magnitude higher than that of the previously reported 3D macroscopic graphene electrodes in aqueous electrolyte, and are even higher than some of the recently reported N-doped graphene, activated carbon, or mesoporous carbon in ionic liquid electrolyte.[40-43] In addition, even at a high power density of 9.1 kW kg⁻¹, the SSGA-12 electrode retained a high energy density of 65.6 Wh kg⁻¹, suggesting its excellent rate performance in the ionic liquid electrolyte. Fig. 5-10(b) shows the charge-discharge cycling performance of the SSGA-12 electrode in the aqueous electrolyte at a current density of 10 A g⁻¹ and in the ionic liquid electrolyte at a current density of 2 A g⁻¹. After 2000 cycles, 97% and 94% of its initial capacitance was preserved in the aqueous electrolyte and ionic liquid electrolyte, respectively, highlighting its cycling stability in both electrolytes.

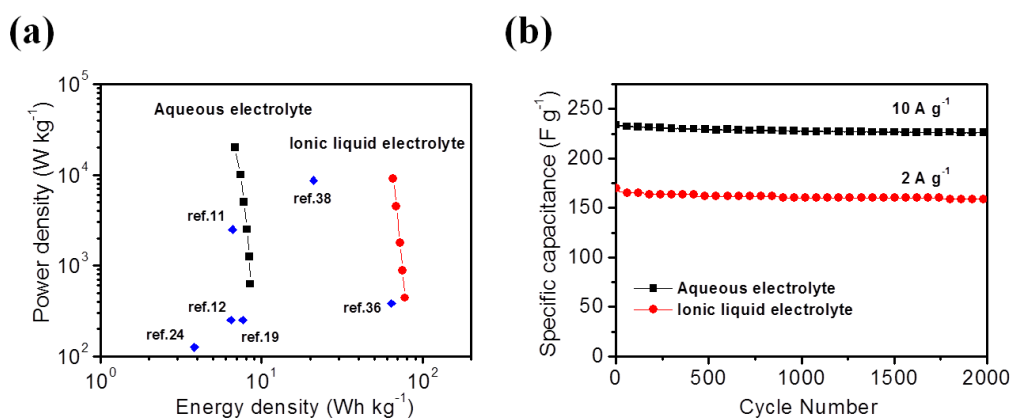


Figure 5-10 (a) Ragone plot, (b) Cycling performance of SSGA-12 sample in aqueous and ionic liquid electrolytes.

5.4 Conclusions

Single-walled carbon nanotube spaced graphene aerogel with desired porous structures were prepared for supercapacitor applications. Electrochemical tests showed that the graphene aerogel electrode delivered a high capacitance of 245.5 F g^{-1} in aqueous electrolyte (5M KOH) and a high capacitance of 183.3 F g^{-1} in ionic liquid electrolyte (EMIMBF₄). An extremely high energy density of 80.0 Wh kg^{-1} in the ionic liquid electrolyte has been achieved with the graphene aerogel supercapacitor electrode. The graphene aerogel supercapacitor also showed excellent rate capability and long cycle life.

References

1. P. Simon, Y. Gogotsi, *Nat Mater*, 7 (2008) 845-854.
2. J.R. Miller, P. Simon, *Science*, 321 (2008) 651-652.
3. L.L. Zhang, X.S. Zhao, *Chem. Soc. Rev*, 38 (2009) 2520-2531.
4. M.D. Stoller, S.J. Park, Y.W. Zhu, J.H. An, R.S. Ruoff, *Nano Lett*, 8 (2008) 3498-3502.
5. J.Y. Luo, H.D. Jang, J.X. Huang, *ACS Nano*, 7 (2013) 1464-1471.
6. Z. Wen, X. Wang, S. Mao, Z. Bo, H. Kim, S. Cui, G. Lu, X. Feng, J. Chen, *Adv. Mater*, 24 (2012) 5610-5616.
7. Y. Zhu, S. Murali, M.D. Stoller, K.J. Ganesh, W. Cai, P.J. Ferreira, A. Pirkle, R.M. Wallace, K.A. Cychoz, M. Thommes, D. Su, E.A. Stach, R.S. Ruoff, *Science*, 332 (2011) 1537-1541.
8. C. Liu, Z. Yu, D. Neff, A. Zhamu, B.Z. Jang, *Nano Lett*, 10 (2010) 4863-4868.
9. F. Liu, S. Song, D. Xue, H. Zhang, *Adv. Mater*, 24 (2012) 1089-1094.
- 10]. Z. Niu, J. Chen, H.H. Hng, J. Ma, X. Chen, *Adv. Mater*, 24 (2012) 4144-4150.
11. J.J. Yoo, K. Balakrishnan, J.S. Huang, V. Meunier, B.G. Sumpter, A. Srivastava, M. Conway, A.L.M. Reddy, J. Yu, R. Vajtai, P.M. Ajayan, *Nano Lett*, 11 (2011) 1423-1427.
12. Y. Yoon, K. Lee, S. Kwon, S. Seo, H. Yoo, S. Kim, Y. Shin, Y. Park, D. Kim, Y.-y. Choi, H. Lee, *ACS Nano*, 8 (2014) 4580-4590
13. J. Lee, S. Kim, J. Yoo, J. Jang, *ACS nano*, 7 (2013) 6047-6055.
14. Y.X. Xu, K.X. Sheng, C. Li, G.Q. Shi, *ACS Nano*, 4 (2010) 4324-4330.
15. Y. Zhao, C. Hu, Y. Hu, H. Cheng, G. Shi, L. Qu, *Angew. Chem. Int. Ed*, 48 (2009) 5864-5868.
16. Z.S. Wu, A. Winter, L. Chen, Y. Sun, A. Turchanin, X. Feng, K. Mullen, *Adv. Mater*, 24 (2012) 5130-5135.
17. S. Ye, J. Feng, *ACS App. Mater. Interfaces*, 6 (2014) 9671-9679.
18. H.-F. Ju, W.-L. Song, L.-Z. Fan, *J. Mater. Chem. A*, 2 (2014) 10895.
19. Q. Cheng, J. Tang, J. Ma, H. Zhang, N. Shinya, L.C. Qin, *Phys. Chem. Chem. Phys.*, 13 (2011) 17615-17624.
20. F. Zhang, J. Tang, N. Shinya, L.-C. Qin, *Chem. Phys. Lett*, 584 (2013) 124-129.
21. J. Yan, T. Wei, B. Shao, F. Ma, Z. Fan, M. Zhang, C. Zheng, Y. Shang, W. Qian, F. Wei,

Carbon, 48 (2010) 1731-1737.

22. X. Du, H. Song, X. Chen, *J. Mater. Chem.*, 22 (2012) 13091.
23. Y. Yu, Y. Sun, C. Cao, S. Yang, H. Liu, P. Li, P. Huang, W. Song, *J. Mater. Chem. A*, 2 (2014) 7706.
24. Y. Zhu, L. Li, C. Zhang, G. Casillas, Z. Sun, Z. Yan, G. Ruan, Z. Peng, A.R. Raji, C. Kittrell, R.H. Hauge, J.M. Tour, *Nat. Commun*, 3 (2012) 1225.
25. F. Zhang, J. Tang, Z. Wang, L.-C. Qin, *Chem. Phys. Lett*, 590 (2013) 121-125.
26. P. Chen, J.J. Yang, S.S. Li, Z. Wang, T.Y. Xiao, Y.H. Qian, S.H. Yu, *Nano Energy*, 2 (2013) 249-256.
27. Z.L. Yuxi Xu, Xiaoqing Huang, Yuan Liu, Yu Huang, Xiangfeng Duan, *ACS nano*, 7 (2013) 4042-4049.
28. W. Chen, L. Yan, *Nanoscale*, 3 (2011) 3132-3137.
29. Z.S. Wu, A. Winter, L. Chen, Y. Sun, A. Turchanin, X. Feng, K. Mullen, *Adv. Mater*, 24 (2012) 5130-5135.
30. Y. Zhao, C. Hu, L. Song, L. Wang, G. Shi, L. Dai, L. Qu, *Energ Environ Sci*, 7 (2014) 1913-1918.
31. L. Qiu, X. Yang, X. Gou, W. Yang, Z.F. Ma, G.G. Wallace, D. Li, *Chem. Eur. J*, 16 (2010) 10653-10658.
32. L. Tian, M.J. Meziani, F. Lu, C.Y. Kong, L. Cao, T.J. Thorne, Y.P. Sun, *ACS App. Mater. Interfaces*, 2 (2010) 3217-3222.
33. L. Borchardt, M. Oschatz, S. Kaskel, *Mater. Horiz*, 1 (2014) 157.
34. Z. Sui, Q. Meng, J. Li, J. Zhu, Y. Cui, B. Han, *J. Mater. Chem. A*, 2 (2014). 9891-9898
35. Z.-j. Jiang, Z. Jiang, W. Chen, *J. Power Sources*, 251 (2014) 55-65.
36. L. Zhang, F. Zhang, X. Yang, G. Long, Y. Wu, T. Zhang, K. Leng, Y. Huang, Y. Ma, A. Yu, Y. Chen, *Sci Rep*, 3 (2013) 1408-1416
37. C.-L. Liu, W. Dong, G. Cao, J. Song, L. Liu, Y. Yang, *J. Electrochem. Soc*, 155 (2008) F1-F7.
38. F. Xu, R. Cai, Q. Zeng, C. Zou, D. Wu, F. Li, X. Lu, Y. Liang, R. Fu, *J. Mater. Chem*, 21 (2011) 1970.
39. H. Zhong, F. Xu, Z. Li, R. Fu, D. Wu, *Nanoscale*, 5 (2013) 4678-4682.
40. M. Sathish, S. Mitani, T. Tomai, I. Honma, *J. Mater. Chem. A*, 2 (2014) 4731-4738.
41. M. Galinski, K. Babel, K. Jurewicz, *J. Power Sources*, 228 (2013) 83-88.
42. A. Vu, X.Y. Li, J. Phillips, A.J. Han, W.H. Smyrl, P. Buhlmann, A. Stein, *Chem Mater*, 25 (2013) 4137-4148.
43. Z. Lei, Z. Liu, H. Wang, X. Sun, L. Lu, X.S. Zhao, *J. Mater. Chem. A*, 1 (2013) 2313-2321.

Chapter 6

Curved graphene from Ionic liquid mediated reduction of graphene oxide for supercapacitor with improved rate capability in ionic liquid electrolyte

6.1 Introduction

Supercapacitors, as a kind of energy storage device, have received extensive attention worldwide because of their unique characteristics including high power density, long cyclic lifetime and low maintenance cost. These features make supercapacitor as a potential versatile power supply for portable electronic devices, hybrid electric vehicles, solar cell panels, memory back-up, especially where peak power is necessarily needed.[1-3] In the recent years, graphene, a monolayer carbon material with large theoretical specific surface area over $2600 \text{ m}^2 \text{ g}^{-1}$ and high conductivity, has been considered as an ideal electrode material for electrical double layer capacitors (EDLCs).[4-8] For graphene based supercapacitors, one challenging yet really important issue is to increase their energy densities. It is well known that the energy density (E) of a supercapacitor is related to the gravimetric cell capacitance (C) and operating voltage (V) by the formula $E = CV^2/2$. So, increasing the operating voltage is crucial to the increase of the energy density of supercapacitors, since the latter increased two orders of magnitude with the former. In general, the operating voltage of supercapacitors is limited by the electrochemical window of the electrolyte. Compared with traditional aqueous electrolytes, ionic liquids (ILs) with an original electrochemical window up to 3.5 to 4V, have been employed as the electrolytes to boost the energy density of graphene based supercapacitors. For example, we have recently reported some graphene based electrodes could exhibit high energy densities of 80-150 kWh kg^{-1} in IL electrolytes, which are an order of magnitude higher than that in aqueous electrolytes.[9-11] So it appears that ILs would be the state-of-the-art electrolytes for graphene based high energy supercapacitors if their cost could be reduced to a acceptable degree.

However, apart from the relative high cost, there still exists another obstacle for the application of ILs as electrolytes for supercapacitors. Compared with aqueous electrolytes, ILs usually have larger molecules, lower conductivity, and higher viscosity, which would cause the electrodes could

not be fast wetted by the IL ions, thus render a relative low rate capability for IL electrolytes based supercapacitors. Imagine that if the supercapacitor could not be charged and discharged quickly, the obtained high energy density benefited from IL electrolytes would be meaningless compared with batteries. To address this issue, organic solvents or single-walled carbon nanotubes have been added into IL electrolytes to reduce the viscosity and increase the ionic conductivity.[12, 13] However, these efforts are all focused on improving the properties of IL electrolytes, and there is a lack of attention on tuning the surface of the electrodes to make them more compatible with IL electrolytes.

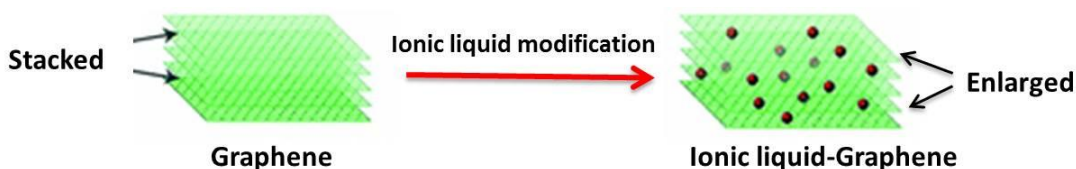


Fig 6-1 Schematic illustration of the enlarged interlayer spacing of ionic liquid modified graphene.

Here, in this communication, we report the use of IL modified reduced graphene oxide (RGO-IL) as an advanced electrode to significantly increase the rate capability of graphene based supercapacitors in IL electrolytes. This concept is based on the fact that electrochemical double layer capacitances come from ions absorption on the surface of the electrodes, so tailoring the surface chemistry of the electrodes would be an effective approach to improve their capacitance behaviors. Considering the being absorbed electrolyte is IL, we choose the same IL as a functionalizer to modify the graphene surface with the aims of increasing their compatibility with each other. Besides, the ionic liquid molecules can also serve as spacers to enlarge the interlayer of graphene. Electrochemical test results show that the relaxation time and charge transfer resistance at electrode-electrolyte interface for RGO-IL electrode is one third and one fourth of that for RGO electrode, respectively, indicating the improved compatibility between the modified electrode and the electrolyte. Benefited from that, the capacitance retention of RGO-IL electrode from current density of 0.5 A g^{-1} to 20 A g^{-1} is 84.4 %, which is extremely higher than that of RGO electrode (52.9 %). These results clearly demonstrate surface modification of RGO electrode by ILs is indeed an effective way to improve the rate capability of IL electrolytes based supercapacitors. More importantly, different from previous method focused on improving IL electrolytes, our concept sheds some light on new strategies to improve rate capability of IL electrolytes based supercapacitors and this method is facile and effective, and holds the potential to be a general way for solution processed graphene based electrodes with improved rate capability in IL electrolytes.

6.2 Experimental section

6.2.1 Preparation of Graphene oxide (GO).

GO was prepared from the natural graphite powder according to a modified Hummers' method.

Briefly, 3.0 g of graphite powder was mixed with 70 mL 98 wt % sulfuric acid in an ice-bath., then 1.5 g sodium nitrate was added. After stirring 5 min, 9.0 g potassium permanganate was slowly added so that the temperature did not exceed 20 °C . The reaction system was transferred to a 35 °C water bath for 1 h, forming a thick paste. After that, 140 mL of deionized water gradually added into the mixture. The mixture was stirred for another 1 h, followed by a addition of 500 mL water. After 30 min, 20 mL of H₂O₂ was slowly added and the color changed from dark brown to yellow. The suspension was centrifuged and washed with 1 M HCl solution and deionized water six times to remove the metal ions and acid. The obtained products were dried under vacuum to get GO powders. Finally, GO powders were dispersed in water by ultrasonication for 2 h to make a homogeneous GO aqueous dispersion of 1 mg/mL.

6.2.2 Preparation of Reduce Graphene oxide (RGO).

RGO was prepared by chemical reduction of GO. 100 mL GO aqueous dispersion (1 mg/mL) was stirred in a 300 mL flask. Then, it was heated to 98 °C and 0.1 mL hydrazine solution (35 wt %) was added in. The mixture was kept at 98 °C for 2 h under reflux. Finally, the product was washed with water and dried in an oven at 60 °C.

6.2.3 Preparation of Ionic liquid modified reduced graphene oxide (RGO-IL).

RGO-IL was prepared by chemical reduction of GO in the presence of ionic liquid. 100 mL GO aqueous dispersion (1 mg/mL) was stirred in a 300 mL flask. Firstly, 0.5 mL ionic liquid EMIMBF₄ was added into the suspension. After 30 min stirring, it was heated to 98 °C and 0.1 mL hydrazine solution (35 wt%) was added in. The mixture was kept at 98 °C for 2 h under reflux. Finally, the product was washed with water and dried in an oven at 60 °C.

6.2.4 Characterization.

The morphology and structure of samples were examined by Scanning Electron Microscope (SEM) using JSM-6500 field-emission scanning electron microscope with acceleration voltage of 15 KV. Transmission electron microscope (TEM) was carried on a JEM-2100 electron microscope. Raman spectra were obtained with RAMAN-11 (Nanophoton) with a 532 nm laser source. Fourier transformation infrared (FT-IR) spectra were recorded using a Nicolet 6700 machine. The specific surface area and pore sized distribution were measured by BET on an Autosorb-iQ analyzer. The specific surface area (SSA) was calculated by BET method based on adsorption data in the relative pressure (P/P_0) range of 0.05 to 0.3.

6.2.5 Electrochemical measurements.

The industry-level two electrode symmetrical supercapacitors were fabricated to measure the electrochemical performance of as obtained samples. Briefly, 90 wt % samples and 10 wt % PTFE were dispersed in ethanol by sonication and then the suspension was filtered onto a porous filter membrane by vacuum filtration. After vacuum drying for 24h, all electrodes were prepared by cutting the filtered films into circular disks with diameter of 15 mm and a weight of about 1 mg for each electrode. The two-electrode cell device was fabricated in a glove box filled with Ar. A porous separator was placed between two electrodes in a stainless cell. EMIMBF₄ was used as the ionic liquid electrolytes.

Electrochemical measurements were carried out at room temperature using a multi-channel VMP-300 electrochemical workstation. The potential range for CV measurements and galvanostatic charge-discharge tests was 0-3.5 V. The gravimetric specific capacitance, C_s (F/g) was calculated according to $C_s = \frac{4I}{m dV/dt}$, where I (A) is the constant current, m (g) is the total mass of the two electrodes and dV/dt (V/s) is the slope obtained by fitting a straight line to the discharge curve over the range of V_{max} (the voltage at the beginning of discharge) to $1/2 V_{max}$. In the Ragone plots, the energy density, E_{cell} (Wh kg⁻¹), was estimated using the formula $E_{cell} = C_s V^2 / 8$. The power density, P_{cell} (W kg⁻¹) was estimated by $P_{cell} = E_{cell} / t$, where t is the discharge time. EIS tests were carried out in the frequency range of 100 kHz-0.01 Hz at open circuit potential with an AC amplitude of 5 mV. Based on a RC model, the capacitance was also calculated from the frequency response analysis to show the trend of changes in capacitance with frequency, according to $C = -1 / (2\pi f Z'')$, where f is frequency (Hz) and Z'' is the imaginary part of the impedance.

6.3 Results and discussion

The RGO-IL was prepared by chemical reduction of graphene oxide (GO) in presence of a hydrophilic IL (EMIMBF₄). The morphology and structure of RGO and RGO-IL were revealed by scanning (SEM) and transmission electron microscopy (TEM). SEM images (Fig.6-2) show that RGO-IL displays a porous structure with hierarchical curved sheets, which would provide more exposed surface for ions adsorption. This morphology is totally different from RGO prepared in the absence of ILs, which shows compact structures. TEM observation (Fig.6-3) also shows the curved characteristic of RGO-IL. Besides, the sheets of RGO-IL are thinner than the multi-layer stacked RGO. Morphology changes is a common phenomenon in ILs mediated reactions, especially in the synthesis of some unique structured inorganic compound.[14,15] Here, in this system, considering the previously reported good dispersibility of graphene in ILs,[16] ILs may serve as a surfactant and a soft template to make the just reduced graphene sheets more separated and curved.

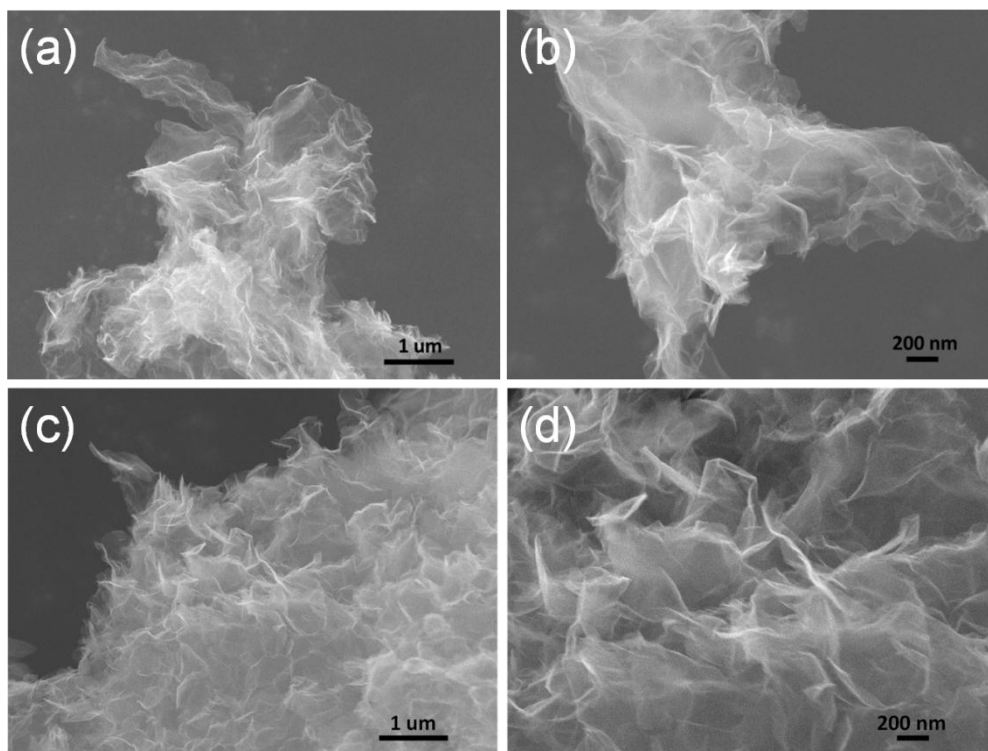


Fig 6-2 SEM images of RGO (a,b); and RGO-IL (c,d).

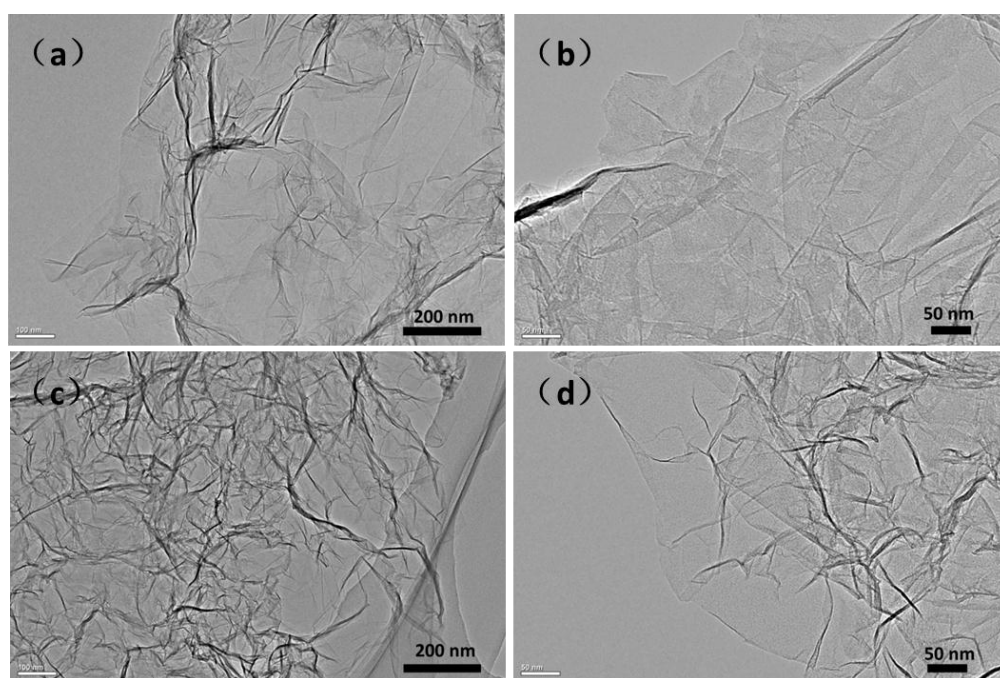


Fig 6-3 TEM images of RGO (a,b); and RGO-IL (c,d).

The porous structure of RGO-IL was further confirmed in Raman analyses (Fig.6-4). The intensity ratio of I_D/I_G for RGO-IL is apparently larger compared with RGO, indicating the increased defect degree induced by the curved structure. The ILs surface modification was verified in FT-IR results (Fig.6-5). As can be observed, additional adsorption bands of IL (EMIMBF₄) at 3160 cm⁻¹ and

3090 cm^{-1} , 1572 cm^{-1} , 1065 cm^{-1} , corresponding to the stretching vibrations of CH_x unsaturated bonds, C-N bonds from the imidazolium ring, and the B-F bonds of $[\text{BF}_4]^-$ anions, respectively, were found in the spectra of RGO-IL, implying the successful modification of IL to the reduced graphene.[17]

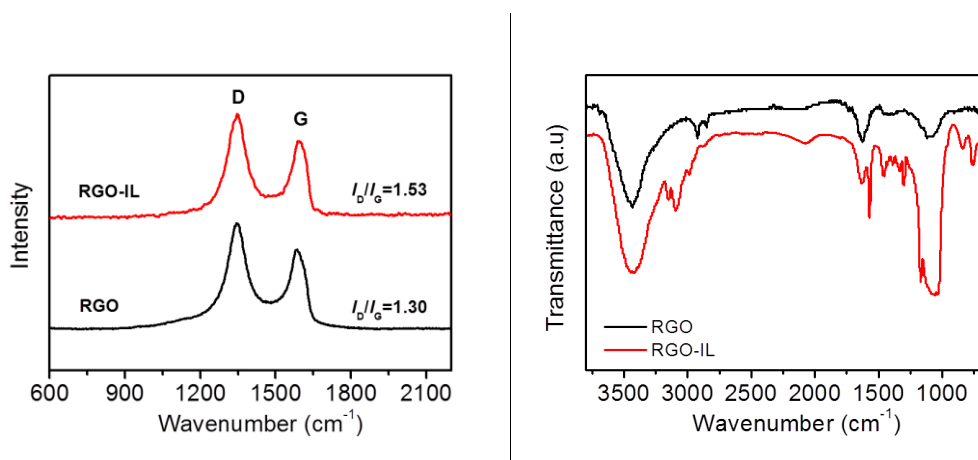


Fig. 6-6 (a) FT-Raman, and (b) FT-IR of RGO and RGO-IL.

The specific surface areas (SSAs) and the pore structures of RGO and RGO-IL were studied by nitrogen isothermal adsorption (Fig.6-7). The adsorption isotherm of RGO reveals a character of type IV, which is typical for the adsorption of mesopores. However, RGO-IL exhibits a combined type III and IV isotherm, indicating that a certain number of macropores also exist in RGO-IL in addition to mesopores. The existence of macropores is consistent with the results of SEM and TEM measurement, which show porous structures. It should be noted that these macropores induced by IL mediate reduction would benefit to the rate ability of RGO-IL electrode because the electrolyte ions diffusion to macropores is rather easier than mesopores. Besides, the peak pore diameter of RGO-IL in the pore size distribution plot is a little larger than that of RGO, which further confirm the more separated graphene sheets due to the “surfactant” IL. Benefited from the more separated structure, a larger SSA of 433.1 $\text{m}^2 \text{g}^{-1}$ for RGO is obtained compared with RGO (324 $\text{m}^2 \text{g}^{-1}$).

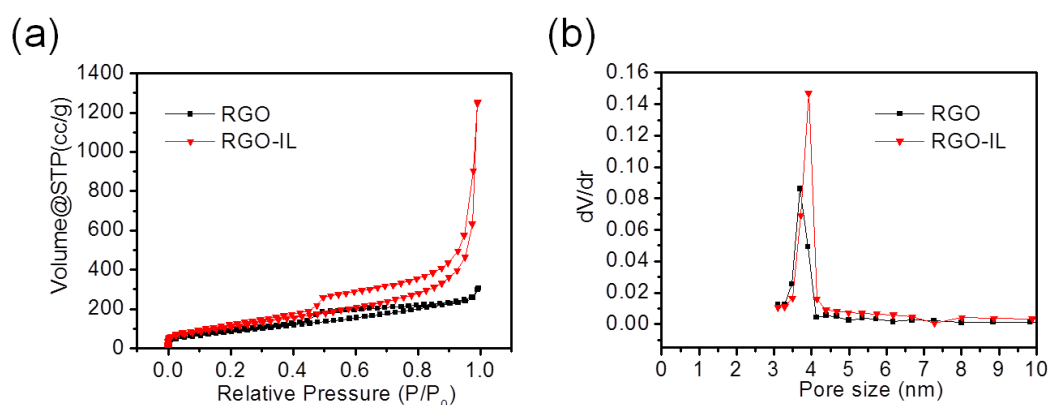


Fig. 6-7 (a) Nitrogen adsorption isotherms, (b) BJH desorption pore size distribution curves of RGO and RGO-IL.

The supercapacitor performances of RGO and RGO-IL were investigated by a two-electrode symmetrical test configuration with the same ionic liquid (EMIMBF₄) as the electrolyte. Fig.6-8a and b show the comparative cyclic voltammetry (CV) curves of RGO and RGO-IL electrodes at low and fast scanning rates, respectively. At the low scanning rate of 50 mV s⁻¹, both CV profiles exhibit rectangular shapes, indicating their ideal electrical double-layer capacitances. However, when the scanning rate increases for ten times, rectangular shaped CV curves can only be observed for RGO-IL electrode, demonstrating its superior rate capability. This trend is more obvious in the charge-discharge results, which shows the discharge time of RGO-IL electrode is significantly larger than that of RGO at high current density of 20 A g⁻¹ (Fig.6-8d). The dependence of gravimetric capacitances on the current densities is presented in Fig.6-8e. At a low current density of 0.5 A g⁻¹, RGO-IL electrode exhibits a slightly higher capacitance of 135.4 F g⁻¹ than RGO (129.0 F g⁻¹), which may be due to the larger SSA of RGO-IL. When the current density increases for forty times, the maintained capacitance of RGO electrode is only 68.3 F g⁻¹, corresponding to a low retention of 52.9 %, revealing its poor rate capability owing to the low conductivity and high viscosity of IL electrolyte. However, after IL modification, a high specific capacitance of 114.3 F g⁻¹, corresponding to a large retention of 84.4 %, can be reserved for RGO-IL electrode under the same condition. This super high retention is much better than bare RGO electrode and even comparable to some reported RGO electrode in aqueous electrolytes,[18-20] evidently revealing the significant importance of IL modification to the improvement of rate capability for graphene supercapacitors in IL electrolytes. Furthermore, the Ragone plots shown in Fig. 6-8f further demonstrate the improved rate performance of RGO-IL electrode. Even at a high power density of 17.5 kW kg⁻¹, the RGO-IL electrode still deliver a high energy density of 48.6 Wh kg⁻¹, which is much larger than that of RGO (29.0 Wh kg⁻¹). Additionally, RGO-IL electrode exhibits excellent cycling stability. It can retain over 91.6 % of capacitance after 2000 cycles even under a high current density of 10 A g⁻¹, which is better than RGO electrode (81.5 %).

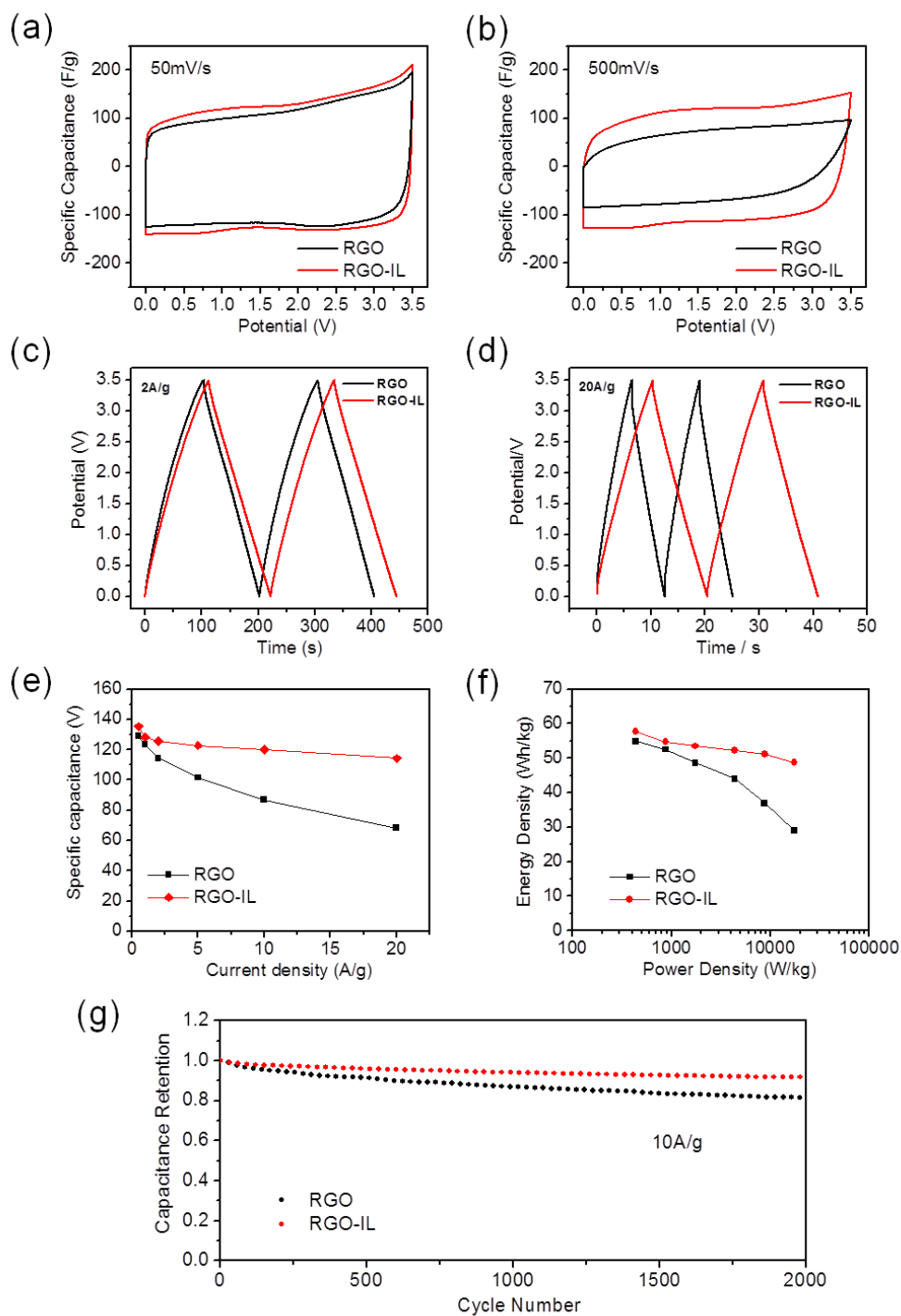


Fig. 6-8 Supercapacitor performances of RGO and RGO-IL in ionic liquid electrolyte with a two-electrode cell. (a,b) CV curves obtained at slow and fast scan rates; (c,d) Charge/discharge curves obtained at different current densities; (e) Gravimetric capacitances measured at various charge/discharge current densities; (f) Ragone plots; (g) Cycling performances.

To understand the reasons for the improved rate capability after IL modification, electrochemical impedance spectroscopy (EIS) technique was employed to examine the interface properties of RGO and RGO-IL electrodes with the IL electrolyte. Fig.6-9a displays the Nyquist plots of RGO and

RGO-IL based supercapacitors. The equivalent series resistance (ESR) from the intercept along the x-axis for RGO-IL is lower than RGO, which can be ascribed to the better contact with current collector due to its porous structure. The radius of the semicircle in the Nyquist usually represents the charge transfer resistance (R_{ct}), which is closely related to the transport of electrolyte ions at the electrode/electrolyte interface.[21] After IL modification, the R_{ct} value of RGO-IL is 0.86Ω , which is only one-fourth of that of RGO (3.5Ω), clearly demonstrating the improved compatibility between the modified electrode and IL electrolyte. The largely reduced resistance would facilitate fast ions adsorption/desorption, thus improving the rate capability of supercapacitors. Moreover, Fig.6-9b shows the frequency response of RGO and RGO-IL electrodes range from 100 kHz and 10 mHz. the operating frequency $f_{0.5}$ (the frequency at which the capacitance is 50 % of its maximum value)[22] of HGO-IL and HGO is 18.6 Hz and 5.75 Hz, respectively, which corresponds to a relaxation time constant $\tau_0 (= 1/f_{0.5})$ of 53.6 ms for RGO-IL, about one-third of that of RGO (173.9 ms). This rapid frequency response of RGO-IL further confirms the significantly improved compatibility between the modified electrode and IL electrolyte. Two main reasons maybe account for the improved compatibility between IL modified graphene electrode and IL electrolyte. First, the curved morphology induced by IL “surfactant”, provides a more conductive and more electrolyte-accessible network; second, the presence of IL on the surface of graphene sheets would weaken the surface free energy and serve as a directing agent to promote ions adsorption.

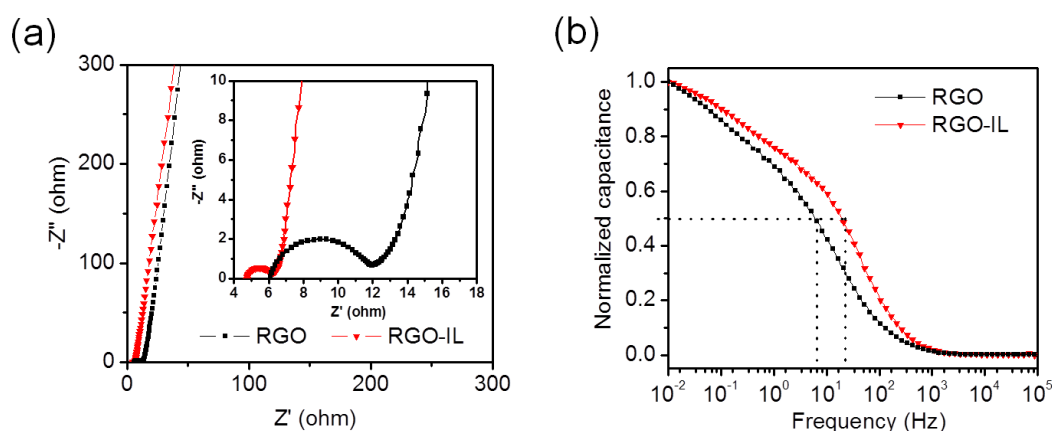


Fig. 6-9 (a) Nyquist plots of RGO and RGO-IL electrodes. The inset shows an expanded view for the high frequency. (b) Frequency response of RGO and RGO-IL electrodes.

6.4 Conclusions

In summary, we have demonstrated surface modification of RGO electrode by IL is an effective way to improve the rate capability of supercapacitor with IL electrolytes. The IL modification can significantly improve the compatibility between the modified electrode and IL electrolyte. Electrochemical tests reveal the modified electrode can exhibit much higher capacitance retention under high current density. More importantly, different from previous effort focused on improving IL

electrolytes, this study potentially opens up a new, simple, and effective route to improve the rate capability of graphene based supercapacitors in IL electrolytes.

References

1. G. Wang, L. Zhang and J. Zhang, *Chemical Society reviews*, 2012, **41**, 797-828.
2. G. Yu, X. Xie, L. Pan, Z. Bao and Y. Cui, *Nano Energy*, 2013, **2**, 213-234.
3. P. Simon and Y. Gogotsi, *Nature materials*, 2008, **7**, 845-854.
4. M. D. Stoller, S. Park, Y. Zhu, J. An and R. S. Ruoff, *Nano letters*, 2008, **8**, 3498-3502.
5. Y. Zhu, S. Murali, M. D. Stoller, K. J. Ganesh, W. Cai, P. J. Ferreira, A. Pirkle, R. M. Wallace, K. A. Cyhosh, M. Thommes, D. Su, E. A. Stach and R. S. Ruoff, *Science*, 2011, **332**, 1537-1541.
6. W. J. Lee, U. N. Maiti, J. M. Lee, J. Lim, T. H. Han and S. O. Kim, *Chemical communications*, 2014, **50**, 6818-6830.
7. B. Luo, S. Liu and L. Zhi, *Small*, 2012, **8**, 630-646.
8. Y. B. Tan and J.-M. Lee, *Journal of Materials Chemistry A*, 2013, **1**, 14814.
9. Q. Cheng, J. Tang, J. Ma, H. Zhang, N. Shinya and L. C. Qin, *Physical chemistry chemical physics : PCCP*, 2011, **13**, 17615-17624.
10. F. Zhang, J. Tang, N. Shinya and L.-C. Qin, *Chemical Physics Letters*, 2013, **584**, 124-129.
11. Q. Shao, J. Tang, Y. Lin, F. Zhang, J. Yuan, H. Zhang, N. Shinya and L.-C. Qin, *Journal of Materials Chemistry A*, 2013, **1**, 15423.
12. V. Ruiz, T. Huynh, S. Sivakkumar and A. Pandolfo, *RSC Advances*, 2012, **2**, 5591-5598.
13. C. Kong, W. Qian, C. Zheng, Y. Yu, C. Cui and F. Wei, *Chemical communications*, 2013, **49**, 10727.
14. B. L. Cushing, V. L. Kolesnichenko and C. J. O Connor, *Chemical reviews*, 2004, **104**, 3893-3946.
15. Z. Ma, J. Yu and S. Dai, *Advanced materials*, 2010, **22**, 261-285.
16. X. Zhou, T. Wu, K. Ding, B. Hu, M. Hou and B. Han, *Chemical communications*, 2010, **46**, 386-388.
17. K. Liu, J. Zhang, G. Yang, C. Wang and J.-J. Zhu, *Electrochemistry Communications*, 2010, **12**, 402-405.
18. Y. Xu, Z. Lin, X. Huang, Y. Liu, Y. Huang and X. Duan, *ACS nano*, 2013, **7**, 4042-4049.
19. Z. Lei, L. Lu and X. S. Zhao, *Energy & Environmental Science*, 2012, **5**, 6391.
20. F. Liu, S. Song, D. Xue and H. Zhang, *Advanced materials*, 2012, **24**, 1089-1094.
21. L. Zhang, F. Zhang, X. Yang, G. Long, Y. Wu, T. Zhang, K. Leng, Y. Huang, Y. Ma, A. Yu and Y. Chen, *Scientific reports*, 2013, **3**, 1408.
22. X. Yang, J. Zhu, L. Qiu and D. Li, *Advanced materials*, 2011, **23**, 2833-2838.

Chapter 7

Fabrication of a Highly Porous Carbon Nanofiber Paper with Large External Surface Area and Its Application for High Energy Density Supercapacitors

7.1 Introduction

With the rapid growth of the economic expansion, the energy consumption, and the environmental pollution, there has been an urgent need for cheap, clean, and renewable energy sources. Among of various energy conversion and storage devices, supercapacitors also known as electrical capacitors, which display intermediate power and energy between dielectric capacitors and batteries, have attracted particular research attention in recent years due to their high power density and long cycle lifetime. [1-5] Based on the energy storage mechanisms, supercapacitors can be divided into two categories: electric double layer capacitors (EDLCs) and pseudocapacitors. [6] Pseudocapacitors, which store charges from fast and reversible redox reactions at the surface of electroactive materials (MnO_2 , NiCO_2O_4 , conducting polymers), usually faces problems of either short cycling life or poor rate ability, let along their high cost. [7-10] As for EDLCs, the capacitance comes from the reversible ion absorption at the electrode/electrolyte interface. Carbon based materials with high surface area, such as activated carbons (ACs) and mesoporous carbons (MCs), are ideal candidates for EDLCs. ACs are widely used for EDLCs electrode materials because of their extremely high specific surface area (up to $3000 \text{ m}^2 \text{ g}^{-1}$), abundant raw materials, and moderate cost. [11-15] However, the specific capacitances of ACs are usually not so high as expected especially when increasing the charging-discharging rate, which are mainly caused by the large quantity of micropores in ACs that are inaccessible by the electrolyte. For MCs, their relatively regular structure and suitable pore size bring about acceptable capacitances and considerable cycling life, nevertheless the fabrication of MCs usually involves complex or multi steps which are not suitable for mass production and the cost is also very high. [16-23] Despite ACs and MCs, carbon nanotubes and graphene have also been investigated as electrodes for electric double-layer capacitors. However, the

preparation of these materials usually requires exact controlled condition, which mainly limits their practical application. [24-25]

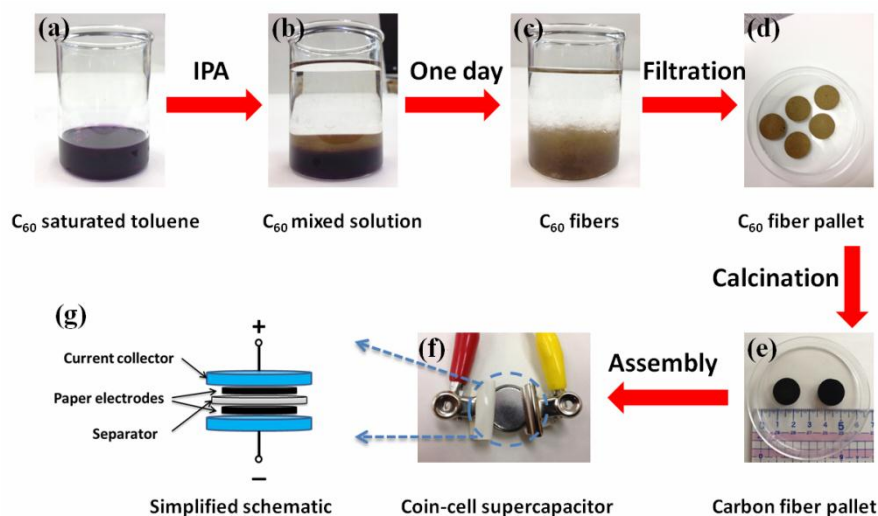


Fig. 7-1 Illustration of preparation process of the highly porous nanofiber paper and its assembly process for coin-cell supercapacitors.

Here, in this study, we report a highly porous carbon nanofiber paper (HPNFP), which possess large external surface area, and use it to fabricate a high energy supercapacitor and also a flexible solid state supercapacitor. As show in Figure 9-1, the HPNFP was prepared by high temperature treatment of the fullerene nanofiber paper. The fullerene nanofibers were firstly prepared by a liquid-liquid interfacial precipitation method. The fullerene nanofibers were then vacuum filtered and cut into small pallet. Then the small fullerene pallet was converted to carbon fiber pallet under high temperature. Then the carbon fiber pallet was directly used as electrodes to assemble coin-cell supercapacitors.

7.2 Experimental section

7.2.1 Fabrication of Highly Porous Carbon Nanofiber Paper (HPNFP)

Fullerene nanofibers were firstly prepared by a liquid-liquid interfacial precipitation method. [26-27] In a typical process, C_{60} saturated toluene suspension was cooled to 5°C in a refrigerator. Then, isopropyl alcohol (IPA) was added dropwise into the suspension. The mixture was kept at 5°C for three days to grow the fullerene nanofibers. The final mixture was filtered on a stainless steel mesh and the fullerene nanofiber paper was peeled off from the mesh. The highly porous carbon nanofiber paper was obtained by heating the fullerene nanofiber paper at 1100°C for 2h at Ar atmosphere.

7.2.2 Characterizations

The morphology of the samples were characterized by SEM (JEOL-6500, 15.0 kV) and TEM (JEOL-2100, 200 kV). The structure was analyzed by powder XRD (Rigaku RINT-2500) and Raman

spectroscopy (Nanophoton RAMAN-11). XPS was obtained on a PHI Quantachrome SXM system with a monochromatic Al K α X-ray source. Nitrogen sorption isotherms were collected using an AUTOSORB iQ-MP instrument. The specific surface areas were determined according to the BET method and the pore size distribution was determined via the NLDFT method using nitrogen adsorption data

7.2.3 Fabrication of a high energy density coin cell supercapacitor with an ionic liquid electrolyte

Coin cells (CR2025) were fabricated using two pieces of HPNFP as electrode materials, a piece of glass fiber as the separator, conductive carbon coated aluminum foils (ExopackTM 0.5 mil 2-side coating) as the current collectors, and 1-Ethyl-3-methylimidazolium tetrafluoroborate (EMIMBF₄) as the electrolyte. The cells were assembled in an argon filled glove box.

7.2.4 Fabrication of a flexible All-Solid-State supercapacitor with an aqueous electrolyte

The all-solid-state supercapacitor was assembled using gold-coated polyethylene terephthalate (PET) sheet as the current collector and flexible substrate, two pieces of HPNFP as electrode materials, poly (vinyl alcohol) PVA-H₂SO₄ gel as the electrolyte and separator. The PVA-H₂SO₄ gel was prepared by mixing 3 g PVA and 3 g H₂SO₄ in 30 mL H₂O. Then the whole mixture was heated at about 85 °C for several hours to form a clear solution

7.2.5 Electrochemical measurements

Cyclic voltammetry (CV), galvanostatic charge-discharge (GC), and electrical impedance spectroscopy (EIS) measurements were performed using a VMP3 multi-potentiostat/galvanostat (Biologic) system. The specific capacitance C was calculated by $C = 2I\Delta t / (m\Delta V)$, where I is the discharge current, Δt is the discharge time, ΔV is the voltage change excluding the IR drop during the discharge process, and m is the mass of a single electrode. The specific energy density E and the specific power density P were calculated using $E = CV^2/8$ and $P = E/t$, respectively, where C is the specific capacitance, V is the voltage of the charged supercapacitor, and t is the discharge time.

7.3 Result and discussion

The morphology of the fullerene nanofibers was examined by SEM and TEM. Figure 7-2a-c show the SEM images in different magnification, from which we can see the fullerene nanofibers are ultra-long ranging from 100 to 1000 μm with a diameter about 300 nm. Besides, the surface of the fullerene nanofibers is rather smooth, and no obvious pores can be seen. TEM images in Figure 8-2d also confirm its non-porous structure.

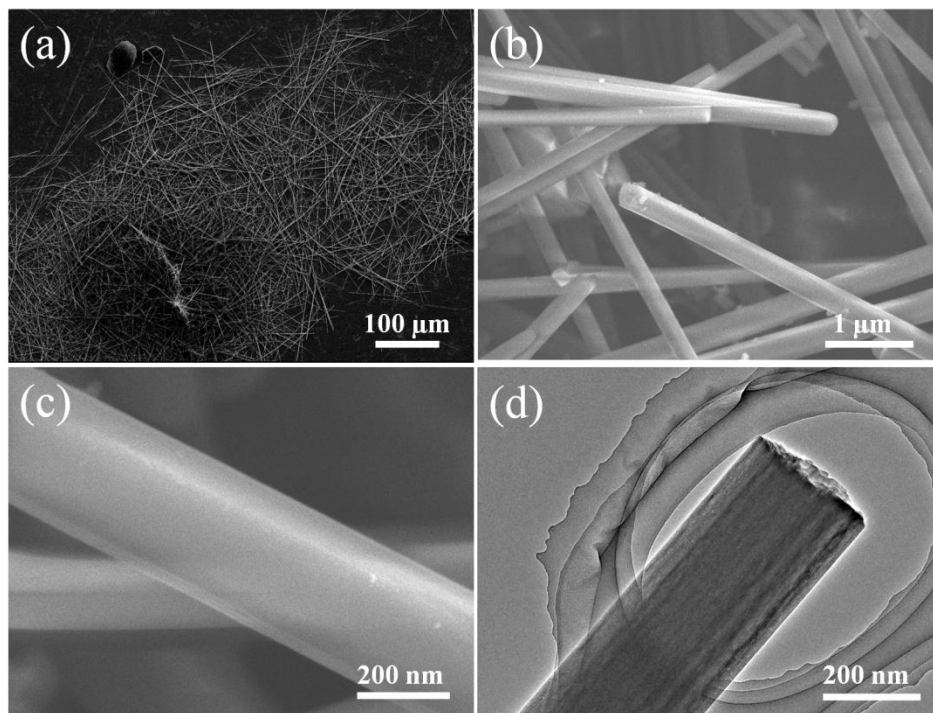


Fig. 7-2 The morphology of as prepared fullerene nanofibers: (a-c) SEM images in different magnification, (d) TEM images showing a single fiber.

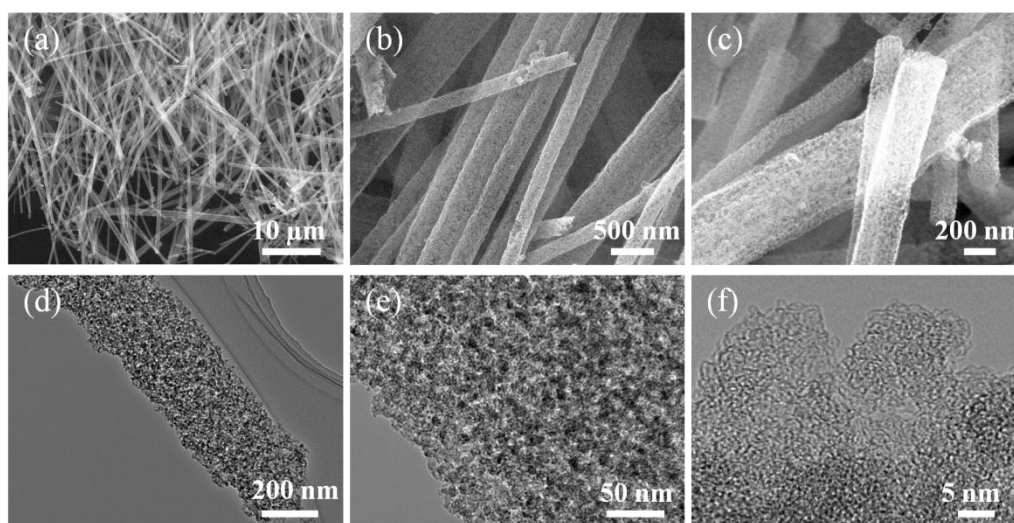


Fig. 7-3 The morphology of as prepared highly porous nanofibers: (a-c) SEM images; (d-f) TEM images in different magnification.

Figure 7-3a-c displays the SEM images of the highly porous nanofiber paper in different magnification. Obviously, there are numerous small mesopores in the fiber, which is totally different from the former fullerene nanofibers. TEM images in Figure 7-3d-e also confirm the ultra-porous structure. The pores are ranging from 5 to 10 nm. This highly porous structure was expected to exhibit high specific surface area thus, providing high specific electric double-layer capacitance.

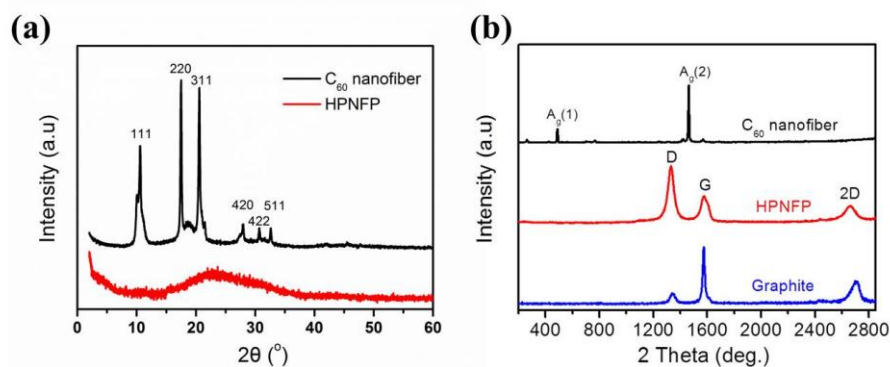


Fig. 7-4 (a) XRD patterns of the fullerene nanofibers and the highly porous nanofibers; (b) FT-Raman spectrum of fullerene nanofibers, highly porous nanofibers, and graphite.

The chemical structure of as prepared highly porous nanofiber was further characterized by XRD and Raman technique. Figure 7-4a shows the XRD pattern of the fullerene nanofiber and the highly porous nanofiber. As can be observed, the characteristic peaks of fullerene nanofiber disappear in the pattern of the highly porous nanofiber, suggesting the fullerene nanofibers have been converted to carbon fibers. The Raman spectrums of the fullerene nanofibers, the highly porous nanofiber, and graphite were displayed in Figure 7-4b, respectively. For the fullerene nanofibers, there are two main peaks at 491 and 1490 cm^{-1} , which are the characteristic peaks of fullerene. The peak at 491 and 1490 cm^{-1} are assigned to the $A_g(1)$ and $A_g(2)$ mode, which are from the breathing mode and the pentagonal pinch mode on the fullerene molecules. [28-29] In the Raman spectra of the highly porous nanofibers, the two peaks from fullerene molecules disappear, and three new peaks appear at 1350 , 1583 , and 2740 cm^{-1} . These three peaks are similar to that of graphite. The changes in the Raman spectrum demonstrate again that the fullerene nanofibers have been turned into graphitic carbon nanofibers. [28-29]

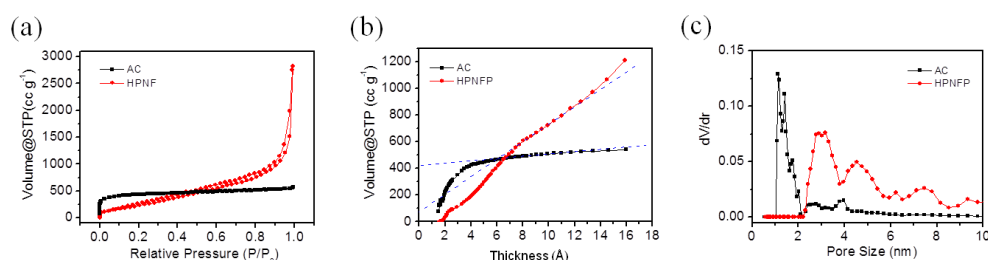


Fig. 7-5 (a) Nitrogen sorption isotherms; (b) t-plot; and (c) pore size distribution of the highly porous nanofibers and activated carbons.

Table 7-1 The specific surface area of activated carbons and highly porous nanofibers.

	S_{BET}	Internal surface area	External surface area
AC	1621.2	1489.9	131.3
HPNFP	1157.7	154.8	1002.9

The porous structure of the highly porous nanofiber was further investigated by nitrogen adsorption-desorption isotherms and the isotherm of activated carbon was also tested for comparison. As can be seen in Figure 7-5a, the two isotherms of activated carbons and highly porous nanofibers exhibit different types of curves, indicating their different pore structures. The isotherms of activated carbon and highly porous nanofiber can be assigned to type-I and type-IV isotherms. The two materials both show very large Brunauer-Emmet-Teller (BET) surface area over 1000 m²/g and the activated carbons even show much a larger value. However, as shown in Table 7-1, the external surface area of the highly porous carbon nanofibers is nearly 8 times larger than activated carbons, which can be confirmed in the pore size distribution in Figure 7-5c where most pores are below 2 nm for activated carbons. This pore structure of the activated carbons was further confirmed using TEM observation shown in Figure 7-6. Such small pores make it is difficult for ions adsorption when using for supercapacitors. As for the as prepared highly porous carbon nanofibers, most pores are larger than 2 nm, which is in good agreement with the TEM observation. This kind of pores would be useful for supercapacitor applications.

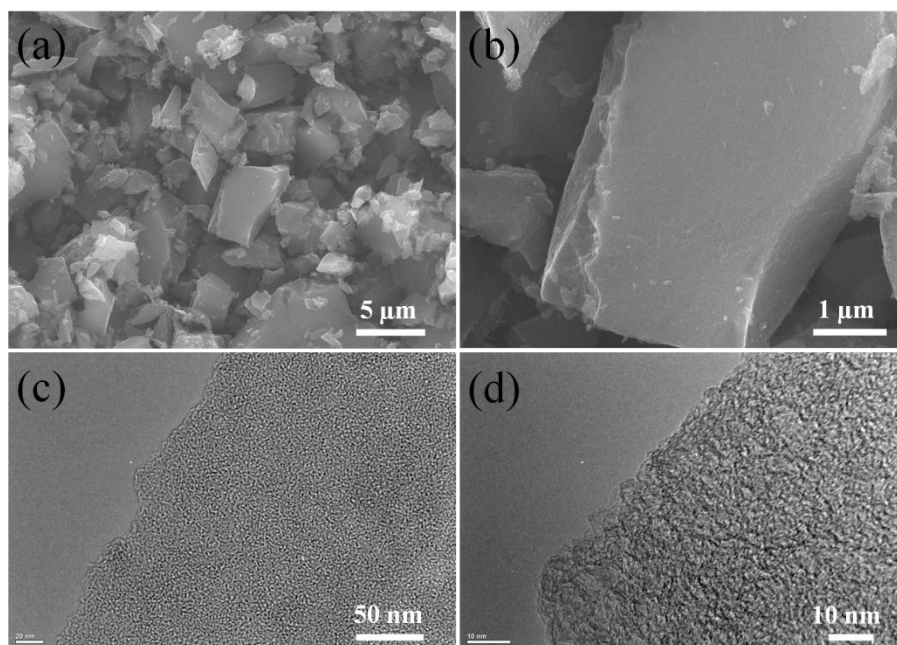


Fig. 7-6 (a,b) SEM images; (c,d) TEM images of activated carbons.

The highly porous nanofiber paper was directly used as electrode for supercapacitors and a room temperature ionic liquid EMI-BF₄ was used as the electrolyte. The supercapacitor performances of the highly porous nanofiber paper are compared with that of activated carbons as shown in Figure 7-7. Figure 7-7a displays the cyclic voltammetry (CV) curves of the highly porous nanofiber paper at

different scanning rates in the potential range of 0-4V. As can be seen, the CV curves are all feature the rectangular loops, indicating that the charge stored in the electrode are dominated by the electrical double-layer mechanism. Figure 7-7b compares the CV curves of the activated carbons and the highly porous nanofiber papers at a high scanning rate of 100 mV/s. Rectangular shaped CV curves can only be maintained for the highly porous nanofiber paper electrodes, indicating its better rate performance. Figure 7-7c and d compare the galvanostatic charge-discharge curves of the two electrodes at the current densities of 0.5 A/g and 10 A/g. Obviously, the highly porous nanofiber paper electrode exhibits negligible IR drop compared with that of activated carbons, which is due to the higher conductivity of the highly porous nanofibers. The calculated specific capacitances under different current densities are presented in Figure 7-7e. At low current density of 0.2 A/g, the highly porous nanofiber paper could deliver a high specific capacitance of 191 F/g, corresponding to a high energy density of 106 Wh/kg, which is two times large than that of activated carbon. In addition, this value is even large than some previously reported mesoporous carbons, carbon nanotubes, and graphene. Figure 7-7f shows the cycling performance of the highly porous nanofiber paper and activated carbons. After 2000 repeated charge-discharge process, 88% of the initial capacitance was maintained for the highly porous nanofiber paper, while the value is only 48% for activated carbons.

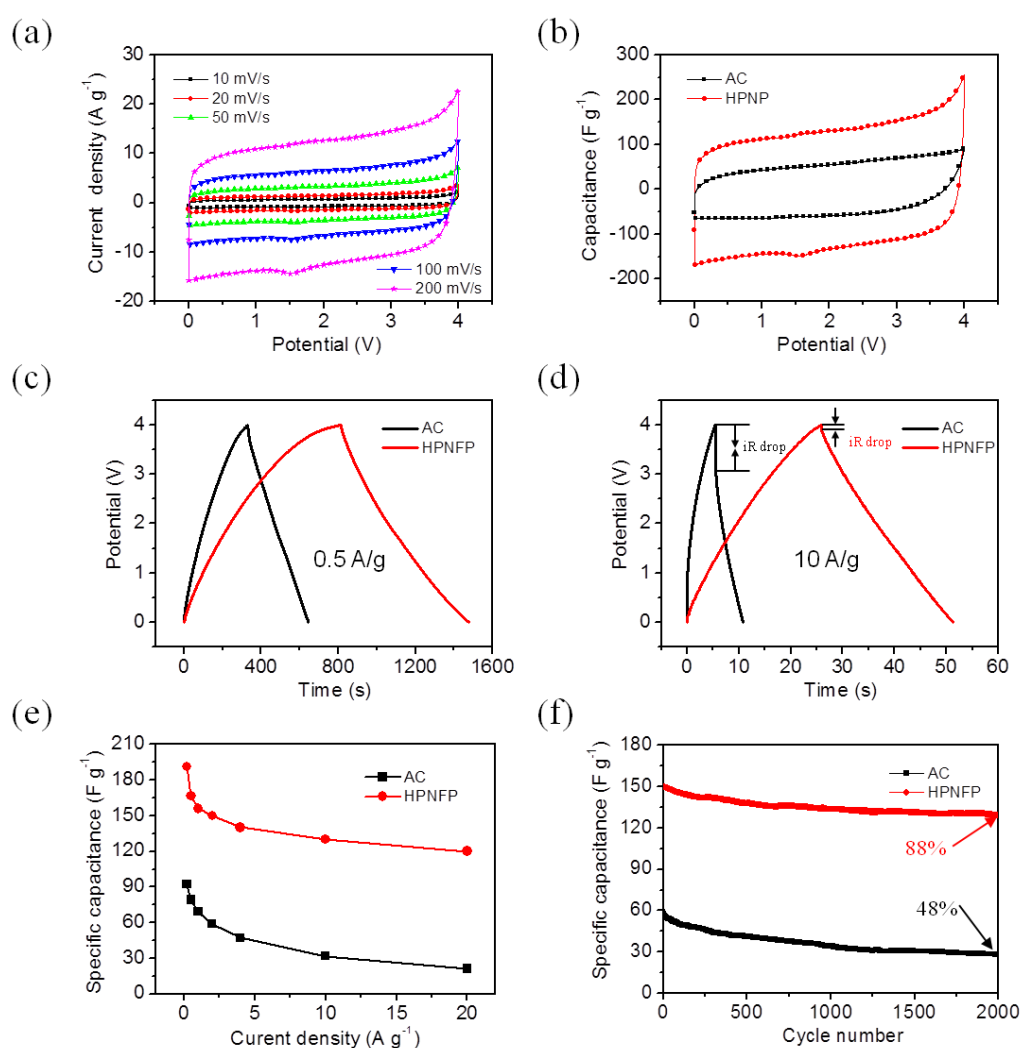


Fig. 7-7 Supercapacitor performances of highly porous nanofibers and activated carbons in ionic liquid electrolyte with a two-electrode cell. (a) CV curves of the highly porous nanofibers at different scanning rates; (b) CV curves of the two materials obtained at slow and fast scan rates; (c,d) Charge/discharge curves obtained at different current densities; (e) Gravimetric capacitances measured at various charge/discharge current densities; (f) Cycling performances.

In order to fully understand the better electrochemical performances of the highly porous nanofiber paper electrode, electrochemical impedance spectroscopy (EIS) was performed to test the electrochemical resistance of the two materials. In the Nyquist plot as shown in Figure 7-8a, activated carbons show obvious Warburg region, indicating its longer ions transport time. Besides, as shown in Figure 7-8b, the frequency response time of highly porous nanofibers (0.34s) is 1 tenth of activated carbons (3.57s), which means ion transfer into the pores of HPNFP is easier than AC. The reasons for the shorter response time could be explained in BET result. In the BET result, the pores in activated carbons are 1-2nm, and pores in highly porous nanofibers are 3-8nm. The larger pore size of HPNFP benefits ions transport. The longer response time of AC indicates there is difficulty for ions transfer into pores of AC, which result in a low capacitance.

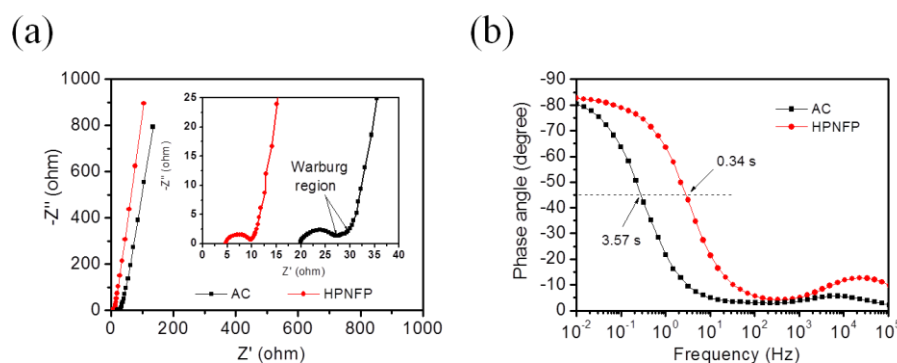


Fig. 7-8 (a) Nyquist plots of the two electrodes. The inset shows an expanded view for the high frequency. (b) Frequency response of the two electrodes.

The highly porous nanofiber papers were further used to fabricate a flexible all-solid-state supercapacitor. As shown in Figure 7-9, gold coated PET was used as the current collector, a solid state gel was used as the electrolyte. As shown in figure b, the capacitance remains almost the same when it was bended under different angles, indicating its good stability. The maximum capacitance of the flexible supercapacitor is 228 F/g. Besides, this solid state supercapacitor also exhibit excellent cycling stability with 93.5% retention after 8000 cycles. The inset figure in Figure 7-9e shows that a LED display board can be lighted by three series of the solid state supercapacitors, indicating the practical application of the solid state supercapacitors.

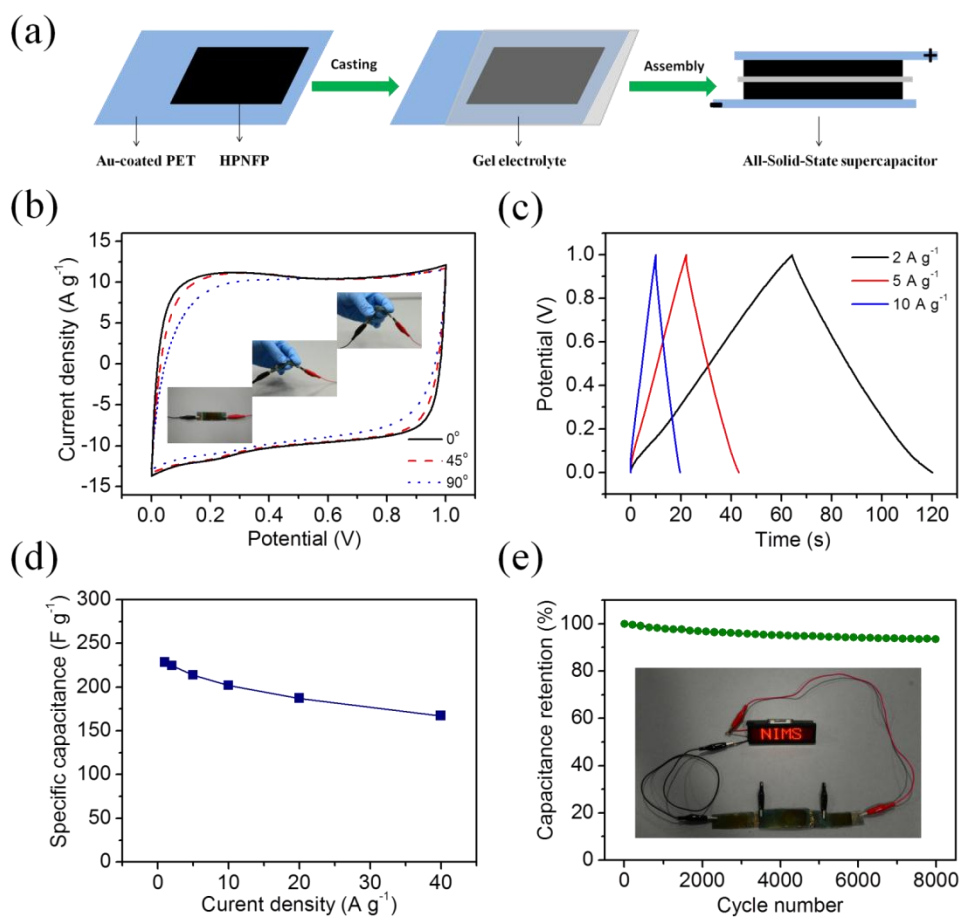


Fig. 7-9 (a) The fabrication process of the solid state supercapacitor based on the highly porous nanofiber paper; (b) CV curves of the electrode at different bending degree; (c) Charge/discharge curves obtained at different current densities; (e) Gravimetric capacitances measured at various charge/discharge current densities; (f) Cycling performances.

7.4 Conclusion

In summary, a highly porous nanofibers paper was prepared by carbonization of C_{60} nanofibers, and the highly porous nanofibers paper shows a large external specific surface area of $1003 \text{ m}^2/\text{g}$. The highly porous nanofibers paper based supercapacitors can deliver a high capacitance of 191 F/g , high energy density of 106 Wh/kg in ionic liquid electrolyte. A flexible all-solid-state supercapacitor fabricated based on the highly porous nanofibers paper exhibits a large specific capacitance of 228 F/g and good flexibility.

References

1. P. Simon and Y. Gogotsi, *Nature materials*, 2008, **7**, 845-854.
2. A. Ghosh and Y. H. Lee, *ChemSusChem*, 2012, **5**, 480-499.
3. X. Lu, M. Yu, G. Wang, Y. Tong and Y. Li, *Energy & Environmental Science*, 2014, **7**, 2160.
4. J. Wang and S. Kaskel, *Journal of Materials Chemistry*, 2012, **22**, 23710.

5. S. Guo and S. Dong, *Chemical Society reviews*, 2011, **40**, 2644-2672.
6. Y. B. Tan and J.-M. Lee, *Journal of Materials Chemistry A*, 2013, **1**, 14814.
7. B. Cui, H. Lin, J.-B. Li, X. Li, J. Yang and J. Tao, *Advanced Functional Materials*, 2008, **18**, 1440-1447.
8. Q. Wang, B. Liu, X. Wang, S. Ran, L. Wang, D. Chen and G. Shen, *Journal of Materials Chemistry*, 2012, **22**, 21647.
9. G. Zhang and X. W. David Lou, *Scientific reports*, 2013, **3**, 1470.
10. H. Wang, Q. Gao and L. Jiang, *Small*, 2011, **7**, 2454-2459.
11. G. Wang, H. Wang, X. Lu, Y. Ling, M. Yu, T. Zhai, Y. Tong and Y. Li, *Advanced materials*, 2014, **26**, 2676-2682, 2615.
12. X. Tao, J. Du, Y. Li, Y. Yang, Z. Fan, Y. Gan, H. Huang, W. Zhang, L. Dong and X. Li, *Advanced Energy Materials*, 2011, **1**, 534-539.
13. Q. Zhang, J. Rong, D. Ma and B. Wei, *Energy & Environmental Science*, 2011, **4**, 2152.
14. G. Milczarek, A. Ciszewski and I. Stepniak, *Journal of Power Sources*, 2011, **196**, 7882-7885.
15. C.-L. Liu, W. Dong, G. Cao, J. Song, L. Liu and Y. Yang, *Journal of The Electrochemical Society*, 2008, **155**, F1.
16. D. Feng, Y. Lv, Z. Wu, Y. Dou, L. Han, Z. Sun, Y. Xia, G. Zheng and D. Zhao, *Journal of the American Chemical Society*, 2011, **133**, 15148-15156.
17. H. Jiang, L. Yang, C. Li, C. Yan, P. S. Lee and J. Ma, *Energy & Environmental Science*, 2011, **4**, 1813.
18. S. Murali, D. R. Dreyer, P. Valle-Vigon, M. D. Stoller, Y. Zhu, C. Morales, A. B. Fuertes, C. W. Bielawski and R. S. Ruoff, *Physical chemistry chemical physics : PCCP*, 2011, **13**, 2652-2655.
19. M. Li, J. Ding and J. Xue, *Journal of Materials Chemistry A*, 2013, **1**, 7469.
20. C.-W. Huang, C.-H. Hsu, P.-L. Kuo, C.-T. Hsieh and H. Teng, *Carbon*, 2011, **49**, 895-903.
21. J. Zhou, J. He, C. Zhang, T. Wang, D. Sun, Z. Di and D. Wang, *Materials Characterization*, 2010, **61**, 31-38.
22. W. Li, F. Zhang, Y. Dou, Z. Wu, H. Liu, X. Qian, D. Gu, Y. Xia, B. Tu and D. Zhao, *Advanced Energy Materials*, 2011, **1**, 382-386.
23. K. Wilgosz, X. Chen, K. Kierzek, J. Machnikowski, R. J. Kalenczuk and E. Mijowska, *Nanoscale research letters*, 2012, **7**, 269.
24. D. A. C. Brownson, D. K. Kampouris and C. E. Banks, *Journal of Power Sources*, 2011, **196**, 4873-4885.
25. Y. Huang, J. Liang and Y. Chen, *Small*, 2012, **8**, 1805-1834.
26. J.-i. Minato and K. i. Miyazawa, *Diamond and Related Materials*, 2006, **15**, 1151-1154.
27. K. i. Miyazawa, J.-i. Minato, T. Yoshii, M. Fujino and T. Suga, *Journal of Materials Research*, 2011, **20**, 688-695.
28. M. Tachibana, K. Kobayashi, T. Uchida, K. Kojima, M. Tanimura and K. Miyazawa, *Chemical Physics Letters*, 2003, **374**, 279-285.
29. C. L. Ringor and K. Miyazawa, *Diamond and Related Materials*, 2008, **17**, 529-534.

Chapter 8

Hierarchical NiCo₂O₄ Nanocubes Constructed by Nanosheets with Excellent Pseudo-capative Properties

8.1 Introduction

Recently, the demand for high power energy storage systems has increased sharply due to the emergence of various kinds of portable electronic devices. Electrochemical capacitors, also known as supercapacitors, has attracted intense attention all over the world due to its higher power density and better long cycling stability than Li-ions batteries. [1-5] However, the practical application of supercapacitor is mainly hindered by their low energy density and low specific capacitance. Carbon based materials are widely used as the electrode materials for supercapacitors because of their high specific surface and low cost. [6-15] However, these carbon based materials usually exhibit low specific capacitance due to their intrinsic charge storage mechanism where the energy storage comes from the reversible adsorption of electrolyte ions at the electrode/electrolyte interfaces. In this case, many attentions have been paid to another type of supercapacitor, pseudo-capacitor, which store energy by the surface redox reactions with the electrolyte and the resulted pseudo-capacitance is usually much larger than the electric double-layer capacitance from carbon based electrodes.

Transition metal oxides with multiple oxidation states have been regarded as ideal electrode materials for pseudo-capacitors. NiO, Co₃O₄, MnO₂, Ni(OH)₂, Co(OH)₂ have been intensely studied for pseudo-capacitors. [16-19] Recently, mixed-metal oxide such as NiCo₂O₄ has also been investigated for potential application in supercapacitors. Compared with NiO and Co₃O₄, the conductivity of NiCo₂O₄ is at least 2 orders of magnitude higher, which make it exhibit better cycling stability when it is used for supercapacitor application. [20-22] Various nanostructured NiCo₂O₄, such as nanowires, nanorods, nanotubes, or nanospheres have been reported with enhanced pseudo-capacitance. NiCo₂O₄ nanocubes have not been investigated, and its unique structure should result in good electrochemical properties. Here, for the first time, we have prepared NiCo₂O₄ nanocubes using Cu₂O nanoboxes as the template and investigate its potential application for pseudo-

capacitors. Electrochemical measurements show that the as prepared hierarchical NiCo₂O₄ nanocubes can deliver a high specific capacitance of 930 F/g and excellent cycling stability with 88% retention after 2000 cycles, demonstrating its great potential as electrode materials high performance pseudo-capacitors.

8.2 Experimental section

8.2.1 Synthesis of Cu₂O nanocubes

Firstly, 10 mL of 2 M NaOH was added into 100 mL of 0.001 M CuCl₂•2H₂O solution. The mixture was stirred for 0.5 h and the color turned into brown. Then, 10 mL of 0.6 M ascorbic acid solution was added dropwise into the mixture and the system is transfer to a 50°C water bath. The reaction was stirred for 3h before it was cooled to the room temperature. The product was collected and washed by centrifugation with distilled and ethanol, and finally dried in an oven overnight.

8.2.2 Synthesis of hierarchical NiCo₂O₄ nanocubes

The hierarchical NiCo₂O₄ nanocubes were prepared by using Cu₂O nanocubes as the templates. In a typical process, 10 mg of Cu₂O template was mixed with a certain amount of Ni(NO₃)₂•6H₂O and Co(NO₃)₂•6H₂O in a mixed water/ethanol solution, and the ratio of Ni(NO₃)₂•6H₂O and Co(NO₃)₂•6H₂O is fixed as 1:2. 0.5 g of PVP was added into the mixture to fully disperse the Cu₂O templates. After stirring for 0.5 h, 4 mL of 1 M Na₂S₂O₃ aqueous solution was added dropwise into the mixture. After the reaction of 3 h, the product was centrifuged with deionized water for several time and dried in an oven overnight. Then, the precursor was annealed at 200°C for 3 h in air and finally the NiCo₂O₄ nanocubes were obtained.

8.2.3 Structural characterization

The morphology and structure of samples were investigated by field emission scanning electron microscopy (FESEM) (JEOL, JSM-7001F), transmission electron microscopy (TEM) (JEOL, JEM-2100). X-ray diffraction (XRD) pattern was collected on a Rigaku RINT 2500. X-ray photoelectron spectroscopy (XPS) data were obtained by an PHI Quantera SXM (Ultravac-PHI). The BET surface area was probed by using an AUTOSORB iQ-MP instrument.

8.2.4 Electrochemical characterization

A three-electrode test system was used to test the electrochemical performance of the as prepared hierarchical NiCo₂O₄ nanocubes. The working electrode was prepared by pressing a mixture of the as prepared hierarchical NiCo₂O₄ nanocubes, carbon black, and polytetrafluoroethylene (PTFE) binder with a weight ratio of 80:10:10 onto a porous nickel foam current collector. The electrode was dried in an oven at 80°C overnight before use. A Pt foil was used as the counter electrode and standard calomel electrode (SCE) was used as the reference electrode. The electrochemical

measurements were conducted in a 5 M KOH electrolyte. Cyclic voltammograms and galvanostatic charge-discharge were performed on a VMP3 electrochemical station (Biologic).

8.3 Results and discussion

The morphology of the as prepared Cu_2O templates is shown in Figure 8-1. Figure 8-1a-c shows the SEM images of the Cu_2O templates at different magnification. As can be seen in Figure 8-1a, the Cu_2O templates display a typical cube-like morphology and the cubes are uniform and monodispersed. Figure 8-1b and c show the SEM images in higher magnification, from which we can observe that the side length of Cu_2O nanocube is about 400-500 nm and the surface of the cubes is rather smooth. TEM image in Figure 8-1d also confirms the cube-like structure of as prepared Cu_2O template. Besides, TEM observation further reveals the solid structure of the Cu_2O nanocubes.

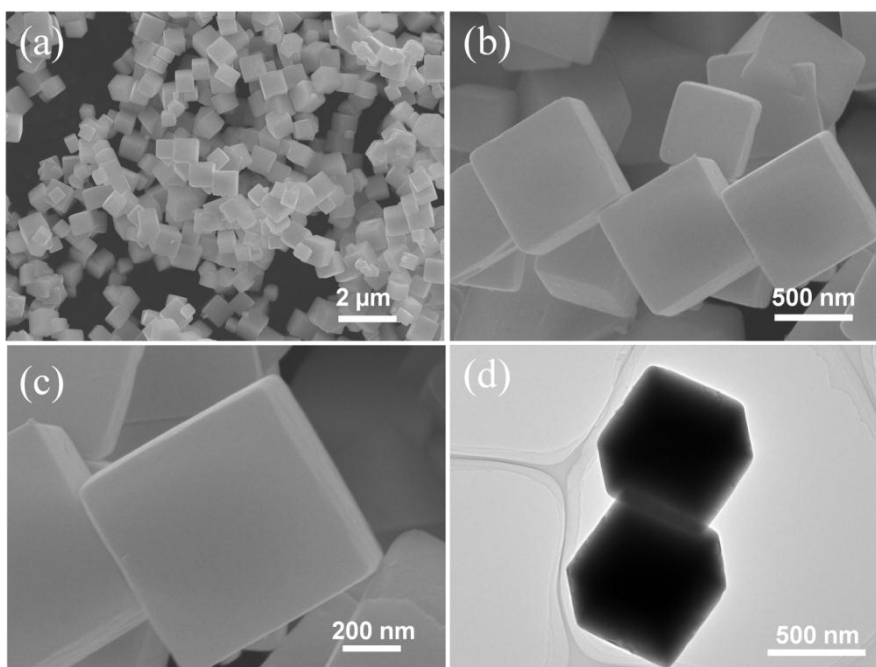


Fig. 8-1 The morphology of as prepared Cu_2O templates: (a-c) SEM images in different magnification, (d) TEM images.

Figure 8-2 shows the SEM images of the as prepared NiCo_2O_4 samples at different magnification. As can be observed, the NiCo_2O_4 maintain the typical cube structure. In addition, the NiCo_2O_4 nanocubes are constructed by numerous nanosheets. It is highly expected that this unique structure would bring about a high specific surface area due to the hierarchical nanosheets and the good morphology stability and consequently, could result in a high specific capacitance for pseudo-capacitors because of the easy access to the active materials for redox reactions.

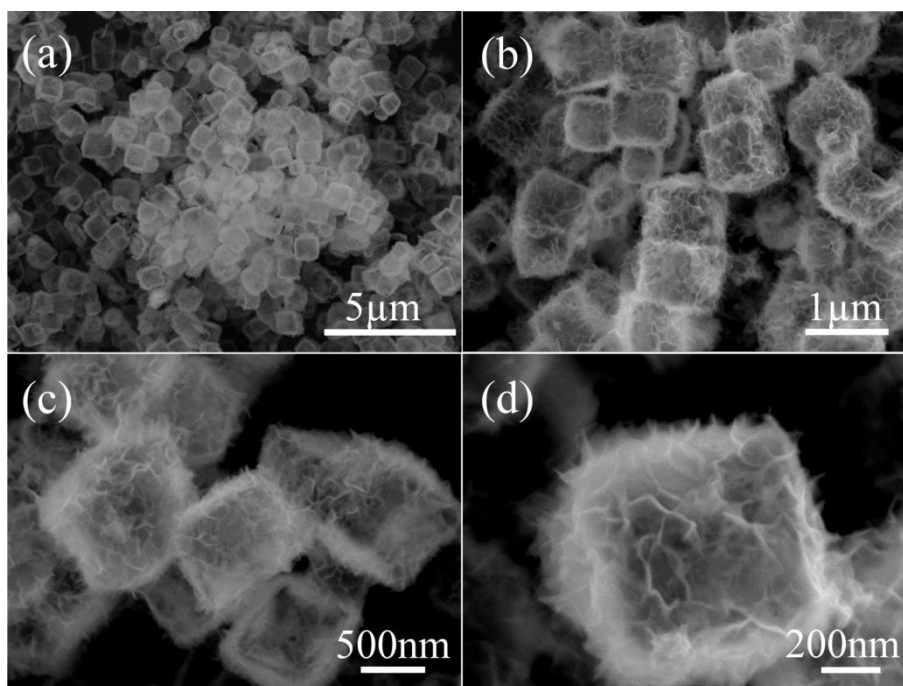


Fig. 8-2 SEM images of the as prepared hierarchical NiCo₂O₄ nanocubes in different magnification.

TEM, HRTEM, and selected-area electron diffraction (SAED) are applied to further characterize the morphology and structure of the as prepared NiCo₂O₄ materials. Figure 8-3a and b display the representative TEM images of the NiCo₂O₄ materials, showing the cubes are composed of numerous nanosheets, which is in good agreement with the SEM observation. More details of the nanosheets are shown in Figure 8-3c and d. The nanosheets of NiCo₂O₄ display a porous structure with a thickness of 5 to 8 nm. The SAED pattern shown in the inset of 8-3c confirms its polycrystalline nature. The inset figure in Figure 8-3d is an HRTEM image taken from an individual NiCo₂O₄ sheet. The clearly resolved lattice fringe is calculated to be 0.24 nm, which is corresponding to the (311) planes of spinel structured NiCo₂O₄. [23-24]

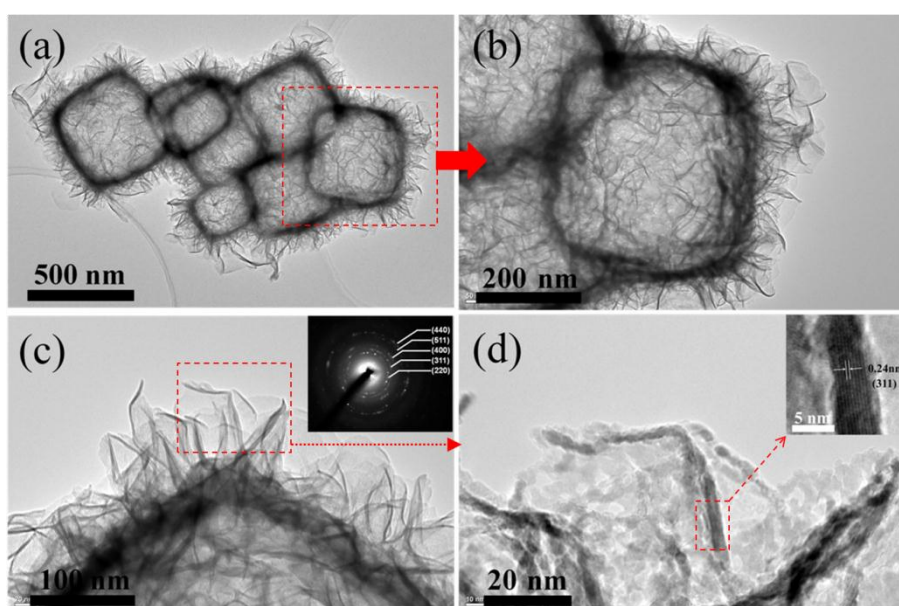


Fig. 8-3 TEM images of the as prepared hierarchical NiCo_2O_4 nanocubes in different magnification.

The phase of as prepared NiCo_2O_4 materials is further confirmed by XRD and the corresponding XRD pattern is shown in Figure 8-4. All the peaks in the XRD pattern can be well indexed into the pure phase of NiCo_2O_4 (JCPDS card number: 20-0781). [25-26] No other peaks were detected, indicating the formation of pure phase NiCo_2O_4 product.

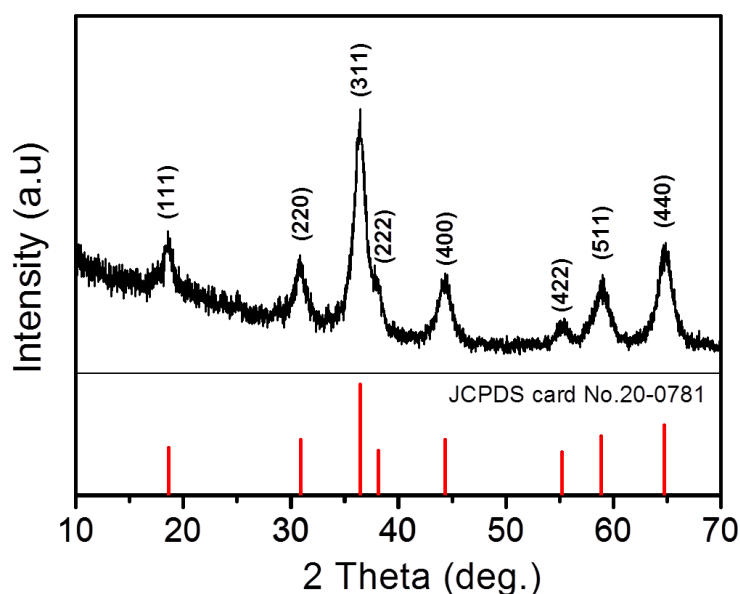


Fig. 8-4 XRD pattern of the as prepared hierarchical NiCo_2O_4 nanocubes.

In order to better understand the chemical bonding states of the Ni and Co element in the hierarchical NiCo_2O_4 nanocubes, X-ray photoelectron spectroscopy (XPS) was conducted. Figure 8-5a displays the XPS survey spectra of the hierarchical NiCo_2O_4 nanocubes. Only the characteristic peaks for Ni, Co, O, and C elements are detected. The existence of C element may be due to the exposure of the sample in air and the C1s peak at 284.6 eV was used as the reference for calibration. Figure 8-5b shows the high-resolution Ni 2p spectrum. There are two strong peaks located at 872.7 and 855.3 eV corresponding to Ni 2p_{1/2}, and Ni 2p_{3/2}, and they are computer fitted to the characteristic peak of Ni²⁺ and Ni³⁺. [24] As can be observed in the fitted result, the Ni element in the NiCo_2O_4 nanocubes sample displays mixed 2 and 3 valence. Similar approach was also applied to Co 2p spectrum as shown in Figure 8-5c. The Co element in the NiCo_2O_4 nanocubes sample also displays mixed 2 and 3 valence. Figure 8-5d shows the core level spectra of O1s region, in which three peaks at 529.5, 531.1, and 532.7 eV are fitted. The O1s peak at 529.5 eV comes from the metal-oxygen

bonds in NiCo₂O₄. The O1s peak at 531.1 eV is from the adsorbed water, and the O1s peak at 531.1 eV is associated with the defect oxygen.

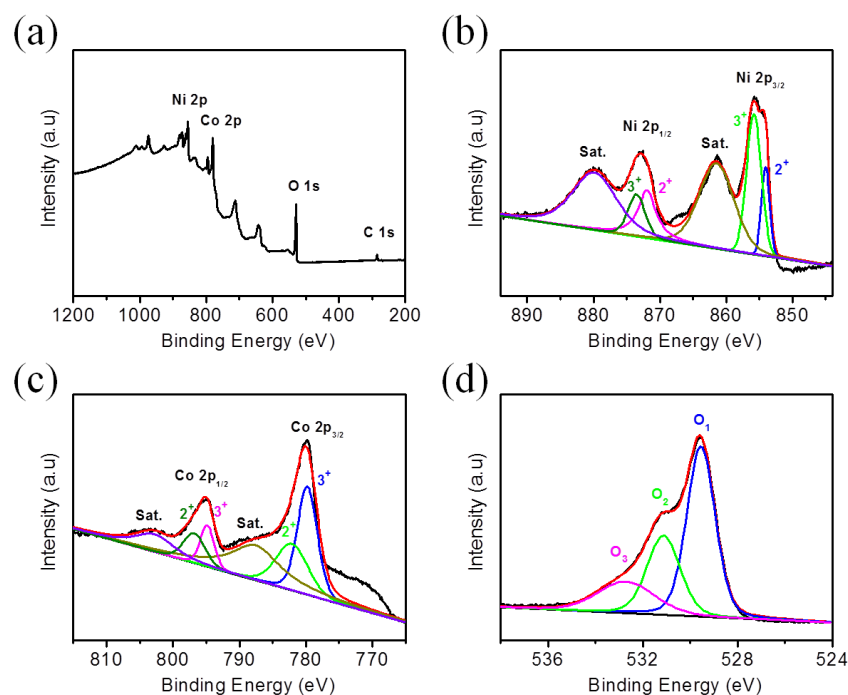


Fig. 8-5 (a) XPS survey spectrum of the as prepared hierarchical NiCo₂O₄ nanocubes; high resolution XPS spectra of (b) Ni 2p, (c) Co 2p, and (d) O 1s.

The porous structure of as prepared NiCo₂O₄ nanocubes was further characterized by nitrogen adsorption-desorption isotherms. Figure 8-6 shows the adsorption-desorption isotherm of the NiCo₂O₄ nanocubes. As can be seen, the curve can be assigned to type-IV isotherms with hysteresis loops. The Brunauer-Emmet-Teller (BET) surface area of as prepared NiCo₂O₄ nanocubes is calculated to be 89m²/g, which is larger than that of previously reported NiCo₂O₄ nanowires, nanoplates, or nanospheres. [20,25,28] The larger specific surface area should be due to its hierarchical porous structure. Besides, the pore size distribution curve calculated by Barrett-Joyner-Halenda (BJH) method is shown in the inset of Figure 8-6. As can be observed, not only small mesopores (<10 nm), but also large mesopores (>10nm) lie in the NiCo₂O₄ nanocubes, which would provide easy access for the electrolyte ions to the surface of the electrode to generate surface redox reactions.

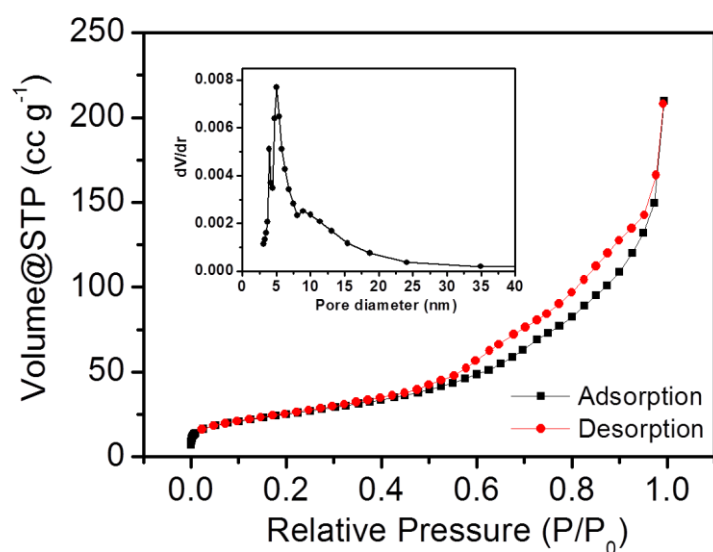


Fig. 8-6 Nitrogen sorption isotherms of the as prepared hierarchical NiCo₂O₄ nanocubes and the inset is pore size distribution.

To understand the formation mechanism of the NiCo₂O₄ nanocubes, time-dependent experiments were performed. Figure 8-7a-c shows the TEM images of the NiCo₂O₄ precursor taken from the reaction at 0, 30, 60, and 120 min, respectively. After a reaction time for 30 min, the nanosheets constructed nanocubes have been formed, and the inner Cu₂O template is still a big block. When the reaction time reaches 60 min, the Cu₂O templates continue to become smaller. After 120 min, the decomposition of Cu₂O templates has been finished and the NiCo₂O₄ nanocubes are finally obtained. There would be two reactions for Na₂S₂O₃, i.e., reaction with Cu₂O or being hydrolyzed to produce hydroxyl which then reacts with Ni²⁺ to generate NiCo₂O₄ precursor. So based on the phenomenon observed in the TEM results, the second reaction should be faster than the first reaction, where the cube shell was formed before Cu₂O was dissolved.

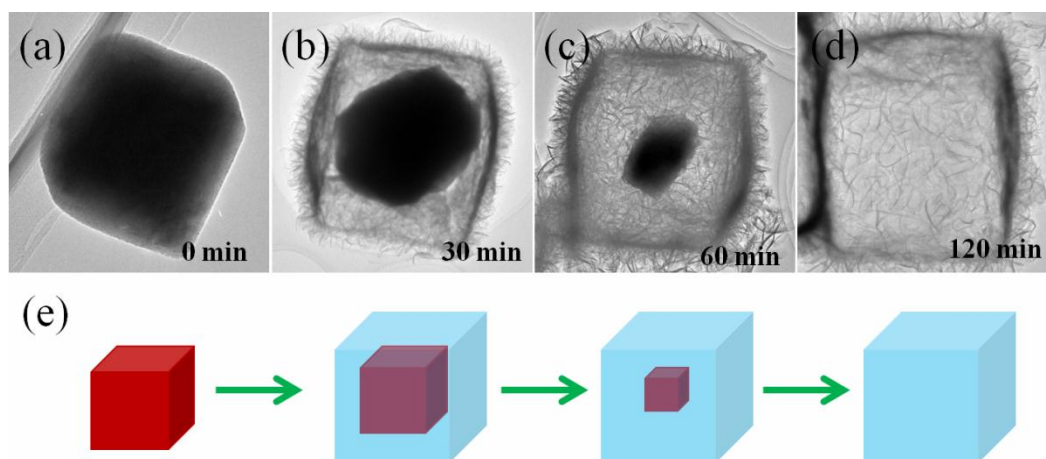


Fig. 8-7 (a-d) TEM images of the NiCo₂O₄ precursor taken from the reaction at 0, 30, 60, and 120 min, respectively. (e) Schematic illustration of the morphology evolution of the NiCo₂O₄ precursor.

The electrochemical performances of the as prepared NiCo₂O₄ nanocubes are measured by cyclic voltammetry (CV) and galvanostatic charge-discharge methods. Figure 8-8a shows the CV curves of the as prepared NiCo₂O₄ nanocubes at different scanning rates from 1 to 5 m V/s in the voltage range of -0.1 to 0.5 V in 5M KOH electrolyte. Two main peaks can be observed in the anodic and cathodic CV curves, suggesting the existence of redox reactions. The redox reactions should be assigned to the solid state redox couples of Co³⁺/Co²⁺ and Ni³⁺/Ni²⁺. However, there is only one pair of redox peaks though the existence of two redox couples, which may be due to the close redox potential of Co³⁺/Co²⁺ and Ni³⁺/Ni²⁺. All the CV curves show similar shape and the current rise with the increasing scanning rates, indicating the good stability of the electrode.

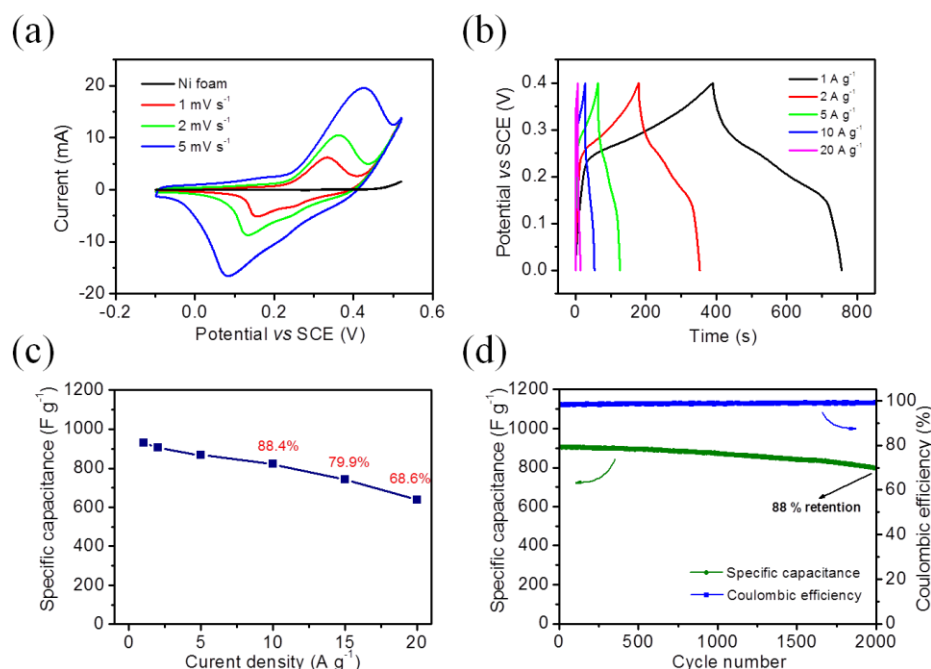


Fig. 8-7 Supercapacitor performances of the hierarchical NiCo₂O₄ nanocube electrode. (a) CV curves obtained at different scan rates; (b) Charge/discharge curves obtained at different current densities ranging from 1 to 20 A/g; (c) Gravimetric capacitances measured at various charge/discharge current densities; (d) Cycling performances.

Figure 8-8b depicts the discharge curves of the NiCo₂O₄ nanocube electrode at different current densities ranging from 1 to 20 A/g. As can be clearly seen, the discharge curves are not linear shaped like the former electric double-layer capacitors, which further confirms its pseudo-capacitance from the surface redox reactions. The calculated specific capacitances under different current densities are shown in Figure 8-8c. At a low current density of 1 A/g, the NiCo₂O₄ nanocube electrode could deliver a highest specific capacitance of 930 F/g. More importantly, the rate capability of the NiCo₂O₄ nanocube electrode is even more impressive. At a high current density of 10 A/g, a high

specific capacitance of 821 F/g can be obtained, corresponding to 88.4% of the highest value. Even under an extremely high current density of 20 A/g, a high retention of 68.6% was achieved. This kind of rate capability is much better than previously reported NiCo₂O₄ nanowires, nanoplates, or nanospheres. [20,25,28] In addition, the NiCo₂O₄ nanocube electrodes also show excellent cycling performance. After being charged and discharged at a current density of 2 A/g, 88% of its initial capacitance can be maintained. Considering the high specific capacitance, impressive rate capability, and the excellent cycling performance, the NiCo₂O₄ nanocubes hold great potential as electrode materials for high performance pseudo-capacitors.

8.4 Conclusion

In summary, a unique hierarchical NiCo₂O₄ nanocubes constructed by nanosheets have been fabricated by a template method. The hierarchical structure results in a large specific surface area and favourable pore structures. When it was used as electrode materials for supercapacitors, the NiCo₂O₄ nanocube electrodes exhibit many desirable properties, such as high specific capacitance, impressive rate capability, and excellent cycling performance, demonstrating its great potential for the application in pseudo-capacitors.

References

1. P. Simon and Y. Gogotsi, *Nature materials*, 2008, 7, 845-854.
2. M. F. El-Kady, V. Strong, S. Dubin and R. B. Kaner, *Science*, 2012, 335, 1326-1330.
3. Y. Zhu, S. Murali, M. D. Stoller, K. J. Ganesh, W. Cai, P. J. Ferreira, A. Pirkle, R. M. Wallace, K. A. Cychosz, M. Thommes, D. Su, E. A. Stach and R. S. Ruoff, *Science*, 2011, 332, 1537-1541.
4. A. L. Mohana Reddy, S. R. Gowda, M. M. Shaijumon and P. M. Ajayan, *Advanced materials*, 2012, 24, 5045-5064.
5. G. Wang, L. Zhang and J. Zhang, *Chemical Society reviews*, 2012, 41, 797-828.
6. H. Nishihara and T. Kyotani, *Advanced materials*, 2012, 24, 4473-4498.
7. H. Jiang, P. S. Lee and C. Li, *Energy & Environmental Science*, 2013, 6, 41.
8. J. Wang and S. Kaskel, *Journal of Materials Chemistry*, 2012, 22, 23710.
9. L. L. Zhang, R. Zhou and X. S. Zhao, *Journal of Materials Chemistry*, 2010, 20, 5983.
10. Y. B. Tan and J.-M. Lee, *Journal of Materials Chemistry A*, 2013, 1, 14814.
11. X.-L. Wu and A.-W. Xu, *Journal of Materials Chemistry A*, 2014, 2, 4852.
12. D. A. C. Brownson, D. K. Kampouris and C. E. Banks, *Journal of Power Sources*, 2011, 196, 4873-4885.
13. M. Inagaki, H. Konno and O. Tanaike, *Journal of Power Sources*, 2010, 195, 7880-7903.
14. L. Borchardt, M. Oschatz and S. Kaskel, *Materials Horizons*, 2014, 1, 157.
15. Z.-S. Wu, G. Zhou, L.-C. Yin, W. Ren, F. Li and H.-M. Cheng, *Nano Energy*, 2012, 1, 107-131.
16. H. Gao, F. Xiao, C. B. Ching and H. Duan, *ACS applied materials & interfaces*, 2012, 4, 2801-2810.

17. L. F. Chen, Z. H. Huang, H. W. Liang, Q. F. Guan and S. H. Yu, *Advanced materials*, 2013, 25, 4746-4752.
18. G. Yu, L. Hu, M. Vosgueritchian, H. Wang, X. Xie, J. R. McDonough, X. Cui, Y. Cui and Z. Bao, *Nano letters*, 2011, 11, 2905-2911.
19. S. Xiong, C. Yuan, X. Zhang, B. Xi and Y. Qian, *Chemistry*, 2009, 15, 5320-5326.
20. X. Y. Yu, X. Z. Yao, T. Luo, Y. Jia, J. H. Liu and X. J. Huang, *ACS applied materials & interfaces*, 2014, 6, 3689-3695.
21. B. Cui, H. Lin, J.-B. Li, X. Li, J. Yang and J. Tao, *Advanced Functional Materials*, 2008, 18, 1440-1447.
22. L. Hu, L. Wu, M. Liao, X. Hu and X. Fang, *Advanced Functional Materials*, 2012, 22, 998-1004.
23. C. Yuan, J. Li, L. Hou, X. Zhang, L. Shen and X. W. D. Lou, *Advanced Functional Materials*, 2012, 22, 4592-4597.
24. J. Pu, J. Wang, X. Jin, F. Cui, E. Sheng and Z. Wang, *Electrochimica Acta*, 2013, 106, 226-234.
25. Q. Wang, B. Liu, X. Wang, S. Ran, L. Wang, D. Chen and G. Shen, *Journal of Materials Chemistry*, 2012, 22, 21647.
26. M. Cabo, E. Pellicer, E. Rossinyol, P. Solsona, O. Castell, S. Suriñach and M. D. Baró, *Journal of Nanoparticle Research*, 2011, 13, 3671-3681.
27. X. Lu, X. Huang, S. Xie, T. Zhai, C. Wang, P. Zhang, M. Yu, W. Li, C. Liang and Y. Tong, *Journal of Materials Chemistry*, 2012, 22, 13357.
28. Y. Lei, J. Li, Y. Wang, L. Gu, Y. Chang, H. Yuan and D. Xiao, *ACS applied materials & interfaces*, 2014, 6, 1773-1780.

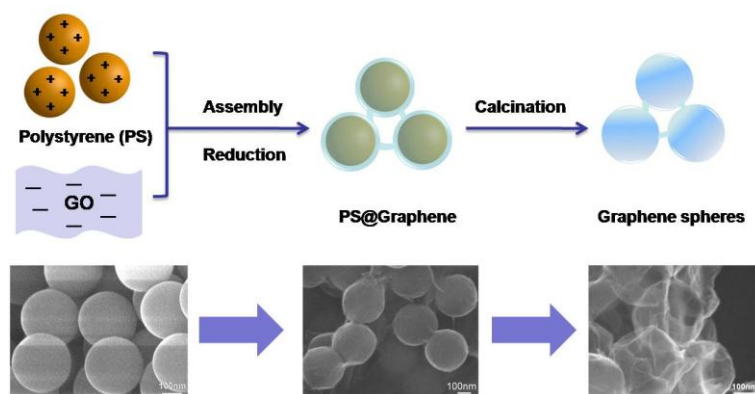
Chapter 9

Conclusions and Perspective

Graphene have been considered as promising electrode materials for application in supercapacitors. The electrochemical performances are largely depended on its morphology and structure. In this thesis, we have developed a series of graphene electrodes with different micro-structures and architectures. These rational designed graphene structures show many advantages, i.e., large specific effective surface area, favorable pore structure, short electron and ion transport path, high conductivity, or better compatibility between electrode and electrolytes, when they are used for supercapacitor applications. Besides, some other novel electrode materials beyond graphene have also designed and fabricated, including SnO₂/graphene composite for Li-ion battery, highly porous carbon nanofiber paper for flexible solid-state supercapacitor, and hierarchical NiCo₂O₄ nanocubes for pseudo-capacitor.

9.1 Conclusions

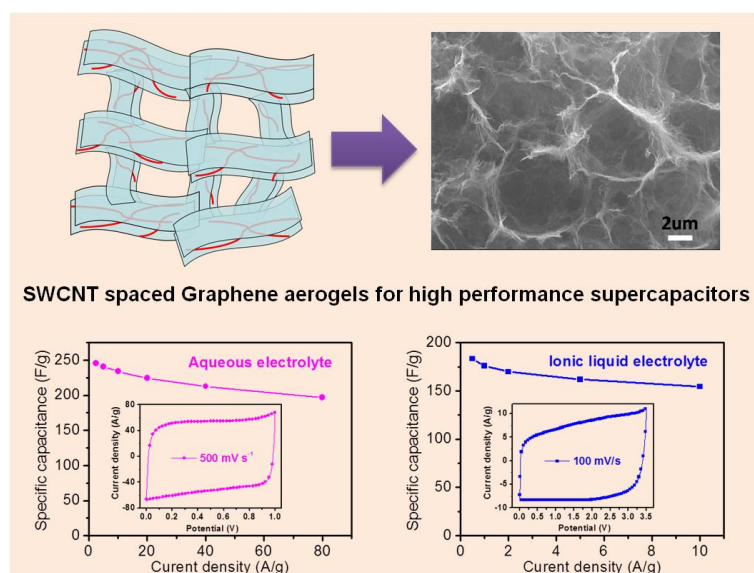
Synthesis and Characterization of Graphene Hollow Spheres for Application in Supercapacitors



- (1). Graphene hollow spheres have been successively fabricated using polystyrene spheres as templates.

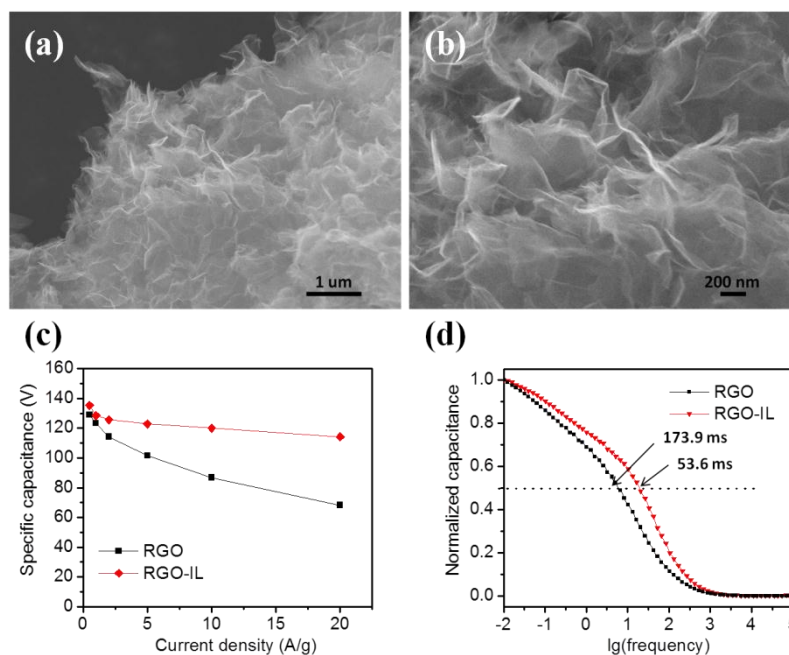
- (2). Compared with stacked planar graphene, the graphene hollow spheres offer more free space between spheres, leading to larger accessible surface area for ion adsorption.
- (3). Electrochemical tests show that the graphene hollow spheres showed high specific capacitance of 273 F g^{-1} at a current density of 0.5 A g^{-1} and 197 F g^{-1} at a higher current density of 10 A g^{-1} .
- (4). After charge-discharge of 5000 cycles at a high current density of 10 A g^{-1} , the graphene hollow spheres retained 95% of its initial capacitance.

Carbon nanotube Spaced Graphene Aerogels with Enhanced Capacitances in Aqueous and Ionic liquid Electrolytes



- (1). Single-walled carbon nanotube spaced graphene aerogels were prepared by hydrothermal reduction of graphene oxide and carbon nanotube mixture.
- (2). The composite aerogels show combined macro and micro 3D structure.
- (3). The 3D macro-porous structure provides numerous large pores to make the electrode be wetted quickly by the electrolyte to ensure high rate performance.
- (4). The SWCNTs are placed between the graphene layers to prevent the restacking of graphene sheets and more accessible surface area is made available for ion adsorption.
- (5). The composites deliver a high capacitance of 245.5 F g^{-1} in aqueous electrolyte and a high capacitance of 183.3 F g^{-1} in ionic liquid electrolyte (EMIMBF₄).

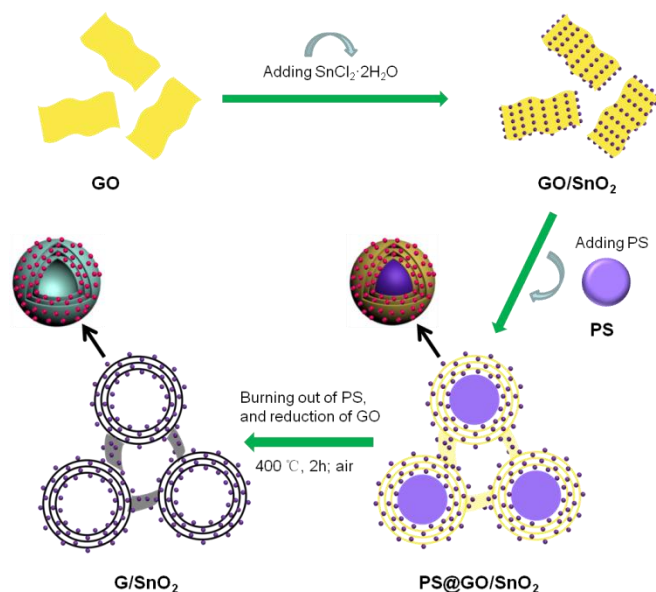
Curved graphene from Ionic liquid mediated reduction of graphene oxide for supercapacitor with improved rate capability in ionic liquid electrolyte



- (1). Curved graphene sheets were prepared by ionic liquid mediated reduction of graphene oxide in aqueous electrolyte.
- (2). When used for ionic liquid electrolyte based supercapacitors, the ionic liquid modification on graphene can significantly improve the compatibility between the modified electrode and ionic liquid electrolyte.
- (3). Electrochemical tests reveal the curved graphene electrode can exhibit much higher capacitance retention under high current density.

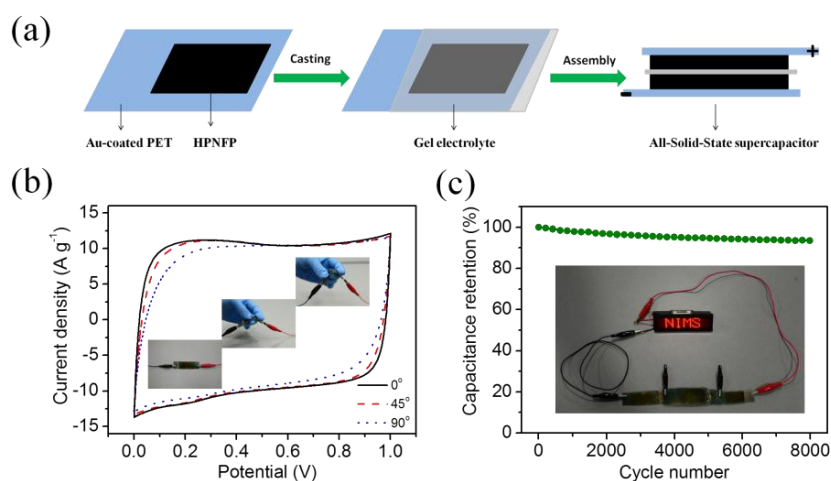
Other extended work

Confining SnO₂ Nanoparticles Between Multi-layered and Interconnected Graphene Shells as Binder-free Anodes for Lithium-ion Batteries



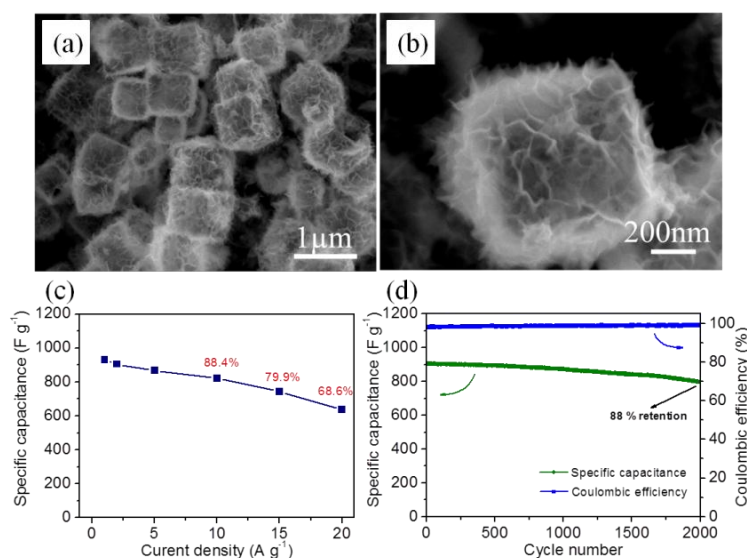
- (1). SnO_2 nanoparticles were confined in interconnected multi-layered graphene shells. Graphene shells serve as conductive matrix to load SnO_2 nanoparticles.
- (2). Graphene shells were interconnected, no need for the binders. The interconnected graphene provided 3D conductive network, facilitating Li^+ and electron transport.
- (3). Multi-layered graphene shells can buffer the volume changes of SnO_2 during cycling.
- (4). Graphene/ SnO_2 composite could deliver a high reversible capacity of 1001 mAh/g, and good cycling performance.

Fabrication of a Highly Porous Carbon Nanofiber Paper with Large External Surface Area and Its Application for High Energy Density Supercapacitors



- (1). Highly porous nanofibers paper (HPNFP) was prepared by carbonization of C_{60} nanofibers
- (2). HPNFP shows a high external specific surface area of $1003 \text{ m}^2/\text{g}$.
- (3). HPNFP based supercapacitors can deliver a high capacitance of 191 F/g , high energy density of 106 Wh/kg in ionic liquid electrolyte.
- (4). A flexible all-solid-state supercapacitor fabricated based on HPNFP exhibits large capacitance of 228 F/g and good flexibility.

Hierarchical NiCo_2O_4 Nanoboxes Constructed by Nanosheets with Excellent Pseudo-capative Properties



- (1). Hierarchical NiCo_2O_4 nanoboxes were firstly prepared by templating Cu_2O nanocubes
- (2). NiCo_2O_4 nanoboxes were constructed by nanosheets with a high specific surface area of $89 \text{ m}^2/\text{g}$.
- (3). The hierarchical structure can provide more active sites for reaction with electrolyte.
- (4). NiCo_2O_4 nanoboxes exhibits a large capacitance of 930 F/g and keep 88 % after 2000 cycles.

9.2 Future Prospects

Graphene based supercapacitors have attracted tremendous research interests over the world. To prevent the restacking of graphene sheets is still a crucial point. Design of functionalized graphene structures with desired shapes, sizes, dimensions could effectively avoid the restacking of graphene

sheets. To further promote the application of graphene based supercapacitors, better control in the morphology and dimension of graphene materials is needed. On the other side, the preparation process of these unique graphene structures usually involves multi-steps and the cost is high, so the developing of novel approaches, which are simple, low cost, and effective, is also important.

In the future, supercapacitors will get more application in the field of energy storage. In view of the emerging wearable electronic devices, more attention should be paid to develop flexible, printable and wearable supercapacitors and integrate the supercapacitors into smart clothing, self-powered nanogenerator, sensors and so on.

Chapter 10

Achievements

10.1 List of Publications

- (1) Qingguo Shao, Jie Tang, Yuexian Lin, Feifei Zhang, Jinshi Yuan, Han Zhang, Norio Shinya, Lu-Chang Qin, “Synthesis and characterization of graphene hollow spheres for supercapacitors” *Journal of Materials Chemistry A* , 1, 15423-15428 (2013).
- (2) Qingguo Shao, Jie Tang, Yuexian Lin, Jing Li, Faxiang Qin, Jinshi Yuan, Lu-Chang Qin “Carbon nanotube spaced graphene aerogels with enhanced capacitance in aqueous and ionic liquid electrolyte” *Journal of Power Sources*, 278, 751-759 (2015).
- (3) Qingguo Shao, Jie Tang, Yuexian Lin, Jing Li, Faxiang Qin, Jinshi Yuan, Lu-Chang Qin “Ionic liquid modified reduced graphene oxide for supercapacitor: a new approach toward improving the rate capability in ionic liquid electrolyte” *Electrochimica Acta*, submitted
- (4) Qingguo Shao, Jie Tang, Yuexian Lin, Yige Sun, Faxiang Qin, Jinshi Yuan, Lu-Chang Qin “Confining SnO₂ nanoparticles between multi-layered and interconnected graphene shells as binder-free anodes for lithium-ion batteries” In preparation
- (5) Qingguo Shao, Han Zhang, Jie Tang, Yuexian Lin, Jinshi Yuan, Lu-Chang Qin “Fabrication of a highly porous carbon nanofiber paper with large external surface area and its application for high energy density supercapacitors” In preparation
- (6) Qingguo Shao, Jie Tang, Yuexian Lin, Kun Zhang, Jinshi Yuan, Lu-Chang Qin “Hierarchical NiCo₂O₄ nanoboxes constructed by nanosheets with excellent pseudo-capative properties” In preparation

10.2 Oral Presentations

(1) Qingguo Shao, Yuexian Lin, Jie Tang, Norio Shinya, Lu-Chang Qin. “Synthesis of Graphene Hollow Spheres and Their Application in Electrochemical Supercapacitors.” The 4th Annual Meeting of the Nanofiber Society of Jpn, 2013 July 5th, Tsukuba, Japan.

(2) Qingguo Shao, Jie Tang, Yuexian Lin, Feifei Zhang, Jinshi Yuan, Han Zhang, Norio Shinya, Lu-Chang Qin. “Formation of Graphene Hollow Spheres as High Performance Electrode Materials for Supercapacitors.” The 23rd MRS-Japan Academic Symposium, December 9-11, 2013, Yokohama, Japan

10.3 Patent

(1) 唐捷、邵慶国、秦禄昌「グラフェン球状中空体の作成方法、グラフェン球状中空体及びグラフェン球状中空体集積キャパシター」出願番号;特願 2013-104557; 出願日:2013 年 5 月 16 日

Acknowledgements

This thesis was accomplished under the supervision from my supervisor Professor Jie Tang. During the three years Ph.D program, Prof. Tang has devoted to instructing my research and study from selecting the topic and designing the proposal to solving the problem and composing the thesis. Her expertise, innovation, and generosity has deeply affected me and greatly encouraged me for my study and life in Japan. Her scientific spirit is a model of virtue for my future career and life. It is my great honor to study and work in her group. Therefore, I am taking this opportunity to sincerely giving my millions of thanks to her.

I also like to give my great thanks to Professor Lu-Chang Qin from University of North Carolina at Chapel Hill for his insight resolving many problems encountered throughout research and scientific paper writing, for his inspiring and encouraging way to guide me to deeper understanding of research, and his invaluable comments during my graduate study.

I really appreciate the valuable suggestion and assistance from all my group members: Dr Han Zhang, Dr Jinshi Yuan, Dr Feifei Zhang, Dr Faxiang Qin, Dr Qian Cheng, Dr Kun Zhang, Mr Yuexian Lin, Mr Jing Li, Mr Yige Sun, and I would like to give my thanks to the secretaries of our group Mrs. Kawamura Yukiyo and Furusawa Sachiko for their kindly help during the study.

I am highly indebted to my committee members: Professor Kenji Sakurai; Professor Kiyoto Matsuishi; Professor Yoshihiko Takeda.

I would like to give my most sincere thanks and love to my parents, my elder sisters, my wife and all friends who are always standing by me and backing my study abroad. I cannot image the life without their selfless love and support.

This work was performed at Materials Processing Unit, National Institute for Materials Science and Graduate School of Pure and Applied Science of University of Tsukuba. Thanks for NIMS Junior Researcher Assistantship for supporting my research in Japan.